MODELING AND CONTROL OF

MINIATURE SERVO PNEUMATIC ACTUATORS

MODELING AND CONTROL OF MINIATURE SERVO PNEUMATIC ACTUATORS

By

ZHIHONG RAO, B. A.

A Thesis

Submitted to the School of Graduate Studies

in Partial Fulfillment of the Requirements

for the Degree

Master of Applied Science

McMaster University

MASTER OF APPLIED SCIENCE (2005) McMaster University

(Mechanical Engineering) Hamilton, Ontario

TITLE: Modeling and control of miniature servo pneumatic actuators

AUTHOR: Zhihong Rao, B. A. (Xi'an JiaoTong University, China)

SUPERVISOR: Dr. Gary M. Bone, Associate Professor

NUMBER OF PAGES: xvi, 118

ABSTRACT

Pneumatic actuators are low-cost, safe, clean, and exhibit a high power to weight ratio. In this thesis a novel servo pneumatic system based on miniature cylinders is presented. The first cylinder investigated has a 9.5 mm bore size. Four low-cost 2-way proportional valves are incorporated to provide greater design flexibility than the traditional single 4-way servo valve solution. A nonlinear system model is developed and validated using open-loop experiments. The use of bipolynomial functions to model the valve flow rates is shown to provide a more accurate solution than the commonly used nozzle flow equations.

Two multiple-input single-output nonlinear position controllers are designed using the inverse dynamics and backstepping method respectively. In addition to position control, the control designs allow a second control objective to be implemented. In the inverse dynamics controller, the chamber pressures are controlled in inner loops and the position is controlled in an outer loop. In the backstepping controller, the stability analysis includes the effects of friction modeling error and valve modeling error. In experiments with a 1.5 kg moving mass, the inverse dynamics controller produced SSE within ±0.08mm and the backstepping controller ±0.05mm. The two control laws produced maximum tracking errors of ±0.5 mm and ±0.3mm for a 1 Hz sine wave trajectory respectively. The tracking errors are shown to be 85% less than those produced by a linear controller.

Experiments demonstrate that the two controllers are robust to the system operating in horizontal and vertical orientations. They are also robust to an increase of payload but not to a decrease of payload. This problem can be overcome by tuning the controller parameters for the smallest payload. The two controllers are further tested with miniature cylinders with different bore diameters and stroke lengths. The smallest cylinder tested has a 4 mm bore diameter.

ACKNOWLEDGEMENTS

I would like to express my sincere gratitude to my research supervisor, Dr Gary M. Bone, for his valuable guidance and support. I would also like to thank the technical services coordinator Mr Dave Schick and technicians Mr Joe Verhaeghe and Mr Mark Mackenzie for their help with the test setup. I also thank my colleagues and friends for their advice and encouragement. Finally I would like to specially show appreciation to my family for their encouragement and support.

TABLE OF CONTENTS

LIST OF FIGURES

LIST OF TABLES

ABBREVIATIONS

DOF	degree of freedom
DZC	dead zone compensation
LQR	linear-quadratic regulator
LVDT	linear variable displacement transformer
MISO	multiple-input single-output
NN	neural network
PD	proportional plus derivative
PI	proportional plus integral
PID	proportional plus derivative plus integral
PMA	pneumatic muscle actuator
PVA	position plus velocity plus acceleration
PWM	pulse width modulation
RLS	recursive least square
RMSE	root mean square error
SISO	single-input single-output
SSE	steady state error

NOMENCLATURE

ρ_a, ρ_b	mass density of air in chamber A , chamber B
$\eta_1, \eta_2, \eta_3, \eta_4$	nonlinear function of valve flow rate
λ , K_s , Λ_a, Λ_b	inverse dynamics controller gains
A_a, A_b	cross sectional area of chamber A and B
A_{rod}	cross sectional area of the rod
c_v	specific heat of air at constant volume
c_p	specific heat of air at constant pressure
$-_d$	subscript, desired
e	tracking error
F_c, F_s, F_v	Coulumb friction, stiction, viscous friction coefficient
F_{ext}	resultant external force excluding friction
F_p, F_f, F_l	applied driven force, friction force, load force
k_1, k_2, k_3, k_4	backstepping controller gains
K	ratio of specific heats of air
K_v	velocity observer gain
L	stroke length
M	moving mass
$\dot{m}_a, \dot{m}_b$	mass flow rate into chamber A, chamber B

$\dot{m}_1, \dot{m}_2, \dot{m}_3, \dot{m}_4$	mass flow rate of four valves
P_a, P_b	pressure in chamber A, B
P_s, P_0	supply pressure, atmosphere pressure
P_u, P_d	upstream pressure, downstream pressure
Q	heat transfer into the system
R	universal gas constant, 287 J/kg°K
s	Laplace variable
S	filtered error
T_s, T_a, T_b	temperature of supply air, temperature in chamber A, chamber B
T	system temperature
u	virtual control signal
u_1, u_2, u_3, u_4	voltage applied to four valves
v, a	piston velocity, acceleration
V_a, V_b	volume of chamber A, B
V_{a0}, V_{b0}	dead volume at chamber A side, chamber B side
v_s	Stribeck velocity
v_{th}	velocity threshold
y	piston position
z_1, z_2, z_3, z_4	backstepping controller states

CHAPTER 1

INTRODUCTION

1.1 Preface

Pneumatic actuators are a class of devices or mechanisms activated by air pressure. Pneumatic cylinders are one of the most common actuators used in industry because of their unique advantages. They are low-cost, safe, and clean and possess a high power to weight ratio. Conventionally the cylinders are used for point-to-point motion controlled by on/off valves in mechanisms with hard stops.

Pneumatic actuators are of interest for robotics and other fields due to their advantages, but closed-loop position servo control of pneumatic actuators is difficult because of the nonlinearities that inherently come from the compressibility of air Other factors, such as the big friction force and the nonlinearity of the valves, further increase the difficulty

Research on pneumatic servo control systems has been ongoing for more than 40 years. A typical pneumatic servo control system includes a cylinder and a proportional/servo valve. The system model has been well established and many control strategies have been developed. The availability of low-cost high performance computers has enabled the implementation of increasingly sophisticated control algorithms. Servo pneumatic actuators have been successfully applied in many fields, including rehabilitation, assistive devices and walking robots.

In the prior servo pneumatics research standard sized pneumatic cylinders (with a typical bore diameter of 30 mm) were employed. Miniature sized pneumatic cylinders (with bore size less than 10mm) have not been studied. These cylinders possess the advantages listed above and are applicable to smaller scale applications in robotics, such as robotic hands and millirobotics. At the same time they are more challenging to control for two reasons. First, seal friction is proportional to bore diameter while the force of the air on the piston is proportional to its area. So as the bore size is reduced the ratio of friction force to piston force increases proportionally. Second, the chamber pressures and piston position are more sensitive to small variations in the mass flow rate so the flow rate behavior of the valves must be very precisely modeled.

1.2 Objective and organization of the thesis

The objective of this thesis is to study the modeling and servo control strategies of miniature cylinders with bore diameters less than 10 mm. The system will be modeled in detail, including the cylinder and the valves. Two nonlinear controllers will be designed, simulated and tested. Robustness and generality of the two controllers will be investigated experimentally.

The organization of the thesis is as follows. In chapter 2 the literature related to pneumatic actuator modeling and servo controller design is reviewed. The system structure and model derivation is described in chapter 3. The nonlinear system model includes the pressure dynamics of the pneumatic components and the mechanical dynamics of the payload. A novel method to modeling the mass flow rate of the valves is presented. The model is validated by an open-loop experiment. In chapter 4 two

nonlinear controllers, based on inverse dynamics and backstepping respectively, are designed. Simulation and experimental results are compared with those from a linear controller. The robustness and generality of the two controllers are experimentally tested in chapter 5. The designed controllers are tested with payload variation and in different system orientation. They are also applied to different kind of cylinders with different bore diameters and stroke lengths. Conclusions are drawn in chapter 6. The achievements and limitations of this research are summarized. Recommendations for future works are presented.

CHAPTER 2

LITERATURE REVIEW

2.1 Introduction

In this chapter the research literature related to the pneumatic servo control will be reviewed. This field has been developing for more than 40 years and the literature is quite rich. The following aspects will be reviewed: modeling of pneumatic cylinder servo systems; and design of linear and nonlinear controllers for positioning and motion tracking.

2.2 System modeling

The most common pneumatic servo system consists of a double acting cylinder and a four-way servo valve. Some other systems consisting of different components, e.g., single acting cylinder [1], three-way valve [2] or ON/OFF valve controlled with pulse-width-modulated (PWM) signal [3][4], have also been studied. Except for the system identification methods that treat the system as a black box [5][6], the system modeling usually includes a few common elements. They are the valve model including the dynamic model and mass flow rate model, thermodynamic behaviour of the working media in the cylinder chambers and dynamic behaviour of the payload system. Among these aspects of system modeling, the valve modeling and the friction modeling are known to be two most difficult parts. This section will review the literature covering different aspects of the system modeling.

One of the pioneers to study the pneumatic servo system was Shearer [7]. He developed a detailed model of a pneumatic servo system in 1956. This work is still the foundation of pneumatic servo system modeling today. In this study the system consisted of a 4-way proportional valve and a double acting cylinder. The emphasis was placed on studying the dynamic behaviour of the working media in the cylinder chamber and the pressure-flow characteristics of the control valve. The spray nozzle formula was applied to the orifice of the valve to obtain the relationship between the driving signal and the mass flow rate. The ideal-gas equation, mass continuity equation and energy conservation law were applied to the gas in the controlled volume of the two chambers, resulting the relationship between the mass flow rate and the chamber pressures. Newton's second law of motion was applied to the mechanical system to derive the relationship between the payload movement and the pressure difference. This analysis established a nonlinear model of the system, which was linearized around the midpoint of the stroke and resulted in a 3rd order linear model.

The mass flow rate behaviour of a valve is highly nonlinear. Most of early papers on pneumatic system modeling were based on system linearization about a fixed equilibrium.

In 1988, Liu and Bobrow obtained a linear state space model using an approach similar to Shearer's [8]. The mass flow rate model was linearized with respect to the control signal and the chamber pressure. An experimental method was developed to determine the linearized coefficients. This system was used in a one degree-of-freedom (DOF) robot. Based on the closed-loop simulation and experiment comparison they concluded that their linearized model is valid for any operating point.

McDonell extended the state space model to an adaptive version [9] Some simplifications were made with the model. First, rather than the two chamber pressures, the pressure difference was used as one state. Second, the mass flow rate model was simplified as proportional to the driving signal. Based on this model structure, the unknown parameters are estimated in real time by the recursive least squares (RLS) algorithm. This system was used to drive a one DOF revolute joint through a pulley and cable.

Richard and Scavarda proposed a nonlinear model of pneumatic actuators for positioning control [10] The model structure was similar to Shearer's but was directly used in the nonlinear form. The variation of the effective valve orifice area with the control voltage was identified using curve fitting from experimental values. In addition, the gas leakage between the two chambers was also included in the mass flow rate model. The mass flow rate of leakage is also a nonlinear function of the two chamber pressures.

Bobrow and McDonell indicated that the valve mass flow rate model using the theoretical nozzle formula does not fit the experiment data well [11] They developed a curve fitting method to find the functions describing the control signal and the mass flow rate for a closed-center 4-way servo valve. Quadratic equations were found to fit the experimental data well in least square sense. A similar approach was used by Ning and Bone with an open-center servo valve [12][13] With the open-center valve, both chambers are partial-filling-partial-discharging when the spool is in a certain position range. In their model the effective valve orifice area was fit by high order polynomials.

Richer and Hurmuzlu developed a detailed mathematical model of an asymmetric double acting cylinder and a proportional spool valve [14]. In their model, the nozzle formula was used for mass flow rate model. The inactive volumes (also known as dead volumes) at the ends of the stroke and the connecting ports were considered. The Coulomb and viscous frictions were included. In addition, the connecting tube between valve and cylinder was considered due to the pressure drop and flow delay. Finally, the dynamic response of the valve spool was included and the effective valve area was calculated from the spool position. They concluded that the connecting tube and the valve dynamic can be neglected to save the online computations when the tube is not too long and the actuator bandwidth is low. The model parameters were identified and the model was validated experimentally.

Nouri *et al.* proposed a novel procedure for valve modeling using the nozzle formula [15]. By scaling the time axis, the pressure vs. time curve at different valve voltages can be fitted in one formula, thus making the effective valve orifice area easier to be identified. This method can only applied to the nozzle spray formula.

Friction is a complex phenomenon existing in all mechanical systems. A comprehensive survey can be found in [16]. In the pneumatic system, the friction mainly comes from the seal between the piston and the cylinder inner wall. Most papers included the Coulomb friction and/or viscous friction, e.g., [7], [14] and [17]. Ning used a classical friction model including viscous friction, Coulomb friction and Stribeck effect [12]. Wang *et al.* investigated the friction force distribution along the cylinder stoke [18]. Their experiment showed that the stiction force depends on the piston position and the direction

of its movement. This uneven distribution makes the modeling and controlling very difficult.

In 1995, Canudas *et al* proposed a new friction model [19], which was named the LuGre model later It characterizes the friction by the average deflection of elastic bristles between two contact surfaces at a microscopic level. In addition to the classical static friction model, the LuGre model captures most of the features of the friction phenomena. friction lag, pre-sliding displacement, stick-slip and hysteresis. However, identification of the model parameters requires a large amount of experiment data, for example, see [20]. Recently Madi *et al.* tried to estimate the LuGre model parameters for a pneumatic servo system based on interval analysis and set inversion method [21] They obtained the parameters with an uncertainty range. This method was time consuming and no precise result was obtained. Robust control is necessary Nouri *et al.* applied another newly developed comprehensive friction model, the so-called Leuven model, to the pneumatic system [15] Only the model structure was discussed in the paper

2.3 Position servo control

The controller synthesis for the pneumatic servo system has progressed in parallel with the control theory development over the last forty years. This section will focus on the literature using linear and nonlinear controller designs for the pneumatic systems.

Before the earlier 90's, most control design used linear control techniques, such as proportional-plus-derivative-plus-integral (PID) and its variations, state space feedback using pole placement or linear-quadratic regulator (LQR).

Moore *et al.* proposed a position-plus-velocity-plus-acceleration (PVA) controller based on a third order linear transfer function [22]. This controller was designed for point-to-point servoing. In addition to the conventional proportional control, they introduced a "minor-loop compensation" that fedback the velocity and acceleration. The minor-loop compensation in fact introduced controllable damping thus the proportional gain can be made higher to reduce the steady-state error (SSE) as well as increase the response speed. Their experiments achieved a settling time of 0.53 seconds and repeatability of 0.1mm for 275 mm movement on a linear asymmetric cylinder with a 25 mm bore, 10 mm rod and 400 mm stroke. By introducing the minor-loop compensation, the SSE was reduced by a factor of 18 and the settling time was reduced to one-third compared with that of without the compensation.

Ning and Bone designed a PVA/PV controller [23]. In their approach, the acceleration feedback is turned off when the piston is close to the target position. This shortened the settling time by eliminating the noisy acceleration signal. A dead-zone compensation (DZC) was added to the control signal to reduce SSE based on the tracking error and the valve voltage. Later they used pole placement method to calculate the PVA gains more systematically and a feedforward term was added [24]. They achieved 0.01 mm SSE and 3 mm tracking error for a single rod cylinder (25 mm bore, 10 mm rod and 300 mm stroke) and a rodless cylinder (25 mm bore and 600 mm stroke), over a range of conditions, i.e., different friction conditions, payloads from 1.2 to 11.2 kg, and vertical and horizontal orientations.

In 1988, Liu and Bobrow used a state feedback controller [8]. Three methods were investigated for the feedback gain selection. The first was proportional-plus-derivative (PD) control that eliminates the pressure measurement. In the second one they added the pressure difference as a state. In the first two methods, the feedback gains were tuned by the root locus method. In their third method the two chamber pressures were treated as two states and a LQR design was used to obtain the feedback gains. They included results from experiments on their test apparatus, a one DOF rotary robot driven by a linear cylinder. The error to a 1 radian step input was 0.03 radians and the rising time was 0.15 seconds.

McDonell and Bobrow extended the state space feedback controller to an adaptive version in 1993 [9]. They used position, velocity and pressure difference as states. Open-loop feedforward control was used to drive the plant along the desired trajectory. Feedback control was used to minimize the state tracking error and control effect using the LQR algorithm. The system parameters were identified online by the RLS algorithm with forgetting factor. In their controller the friction was omitted. Their test apparatus is a 1 DOF revolute robot driven by linear cylinder through a pulley and cable. They showed 0.4 degrees tracking error with arbitrary trajectory in the range of 130 degrees. They also illustrated the capability to payload change and system fault tolerance. They found that which limits the speed of motion is valve saturation rather than parameter convergence.

Lai *et al.* proposed a cascaded controller for a system consisting a linear cylinder and two on-off valves in 1990 [3]. An outer loop with displacement and velocity feedbacks was used to control the load displacement and obtain the desired pressure. An

inner loop utilizing proportional-plus-integral (PI) control was formed to control the actuator pressure. Friction was compensated by a feedforward term in the outer loop when tracking error exceeds a threshold. They used on-off valves and the control signal was modulated to form the PWM signal driving the on-off valve. In this way the on-off valve actually imitated a proportional valve. In their system, only one chamber of the cylinder was controlled. The other chamber was kept open to the atmosphere. They showed experiment of 76.2 mm step response with an asymmetric cylinder in a five DOF commercial pneumatic robot, the bore diameter appeared to be 317.5 mm. No SSE values were reported.

Varseveld and Bone developed a fast, accurate and inexpensive pneumatic position servo system consisting of an asymmetric cylinder (152 mm stroke and 27 mm bore) and four on-off valves [4]. They used a controller combining PID control, friction compensation, bounded integral action and position feedforward. A novel PWM valve pulsing scheme was developed to eliminate the velocity output deadband and to improve the linearity. A worst case SSE of 0.21 mm was achieved with a rise time of 0.18 seconds for step inputs from 0.11 to 64 mm. Tracking errors to a 64 mm S-curve profile were less than 2 mm. Aziz and Bone later presented an auto-tuning procedure for tuning controller [25]. The controller gains were first calculated based on off-line model-based analysis. A heuristic method was used to tune the gains based on the desired overshoot, rising time and SSE. Three different cylinders were tested to demonstrate the efficiency of the method. The best experimental SSE was 0.04 mm for 30 mm step inputs and the rising time was 96 ms. Average tracking error to S-curve was 0.26 mm.

Lee *et al.* proposed a tracking position controller with a rodless cylinder (200 mm stroke and 25 mm bore) and a 5-port servo valve [26]. The controller structure was similar to [3]. The inner loop for pressure control was a PID controller with feedback linearization. The outer position control loop was also a PID controller augmented with friction compensation. Two methods were used to estimate the friction. One was a neural network (NN) and the other was a nonlinear observer. In the NN friction estimator, the 2-3-1 multi-layered perceptron type NN was trained based on the back-propagation learning rule. The resulting functional relationship between velocity, acceleration and friction was an irregular surface. With the nonlinear observer, only the Coulomb friction was considered. Their experiment results showed that the friction compensation drastically improved the tracking performance, but the tracking error was still big. For the 75 mm amplitude 0.2 Hz sine wave tracking, the peak errors were 8.1 mm using the NN estimator and 12.9 mm using the nonlinear observer. The main reason is that the friction in the vicinity of zero velocity was not well estimated.

Nonlinear control theory has been attractive since last decade. Many researchers used nonlinear control for pneumatic servo in last ten years. Examples include input-output and feedback linearization, inverse dynamic control, sliding model control and backstepping control.

Richard and Scavarda used input-output linearization via a static state feedback in the continuous time domain [10]. An inner loop was used to linearize the system input-output behaviour. An outer loop was then used to set the desired dynamic behaviour for the linearized system. They also analyzed the linearized 3rd order model with root loci in

both continuous time and discrete time. From the continuous time root locus they confirmed that the middle stroke position is the least stable for the linearized 3rd order model. On the other hand, for a sampled data system positions near the end stroke is less stable. This was confirmed by experiment. The nonlinear control can suppress the oscillation at both end of the cylinder. Their experiments were performed on a rotary vane actuator, an SSE of 0.5 degrees and a 0.2 seconds rising time were obtained for a step response of 10 degrees.

Bobrow and McDonell did a comprehensive nonlinear control study with a pneumatic cylinder driven robot with revolute joints [11]. In the servo control part, they used two methods, inverse dynamic method [27] and "Slotine & Li" method [28], to obtain the desired torque to follow the trajectory and a PD controller to achieve the desired torque. The "hierarchical system stability theorem" was used to prove the overall system stability. Their three-joint robot had a maximum tracking error of 4 degrees when the joint trajectories had maximum amplitude of 100 degrees. Ning [12] also implemented the "Slotine & Li" controller with two different cylinders as described in [24], and achieved 0.01 mm SSE and maximum tracking error of 2 mm for different trajectories.

Sliding mode control is a popular nonlinear control design method due to its relative simplicity and robustness. For a survey of sliding mode control see [29].

Paul *et al.* designed a reduced order sliding mode controller for a pneumatic system using two solenoid valves [17]. The valve flow rate was assumed to be proportional to the control signal. A first-order sliding surface was used to eliminate the pressure sensors.

Relay control was used for the switching term. They achieved 1 mm SSE on a symmetric cylinder with 25.4 mm bore and 305 mm stroke. Tang and Walker used a switching with proportional feedback scheme for a similar system but they only achieved 5 mm SSE over 100 mm stroke length with a 32 mm bore cylinder [30].

Surgenor and Vaughan used an equivalent control plus boundary layer switching scheme [31]. The sliding surface included tracking error, velocity and acceleration. The equivalent control was a PVA controller. By introducing the boundary layer, the chatter in control signal was drastically reduced. They achieved 0.2 mm SSE over 50 mm stroke length with a standard double acting cylinder (25 mm bore, 10 mm rod and 120 mm stroke) and the experimental results demonstrated the robustness to the payload variation.

Song and Ishida [32] developed a robust sliding mode controller for a system consisting of a cylinder (300 mm stroke and 63 mm bore) and two proportional valves. A model reference robust control approach was used. The sliding surface consisted of the model following error and its derivative. The switching law was boundary layer control and included the reference model output, the position measurement and their derivatives. They demonstrated experimental results with 50 mm forward and backward transitions with different payloads in the two directions. The tracking error was smaller than 2 mm and SSE was about 0.2 mm.

Pandian *et al.* used forth order state feedback and relay switching control [33]. The sliding surface included the position error, pressure error and their derivatives. They also included adaptive law for the payload mass estimation, proved by the Lyapunov's second method. Their controller was implemented on a CKD PCU2-FB cylinder. The bore size

was not specified. The SSE of their system was within 0.3 mm for a 300 mm step response for both horizontal and vertical orientation.

Ning and Bone used equivalent control plus boundary layer switching scheme [34], [12]. The sliding surface was first order and included tracking error and its derivative. The equivalent control was obtained for both a linear forth order model and a nonlinear model. They obtained 0.01 mm SSE and maximum tracking error of 1 mm for different trajectories. Robustness to payload mass change and orientation were also demonstrated.

Backstepping is a recently developed nonlinear control design methodology that started in the 90s [35], [36]. This method was developed from the feedback linearization theory. It uses the Lyapunov theory in a recursive way such that the global or regional stability is ensured in each step of the design procedure. Only one paper is found for the pneumatic cylinder servo using backstepping up to date. Backstepping design for systems similar to pneumatic cylinder system, e.g., hydraulic system and pneumatic muscle actuator (PMA), has been reported.

Rifai and Bridges applied integrator backstepping control design to a single link robot driven by a pneumatic cylinder [37]. The mechanism was similar to that in [8]. Two servo flow valves were used to control the two chamber pressures separately. Backstepping design was used to derive the desired two chamber flow rates. The valve control current was obtained from the valve model inversion. In their design procedure, the friction and the valve model were omitted and one desired chamber pressure was fixed. They showed simulation of 3 Hz 45 degrees sine wave tracking and the tracking error was within 0.006 degrees. No experiment results were included.

Sirouspour and Salcudean applied the backstepping design to a hydraulic servo system [38]. The system consists of a single acting cylinder and a 3-way servo valve. The system dynamics are similar in structure to that of a pneumatic system. Two backstepping controllers, one non-adaptive and one adaptive, were developed, tested and compared with a PD controller. Their experimental result plot shows a 2 mm maximum tracking error for a 4 Hz sine wave with 15 mm amplitude.

Carbonell *et al.* compared a robust backstepping controller, an adaptive backstepping controller and a sliding mode controller with a PMA model [39]. Only simulation results were presented. They concluded that the adaptive backstepping controller is better than the other two.

2.4 Summary

Up to today the fundamental modeling of pneumatic cylinder servo system is still based on Shearer's work in 1956. For the characteristics of mass flow rate of valve, experimental methods have been proposed recently in view of the mismatch between the conventional spray nozzle formula and the experimental data. The use of the traditional friction model is predominant in the literature. Newly developed friction models started to be used with pneumatic servo systems only recently. Due to the limited stroke length, it is hard to get plenty of data for the velocity-friction map, making friction model identification more difficult, compared with that for a rotary motor. Controller design for pneumatic servo system has progressed alongside control theory development. Today, nonlinear control is popular in this field. Sliding mode control is commonly used.

Most of past researches use standard industrial cylinders, that is, bore size bigger than 20 mm, stroke longer than 100 mm. The best SSE achieved for point-to-point movement was 0.01 mm [34], to the author's knowledge.

CHAPTER 3

SYSTEM MODELING

3.1 Introduction

Model-based controllers are known to provide better performance than non-model-based ones. Pneumatic servo systems exhibit nonlinear dynamics due to the compressibility of air, the flow characteristics of valves and the variation of friction. Modeling of each aspect of the system is necessary for improving the control performance.

The system structure will be described first in this chapter. The system model equations will be derived, including the pressure dynamics of the pneumatic components and the mechanical dynamics of the payload. The mass flow rate model of the proportional valves will be discussed in detail. Next, The friction model and parameter identification will be presented. Finally the model is validated by an open-loop experiment.

3.2 System hardware

In this section the system hardware structure is presented first. Then the procedure and results of the sensor calibration are given, followed by the signal conditioning method that deals with the sensor noise.

3.2.1 System structure

The system hardware is shown schematically in Figure 3.2.1 The system consists of a double-acting cylinder, four low-cost 2-way proportional valves and a payload mass mounted on a linear slide table. A linear variable displacement transformer (LVDT) position sensor and two pressure sensors are used to measure the system states. The supply pressure, P_s, was 0.65 MPa absolute. Through out this thesis the pressure is absolute value unless indicated in the context.

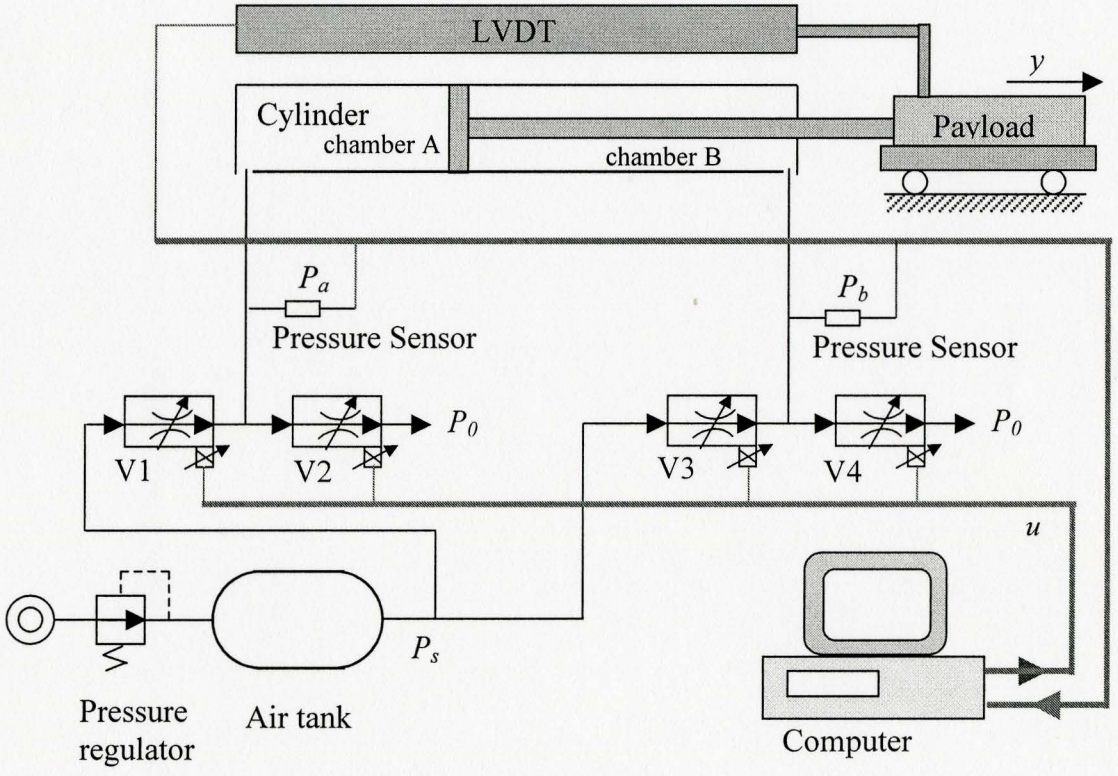

Figure 3.2.1 Pneumatic servo positioning system hardware.

The cylinder (Clippard Instrument Laboratory, Inc. model 3SD-T) has 9.525 mm bore and 25.4 mm stroke. The diameter of the rod is 3 175 mm. The four valves (Clippard model ET-P-05-25A0) have input ranges of 0-5V They are interfaced to a computer (AMD K6-2 166MHz) through customized unity gain amplifiers via a Quanser MultiQ3 I/O board. A pressure sensor (OMEGA Engineering, model PX139-100D4V) is connected to each of the two chambers of the cylinder The LVDT position sensor (Hewlett-Packard, Model 7DCDT-1000) is connected to the payload to measure the displacement. The two pressure sensors and the LVDT position sensor are also connected to the I/O board. The PC is programmed in C and a 1000 Hz sampling frequency is used. The system can be orientated horizontally or vertically. A photograph of the system is shown in Figure 3.2.2.

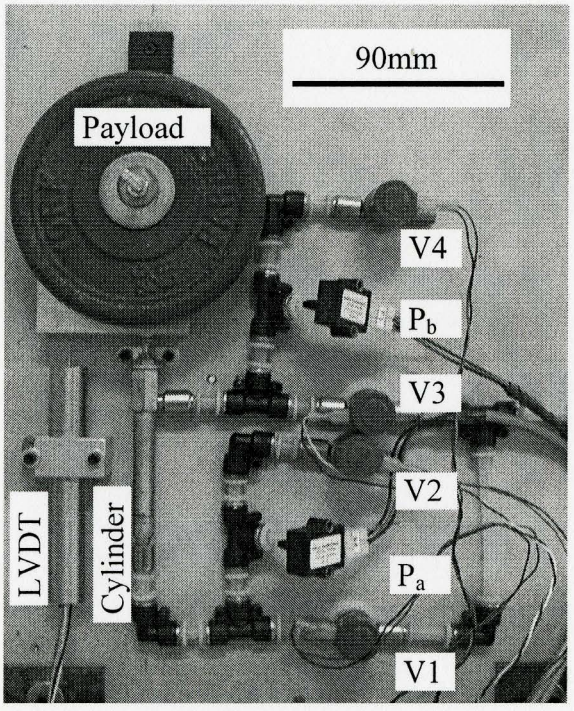

Figure 3.2.2. Photograph of the system in vertical orientation.

The conventional pneumatic servo system uses a 4-way servo valve. The disadvantage of a servo valve is that the valve spool is controlled by one signal and media flowing to the two chambers of the cylinder are dependent. The pneumatic circuit in this research uses four 2-way proportional valves to control the charging and discharging process for the two chambers independently. The four valves are named V1, V2, V3 and V4 respectively (See Figure 3.2.1 and 3.2.2). For chamber *A*, valve 1 controls charging from the supply and valve 2 controls discharging to the atmosphere. With chamber *B*, valve 3 controls charging and valve 4 discharging. This valve arrangement increases the flexibility of the system.

3.2.2. Sensor calibration

The pressure sensors are calibrated as follows. The two sensors were connected to a tank, in which the pressure can be adjusted by a valve. A Wainbee 20BM-160-1/4 pressure gauge (range: 0.1-1.1MPa, resolution: 20kPa/div) was used to read the pressure in the tank. The tank pressure was set to a certain value and the sensor output voltages were recorded. Due to the sensor and A/D board noise, 1000 readings were recorded for both sensors and the average was used for the calibration. Seven gauge pressures were tested and the data are listed in Table 3.2.1 and shown in Figure 3.2.3.

Table 3.2.1: Calibration data of the pressure sensors.

Gauge pressure [MPa]	P_a sensor reading [V]	P_b sensor reading [V]
0.0	2.334	2.322
0.1	2.006	1.999
0.2	1.710	1.702
0.3	1.423	1.413
0.4	1.138	1.126
0.5	0.816	0.806
0.58	0.595	0.586

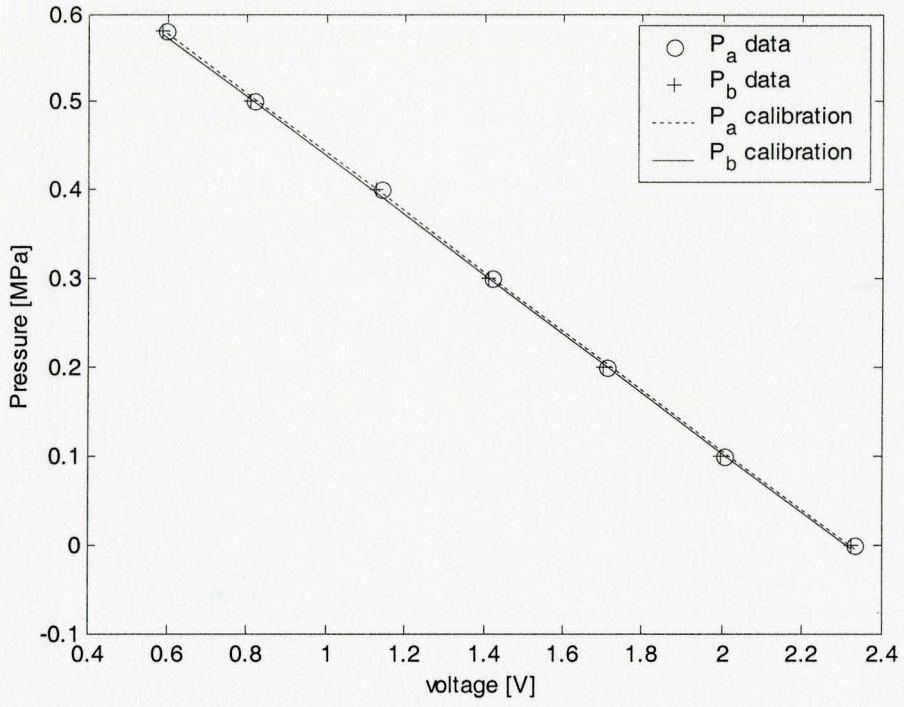

Figure 3.2.3 Calibration of pressure sensors.

From the sensor specification and the measured data it was found that the sensors are linear in the working range. The data were fitted in a first order equation in a least square sense using the linear regression. The results are as follows,

$$\begin{aligned} P_a &= -0.3352u_a + 0.7771 + P_0 \\ P_b &= -0.3352u_b + 0.7738 + P_0 \end{aligned} \tag{3.2.1}$$

where u_a and u_b are the sensor output voltages in volts, P_a and P_b are chamber A and chamber B pressures in MPa. P_0 is the atmospheric pressure added to obtain the absolute pressure.

The LVDT position sensor was calibrated using the same method. The result is,

$$y = -0.00575u_y + 0.0209 \tag{3.2.2}$$

where y is the displacement in meters and u_y is the LVDT sensor output voltage in volts.

3.2.3 Sensor signal conditioning

The noise in the measurement comes from the build-in amplifier of the sensors, the quantization effect of the A/D process and the noise from the power supply. The pressure and displacement measurement are noisy. Examples of the measurements and their spectrum are shown in Figure 3.2.4 and Figure 3.2.5. It was found that the pressure sensors have obvious noise at 270 Hz and the LVDT sensor at 380 Hz. Since the system dynamic response is far lower than these frequencies, the measurements will be low-pass filtered before being used for control. A 4^{th} order Butterworth filter [40] with cut-off frequency of 200 Hz will be used.

From now on we term the measurement after signal conditioning as simply the "measurement". The position measurement is shown in Figure 3.2.6. It has noise of ±0.02 mm. Similarly, the pressure measurement has noise of ±1.5kPa after signal conditioning.

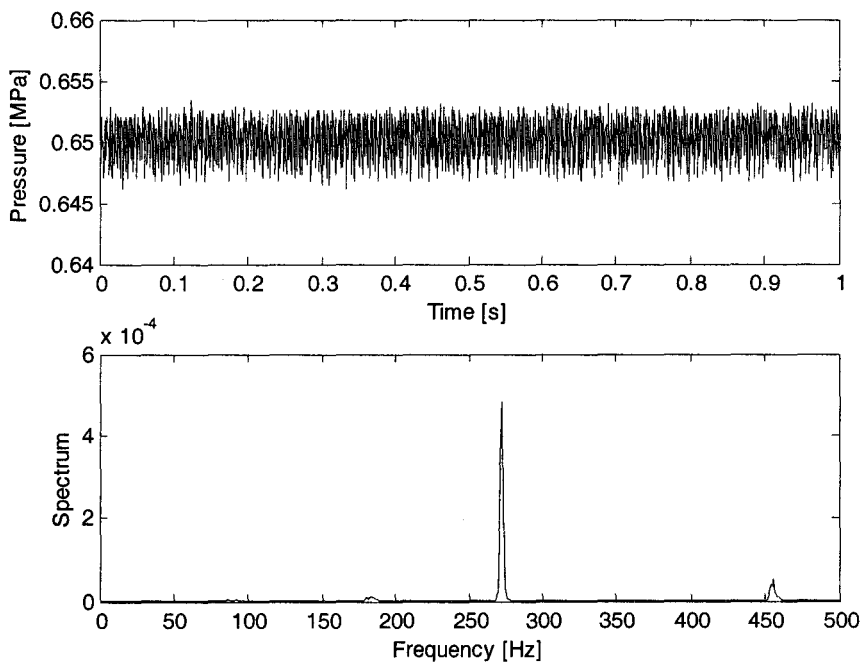

Figure 3.2.4: Pressure measurement and noise spectrum.

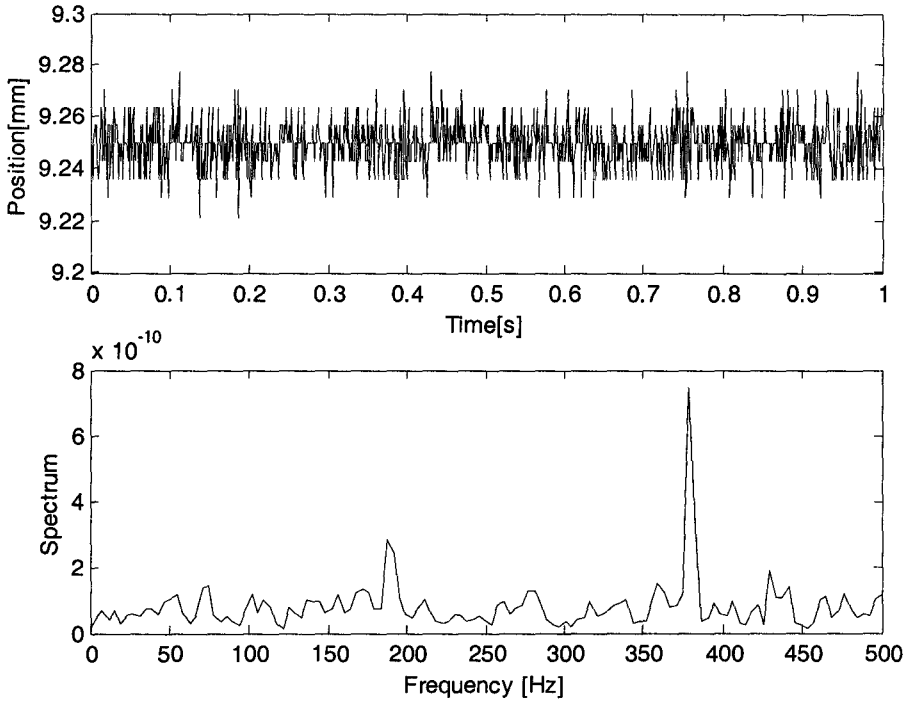

Figure 3.2.5: Position measurement and noise spectrum.

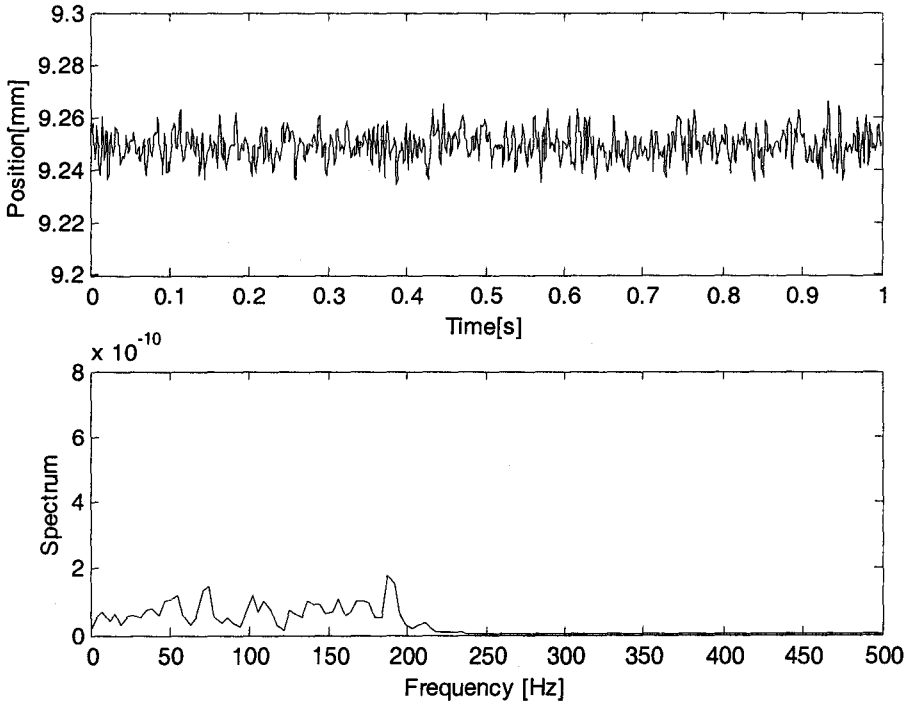

Figure 3.2.6: Position measurement and noise spectrum after signal conditioning.

3.3 Modeling equations

This section derives the nonlinear mathematical model of the system following the approach of Shearer [7]. See the nomenclature for the definitions of variables. To begin, the energy conservation equation is applied to the controlled volume of chamber *A* bounded by the cylinder and piston,

$$\frac{d}{dt}(c_v \rho_a V_a T_a) = c_p T_s \frac{dm_a}{dt} + \frac{dQ}{dt} - P_a \frac{dV_a}{dt} \tag{3.3.1}$$

where $\frac{d}{dt}(c_v \rho_a V_a T_a)$ is the total change rate of internal energy of the system, $c_p T_s \frac{dm_a}{dt}$ is rate of the internal energy of the mass flow into the system, $\frac{dQ}{dt}$ is the rate of heat transfer into the system and $P_a \frac{dV_a}{dt}$ is the work done by the piston. Assuming the air behaves as perfect gas, using the ideal gas equation we have $\rho_a = \frac{P_a}{RT_a}$. Assuming the process is adiabatic, we have $\frac{dQ}{dt} = 0$. Also, assuming the flow rate is much faster then the heat transfer in the system, the temperature difference between the upstream and downstream can be neglected, i.e., $T_s = T_a = T_b$. We will simply denote the system temperature as *T*. Based on these assumptions equation (3.3.1) can be simplified as

$$\frac{c_v}{R}\frac{d}{dt}(P_a V_a) = c_p T \frac{dm_a}{dt} - P_a \frac{dV_a}{dt} \tag{3.3.2}$$

or

$$\frac{c_v}{R} P_a \frac{dV_a}{dt} + \frac{c_v}{R} V_a \frac{dP_a}{dt} = c_p T \frac{dm_a}{dt} - P_a \frac{dV_a}{dt} \tag{3.3.3}$$

This can be rearranged as

$$\frac{c_v}{R}V_a\frac{dP_a}{dt}=c_pT\frac{dm_a}{dt}-\frac{c_v+R}{R}P_a\frac{dV_a}{dt} \tag{3.3.4}$$

or

$$\frac{dP_a}{dt}=\frac{c_pRT}{c_vV_a}\frac{dm_a}{dt}-\frac{c_v+R}{c_v}\frac{P_a}{V_a}\frac{dV_a}{dt} \tag{3.3.5}$$

Using the fact that $K=c_p/c_v$ and $c_p=c_v+R$, equation (3.3.5) becomes

$$\dot{P}_a=\frac{KRT}{V_a}\dot{m}_a-K\frac{P_a}{V_a}\dot{V}_a \tag{3.3.6}$$

Similarly for chamber *B* of the cylinder,

$$\dot{P}_b=\frac{KRT}{V_b}\dot{m}_b-K\frac{P_b}{V_b}\dot{V}_b \tag{3.3.7}$$

The volumes of chamber *A* and chamber *B* are related to the piston position *y*,

$$V_a=A_ay+V_{a0} \tag{3.3.8}$$

$$V_b=A_b(L-y)+V_{b0} \tag{3.3.9}$$

where V_{a0} and V_{b0} are the dead volumes of the two chambers, including the dead volume of the chamber and connecting tube. Due to the small size of the cylinder the dead volumes have to be considered. In the experiment setup the dead volumes at both ends are measured as $V_{a0}=5.52\times10^{-6}m^3$ and $V_{b0}=4.81\times10^{-6}m^3$. Also it is assumed that the pressures distribute evenly in the chambers and the dead volumes such that the pressure measurements equal to the chamber pressures. Substituting (3.3.8) and (3.3.9) into (3.3.6) and (3.3.7),

$$\dot{P}_a = \frac{KRT}{A_a y + V_{a0}} \dot{m}_a - K \frac{P_a A_a}{A_a y + V_{a0}} \dot{y} \tag{3.3.10}$$

$$\dot{P}_b = \frac{KRT}{A_b (L - y) + V_{b0}} \dot{m}_b + K \frac{P_b A_b}{A_b (L - y) + V_{b0}} \dot{y} \tag{3.3.11}$$

The mass flow rates $\dot{m}_a$ and $\dot{m}_b$ are the flow rates into chamber A and B respectively. Since each chamber is controlled by two valves, the net rate of change in mass contained within the chamber is the difference of the flow rates through the two valves for charging and discharging respectively,

$$\dot{m}_a = \dot{m}_1 - \dot{m}_2 \tag{3.3.12}$$

$$\dot{m}_b = \dot{m}_3 - \dot{m}_4 \tag{3.3.13}$$

Usually the mass flow rate of a valve is modeled as a nonlinear function related to the control voltage and the upstream and downstream pressures,

$$\dot{m}_1 = \eta_1(u_1, P_s, P_a) \tag{3.3.14}$$

$$\dot{m}_2 = \eta_2(u_2, P_a, P_0) \tag{3.3.15}$$

$$\dot{m}_3 = \eta_3(u_3, P_s, P_b) \tag{3.3.16}$$

$$\dot{m}_4 = \eta_4(u_4, P_b, P_0) \tag{3.3.17}$$

Note that for charging process, the upstream pressure is the supply pressure P_s and downstream pressure is the chamber pressure P_a (or P_b), for the discharging process the upstream pressure is P_a (or P_b) and the downstream pressure is the atmosphere pressure P_0. These functions will be discussed in the next section in detail.

The mechanical movement of the system is simply derived from Newton's second law of motion,

$$M\ddot{y} = F_p - P_0 A_{rod} - F_f - F_l \tag{3.3.18}$$

where

$$F_p = P_a A_a - P_b A_b \tag{3.3.19}$$

is the applied driving force. Note that the cylinder is asymmetric such that the pressure on the rod cross-section area cannot be neglected, especially for the miniature cylinders. The $P_0 A_{rod}$ term is due to the cylinder asymmetry. F_f is friction in the system and F_l is the load force. When the system is horizontally placed, $F_l = 0$, while vertically placed, $F_l = Mg$. The moving mass M was measured as 1.532 kg, including the mass of the payload, sliding table, the rod and piston of cylinder, the rod of LDVT and other connecting parts.

In summary, equations (3.3.10)~(3.3.19) constitute the system model. The mass flow rate model and the friction model will be discussed in the next sections.

3.4 Mass flow rate model of the valves

The mass flow rate model of the proportional valve is an important part of the system model. As shown in equations (3.3.14)~(3.3.17), the model is a nonlinear function related to the control signal and the upstream and downstream pressures. Conventionally the valve orifice is modeled as a spray nozzle and the nozzle formula is used,

$$\dot{m} = \begin{cases} A(u)P_u\sqrt{\dfrac{K}{RT}\dfrac{2}{K-1}}\sqrt{(\dfrac{P_d}{P_u})^{\frac{2}{K}} - (\dfrac{P_d}{P_u})^{\frac{K+1}{K}}} & \dfrac{P_d}{P_u} > (\dfrac{2}{K+1})^{\frac{K}{K-1}} \text{ (unchoked flow)} \\ A(u)P_u\sqrt{\dfrac{K}{RT}(\dfrac{2}{K+1})^{\frac{K+1}{K-1}}} & \dfrac{P_d}{P_u} < (\dfrac{2}{K+1})^{\frac{K}{K-1}} \text{ (choked flow)} \end{cases} \tag{3.4.1}$$

where $A(u)$ is the equivalent orifice area varying with the valve input, P_u is the upstream pressure and P_d is the downstream pressure. An example of the flow rate curves for this model is shown in Figure 3.4.1. This model may be used with the charging and discharging processes. With the charging process, the upstream pressure, supply pressure P_s, is usually assumed to be constant. Thus when the flow is choked the flow rate is a constant for a certain control signal. With the discharging process, the upstream pressure, the chamber pressure, drops continuously and the down stream pressure P_0 is assumed constant. When the flow is choked the mass flow rate is almost linear with respect to the chamber pressure. This was experimentally verified by previous researchers [7] [14]. Some other researchers have found that their experimental data does not fit this theoretical equation well, e.g., [11] and [13]. Possible reasons are the model does not apply to the particular valve or their flow rate measurements were not accurate enough.

This section will describe two empirical methods for valve mass flow rate modeling. The experimental data will be modeled first using the curve fitting method proposed by [11], then a novel surface fitting method will be proposed. The accuracy of the two methods will be compared.

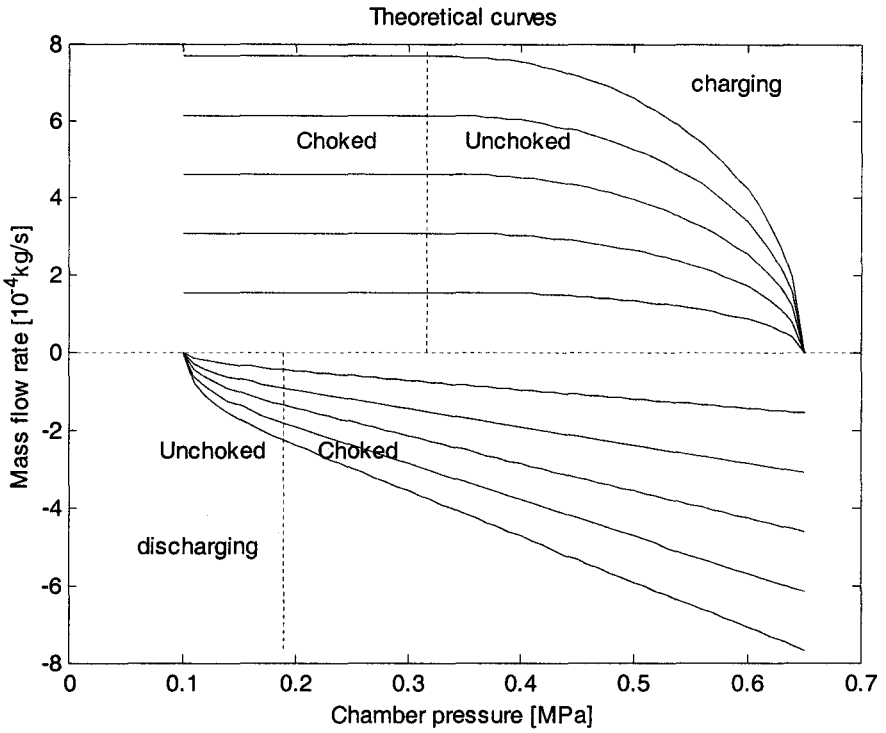

Figure 3.4.1: Example of a valve mass flow rate model based on the nozzle formula.

3.4.1 Measurement of mass flow rate

In mass flow rate modeling, an important issue is how to measure the flow rate. This requires complex and expensive flow rate measurement instruments. A simple way to indirectly measure the flow rate is to use the chamber pressure measurement. Observing equation (3.3.10) for chamber A it is found that when the piston is fixed ($\dot{y} = 0$), the mass flow rate $\dot{m}_a$ is proportional to the chamber pressure $\dot{P}_a$. For example, if the piston is fixed at the fully extended position, $y = L$ and $\dot{y} = 0$, we have

$$\dot{m}_a = \frac{A_a L + V_{a0}}{KRT} \dot{P}_a \tag{3.4.2}$$

This gives a simple way to measure the flow rate in the chamber.

To obtain the mass flow rate measurement, the derivative of the pressure is required. The derivative operation will amplify the noise. The sensor signal conditioning for noise reduction was discussed in section 3.2.3. Since the analysis for valve modeling is done offline, a different filter technique was used with the raw data before signal conditioning to obtain a better result. The raw measurement was low-pass filtered by a 6^{th} order Butterworth filter and the zero-phase forward-backward digital filtering [40] technique was used for zero-phase distortion. This was implemented using the Matlab command `filtfilt`. For each pressure measurement the cut-off frequency of the filter was manually tuned.

Before the flow rate measurement procedure is presented, we discuss the influence of P_s variation, using valve 1 as example. From equation (3.3.14) we know that $\dot{m}_1$ is related to P_s, P_a and u_1 in the charging process. An experiment was carried out to investigate the P_s variation. In the experiment, the initial pressure in the two chambers was P_0 and the piston was fully extended. When the experiment started, valve 1 was set fully open and valve 2 was set fully closed. In this case, the flow rate of valve 1 was maximum at beginning. Figure 3.4.2 shows the experimental measurement of P_s and P_a. P_a rises to P_s in 0.25 seconds and P_s only has small variation in the first 0.05 seconds. The variation of P_s is neglectable. This is due to the relative big tank volume (0.002 m^3) for the supply air and the small flow rate of the valves. In this research, P_s is assumed to be constant for the charging process. The valve flow rate model equation (3.3.14) becomes

$$\dot{m}_1 = \eta_1(u_1, P_a) \tag{3.4.3}$$

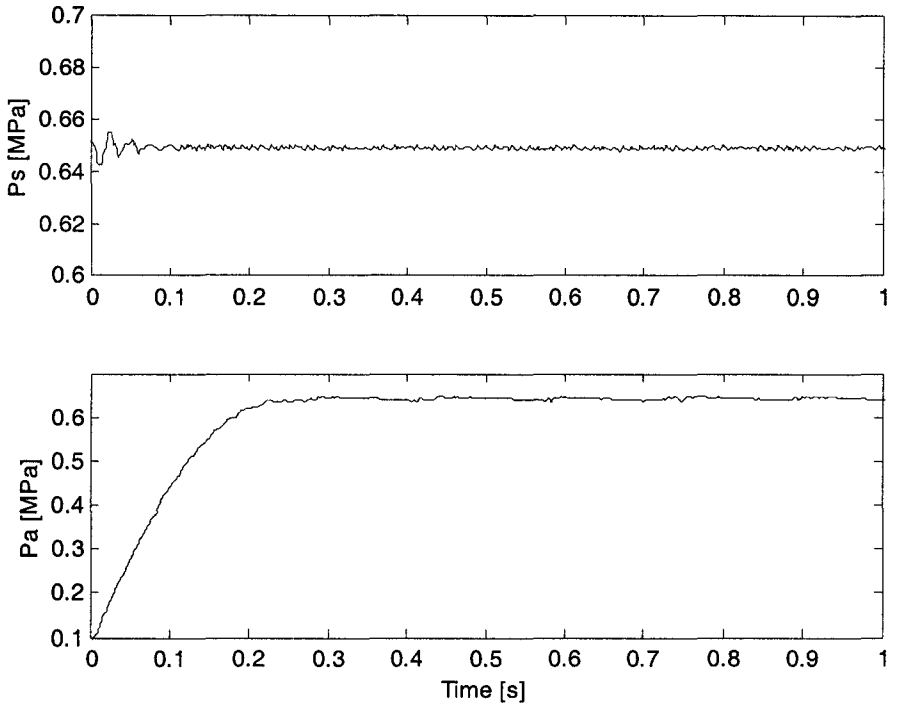

Figure 3.4.2: Supply pressure variation at maximum flow rate.

Now we will discuss the measurement procedure for the valve mass flow rate. Valve 1 is used as example. Since two valves are connected to a chamber, one valve is fully closed when measuring the mass flow rate of the other. For instance, when measuring the charging characteristic of valve 1, valve 2 is fully closed thus $\dot{m}_2 = 0$. From equation (3.3.12) we have: $\dot{m}_1 = \dot{m}_a$. The experiment steps for valve 1 are as follow:

(1) Open valve 1 and valve 4 until the piston is fully extended, then close them.

(2) Open valve 2 to discharge the high-pressure air in chamber A until the pressure drops to P_0, close valve 2.

(3) Send a chosen control signal u_1 to valve 1 and record P_a over a chosen time interval.

(4) Stop when P_a is stable or when a specific time has been reached.

(5) Repeat (1)-(4) for different control signals u_1.

With this method the dynamics of the valve are ignored. Numerous experiments were performed using this procedure.

Figure 3.4.3 shows the P_a vs. time for valve 1. The experiments showed that when u_1<1.6V P_a does not change at all, which means the flow rate is zero. This is due to the dead zone of the valve itself as indicated in its specifications. When u_1 is in the range of 1.6-3.0V, P_a reaches a steady state pressure less than P_s in a specific time and the pressure does not reach P_s even after 20 seconds. When u_1 is higher than 3V, P_a reaches P_s in a short time (less than 2 seconds).

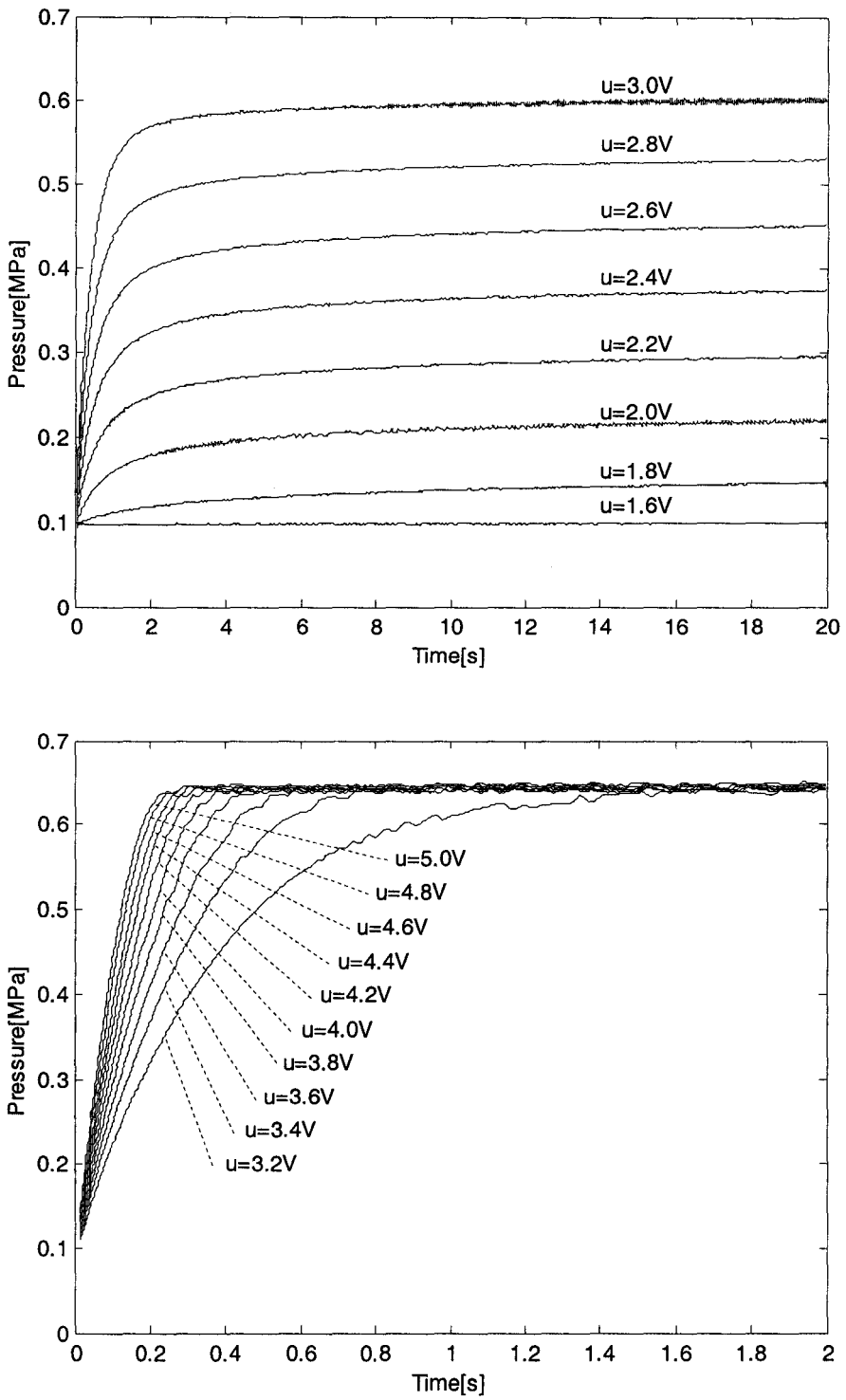

Figure 3.4.3: P_a measurement vs. time for valve 1.

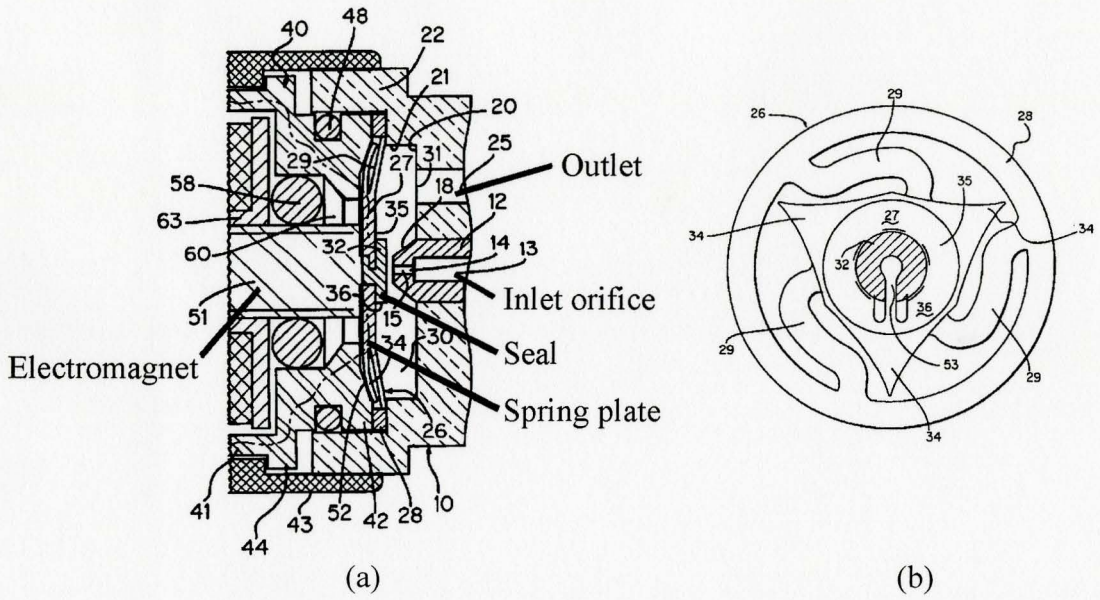

Figure 3.4.4: (a) Structure of the valve, (b) The spring plate [41].

This behavior may be understood by studying the structure of the valve, shown in Figure 3.4.4 [41] The flow rate is controlled by a seal on top of the inlet orifice. The seal is connected to a patented spring plate. The electromagnet lifts the spring plate to open the orifice. The force exerted on the seal is

$$F = F_{coil} + (P_s - P_a)A_0 - F_{pre} - kh \tag{3.4.4}$$

where F_{coil} is the force generated by the electromagnet, A_0 is the orifice area, F_{pre} is the preload force of the spring plate, k is the stiffness and h is the displacement of the spring plate. When the applied voltage is small (less than 1.6V), F_{coil} is so small that the total force is negative due to F_{pre} This force pushes the seal against the orifice such that the valve stays closed. When the applied voltage is in the range of 1.6-3.0V, the spring force kh increases and the pressure difference $(P_s - P_a)A_0$ decreases when the spring plate rises and the P_a rises. When h reaches a certain level, the total force becomes negative such

that the valve is closed again and P_a reaches a steady value less than P_s. When the applied voltage is bigger than 3.0V, F_{coil} is big enough to keep the valve open and P_a can always reach P_s.

The numerical derivative of P_a was used to calculate the flow rate using equation (3.4.2). The central difference method was used. The resulting data were low-pass filtered again to reduce the noise. The flow rate model equation (3.4.3) represents a surface in 3D space. The surface formed by the smoothed data is shown in Figure3.4.5 It is found that the measured flow rate does not fit the nozzle formula equation (3.4.1). Specifically, the measured flow rate is not constant when the flow is "choked" in theory Results for the other three valves are given in Appendix A.

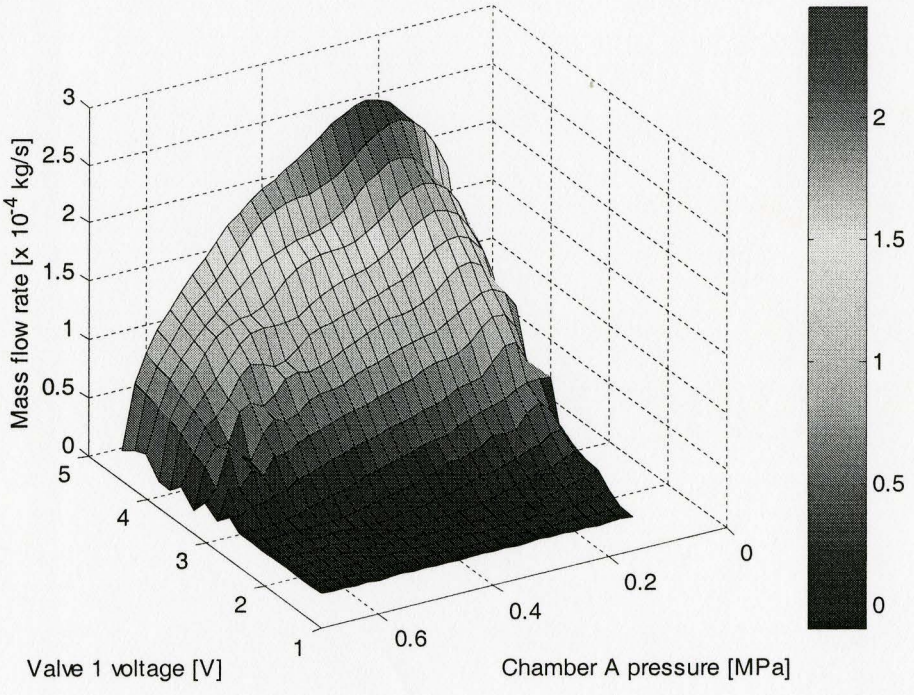

Figure 3.4.5: The measured flow rate surface for valve 1

3.4.2 Mass flow rate modeling

Curve/surface fitting methods are used to find a suitable function $\eta_1(\bullet)$. As shown in Figure 3.4.5, there are some ripples in the measured flow rate surface since there was a compromise between removing sensor noise and keeping the underlying signal. Fortunately, least squares fitting has the capability of removing ripples. Two methods will be used to fit this surface.

3.4.2.1 Sectional curve fitting method

This method was inspired by the work of McDonell [11]. As previously mentioned, the valve 1 opening depends nonlinearly on the applied voltage. Studying the data, the following equations were used to fit the curves.

$$\dot{m}_1 = \begin{cases} 0 & u_1 < 1.6V \\ A_{11}(u_1)\left[P_f(u_1) - P_a\right]^{1.5} & 1.6V \le u_1 \le 3.0V \\ A_{12}(u_1)\sqrt{P_s - P_a} & 3.0V < u_1 < 5.0V \end{cases} \tag{3.4.5}$$

In the second equation, there are two items need to fit. The P_f is the final value of P_a when $1.6<u_1<3.0$V. It was obtained by taking the average of the smoothed P_a data in the time span of 18 ~ 20 seconds. A least squares polynomial curve fitting was then applied to get,

$$P_f(u_1) = 10^5 \times (3.5714u_1 - 4.7143) \tag{3.4.6}$$

This fitting result is shown in Figure 3.4.6. With this $P_f(u_1)$ value, the A_{11} values for each measured data group were obtained by fitting the $\dot{m}_1$ vs. P_a using the golden

section search method [42]. The goal was to minimize the sum of squared fitting error. The obtained data were then fitted using least square polynomial curve fitting to get,

$$A_{11}(u_1) = 10^{-13} \times (-0.4779u_1^3 + 3.0745u_1^2 - 4.5428u_1 + 1.3312) \quad (3.4.7)$$

This is shown in Figure 3.4.7. In the third equation in (3.4.5), only $A_{12}(u_1)$ needs fitting. Similar to $A_{11}(u_1)$, it was obtained as,

$$A_{12}(u_1) = 10^{-6} \times (0.1645u_1 - 0.4347) \quad (3.4.8)$$

It is shown in Figure 3.4.8.

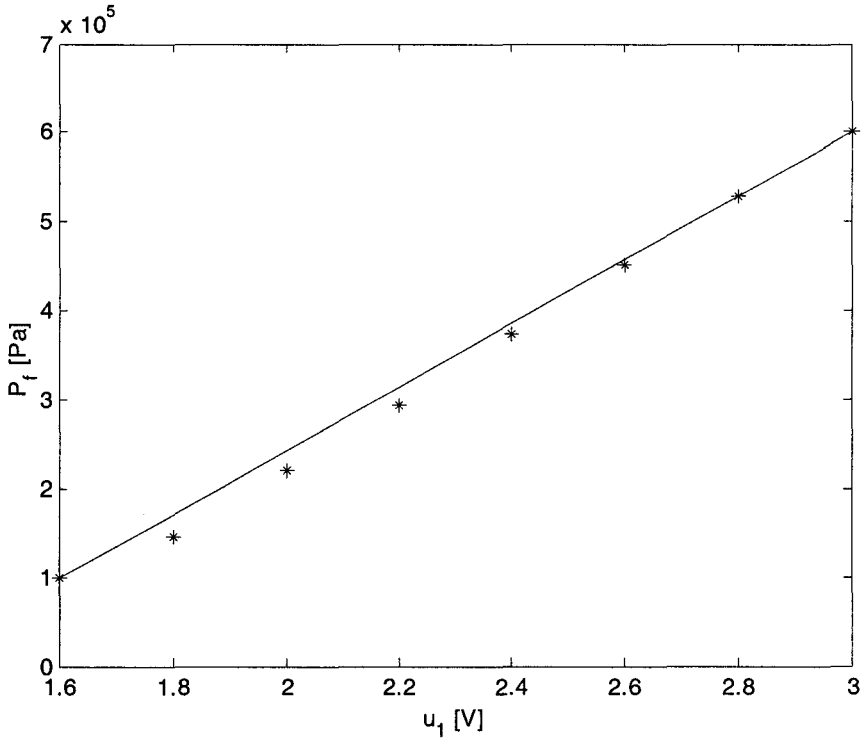

Figure 3.4.6: Curve fitting of $P_f(u_1)$.

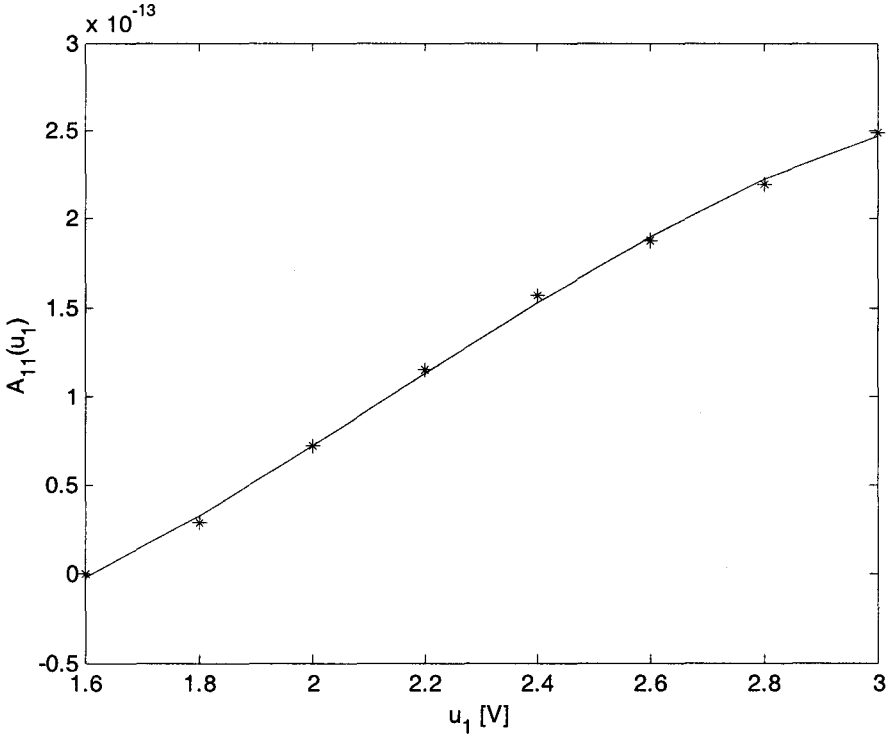

Figure 3.4.7: Curve fitting of $A_{11}(u_1)$.

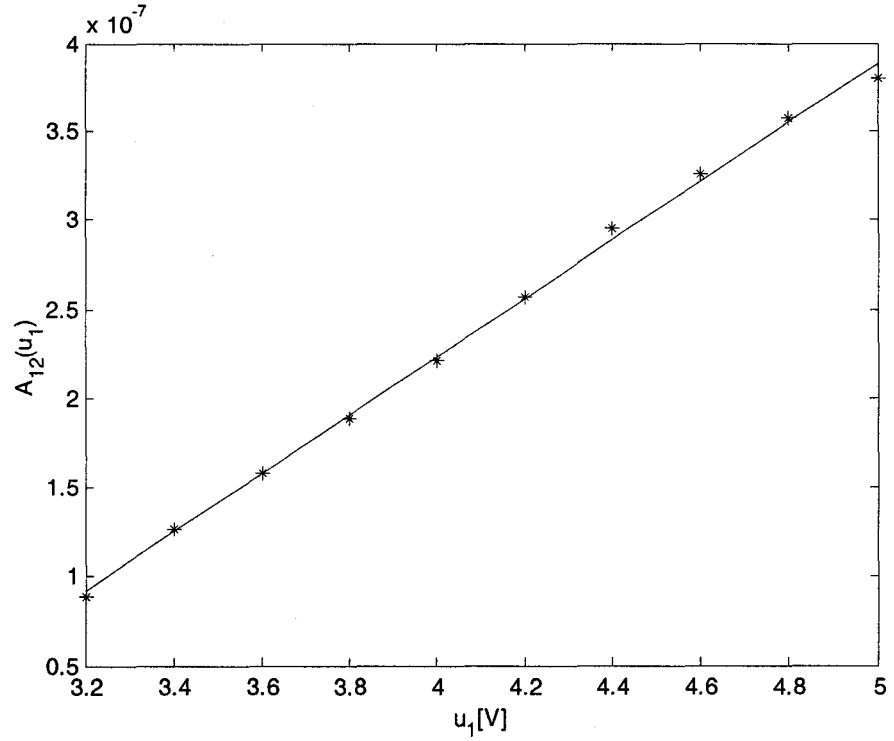

Figure 3.4.8: Curve fitting of $A_{12}(u_1)$.

In summary, the mass flow rate model of valve 1 is obtained as equations (3.4.5)~(3.4.8). Since curve fitting method is used, the coefficients in the fitting results have no physical meaning. When substituting values into the curve fitting equations, voltage value and pressure value are in units of [V] and [Pa], and the resulting mass flow rate value is in unit of [kg/s] The surface of the fitted model is shown in Figure 3.4.9

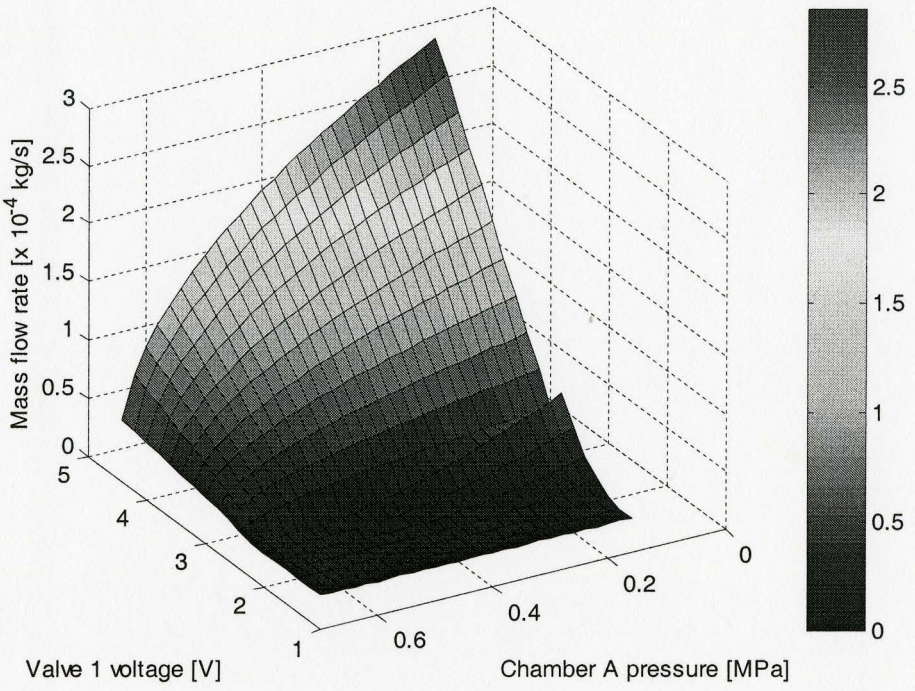

Figure 3.4.9· Sectional curve fitting result for mass flow rate of valve 1

3.4.2.2 Surface fitting method

Since the flow rate measurement is represented by a surface, it can be directly fitted in a surface. The website http://www.zunzun.com [43] provides a wide range of function candidates and fitting targets for curve and surface fitting. The measured surface shown in Figure 3.4.5 was down-sampled at a series of fixed pressure points by linear interpolation to reduce the data size. The data were sent to the website for surface fitting with different function candidates. The fitting target was lowest sum of squared absolute errors. From the results provided the measured surface can be well fitted by bipolynomials. High order bipolynomials fitted the noise in addition to the signal. For noise reduction, a second order bipolynomial function was selected for the fitting result as follows:

$$\begin{aligned}\dot{m}_1 = {} & a_1 + b_1 u_1^{\,0} P_a^{\,1} + c_1 u_1^{\,0} P_a^{\,2} + d_1 u_1^{\,1} P_a^{\,0} + e_1 u_1^{\,1} P_a^{\,1} + f_1 u_1^{\,1} P_a^{\,2} \\ & + g_1 u_1^{\,2} P_a^{\,0} + h_1 u_1^{\,2} P_a^{\,1} + i_1 u_1^{\,2} P_a^{\,2}\end{aligned} \tag{3.4.9}$$

The coefficients for valve 1 are:

$a_1 = -1.0191\text{x}10^{-04}$; $b_1 = 5.5755\text{x}10^{-10}$; $c_1 = -6.1582\text{x}10^{-16}$; $d_1 = 5.8982\text{x}10^{-05}$; $e_1 = -5.2252\text{x}10^{-10}$; $f_1 = 6.5239\text{x}10^{-16}$; $g_1 = 2.0092\text{x}10^{-07}$; $h_1 = 1.0054\text{x}10^{-10}$ and $i_1 = -1.4980\text{x}10^{-16}$.

In equation (3.4.9), voltage, pressure and mass flow rate have the units of [V], [Pa] and [kg/s], respectively. The fitted surface is shown in Figure 3.4.10.

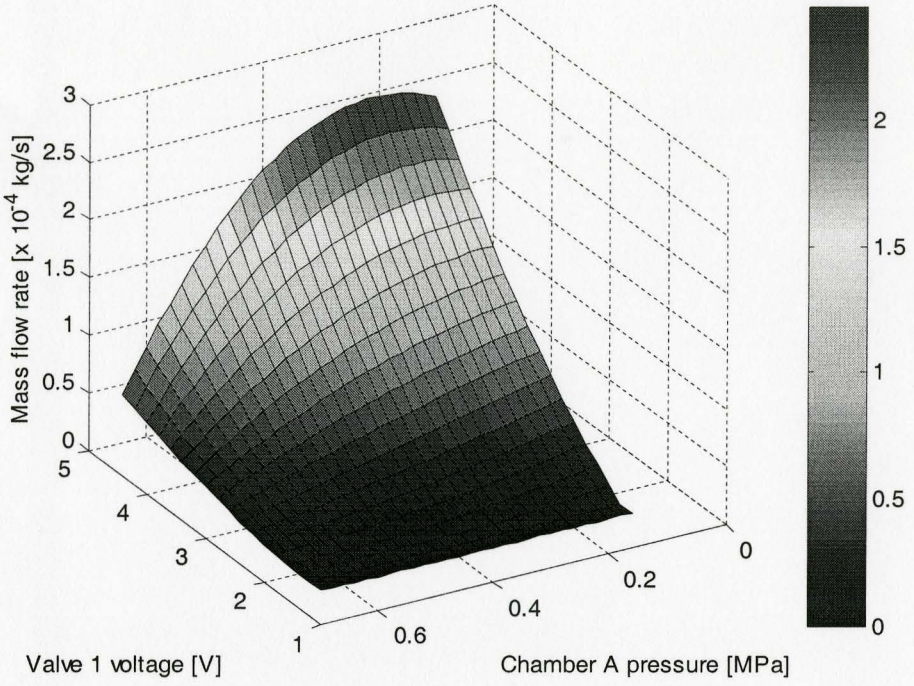

Figure 3.4.10· Bipolynomial surface fitting result for mass flow rate of valve 1

3.4.2.3 Comparison of the two fitting methods

The mass flow rates of the four valves were all modeled by the two methods. The two methods are compared considering the fitting accuracy and the ease of use. Two indexes are used for comparison. They are the root of the mean square error (RMSE) and the relative error

$$\text{RMSE} = \sqrt{\frac{1}{n}\sum_{i=1}^{n} e_i^{\,2}} \tag{3.4.10}$$

$$\text{Relative error } \varepsilon = \left| \frac{\dot{m}_{1\,fit} - \dot{m}_{1measured}}{\dot{m}_{1measured}} \right| \times 100\% \tag{3.4.11}$$

The RMSE value indicates the average error over the surface while the relative error applies to a single point.

The RMSE values are listed in Table 3.4.1. They were obtained using the down-sampled voltage-pressure mesh described previously. The maximum mass flow rates and the relative errors at the maximum flow rates are listed in Table 3.4.2. They were obtained by taking the maximum value of the surface. They correspond to the maximum valve opening (5V) and lowest chamber pressure for the charging valves (V1 and V3) or the highest chamber pressure for the discharging valves (V2 and V4). The relative errors at the maximum flow rates are listed in bracket.

Table 3.4.1: Comparison of the RMSE values for valve 1 modeling (unit: 10^{-5} kg/s).

	Valve1	**Valve2**	**Valve3**	**Valve4**
Sectional curve fitting	1.29	0.56	1.00	7.32
Bipolynomial surface fitting	1.04	0.48	0.79	7.68

Table 3.4.2: Comparison of the maximum flow rates (unit: 10^{-4} kg/s).

	Valve1	**Valve2**	**Valve3**	**Valve4**
Measurement	2.46	2.26	2.99	1.53
Sectional curve fitting	2.86 (16.30%)	2.59 (14.54%)	2.88 (3.82%)	1.31 (14.21%)
Bipolynomial surface fitting	2.46 (0.069%)	2.56 (13.26%)	3.00 (0.31%)	1.62 (6.25%)

From the data listed above it is found that the bipolynomial surface fitting is better than the sectional curve fitting in terms of both the RMSE values and relative errors. In addition, the bipolynomial surface fitting gives a smooth surface and the model equation is simpler than that of the sectional curve fitting, which will give less computational load

in the controller. For the remainder of this thesis the bipolynomial model will be used for the valves. The model coefficients for valves 2-4 are given in Appendix A.

3.4.3 Back-solving the flow rate model

The mass flow rate model of each valve is represented by a 2nd order bipolynomial function. Implementing the controller will require solving the applied voltage for a desired mass flow rate under a certain chamber pressure. For example, model of valve 1, equation (3.4.9) is a quadratic equation in u_1 when the desired flow rate $\dot{m}_{1d}$ and P_a are given. Equation (3.4.9) can be rearranged as

$$C_{21}u_1^2 + C_{11}u_1 + C_{01} = 0 \tag{3.4.12}$$

where $C_{21} = g_1 + h_1P_a + i_1P_a^2$, $C_{11} = d_1 + e_1P_a + f_1P_a^2$ and $C_{01} = a_1 + b_1P_a + c_1P_a^2 - \dot{m}_{1d}$. Generally u_1 could have 2 solutions as

$$\begin{aligned} u_{11} &= \frac{-C_{11} + \sqrt{C_{11}^2 - 4C_{21}C_{01}}}{2C_{21}} \\ u_{12} &= \frac{-C_{11} - \sqrt{C_{11}^2 - 4C_{21}C_{01}}}{2C_{21}} \end{aligned} \tag{3.4.13}$$

Since the model represents the surface shown in Figure (3.4.10), the three variables have a one-to-one correspondence in the working range. Thus u_1 can be uniquely solved from the quadratic equation, which means only one of u_{11} and u_{12} is the control voltage we desire. The two back-solving solutions in (3.4.13) were checked over the mesh of the whole working condition range, i.e., pressure of 0.1-0.65 MPa and voltage of 1.6-5 V. The checking procedure is as follows:

(1) For each pair of given voltage and pressure values on the mesh, calculate the mass flow rate by the bipolynomial function (3.4.9).

(2) Use (3.4.13) to calculate two back-solved voltages based on the given pressure value and the mass flow rate value obtained in step (1).

(3) Compare the two back-solved voltage values with the given one in step (1). The back-solved voltage close to the given one is the right back-solving solution.

It was found that there are three regions as shown in Figure 3.4.11. In region 1, only the solution u_{11} falls into the range of 1.6-5 V. So u_{11} is taken as the back-solving solution. In region 2, two solutions fall into the range of 1.6-5 V. But only u_{11} is in region 2 (bigger than 2 V). So u_{11} is taken as back-solving solution. In region 3, the mass flow-rate is zero; the control voltage is simply set to be zero. In the implementation, it can be set to be the dead zone voltage (1.6 V for valve 1) for better dynamic performance. Note that at the boundary of region 1, the back-solving solution exceeds 5V at some points due the numerical error. In this case, the solution is set to be 5V. From these observations the back-solving procedure is as follows, given the chamber pressure P_a measurement and the desired flow rate $\dot{m}_{1d}$:

(1) If $\dot{m}_{1d}$ is zero, set u_1 as 1.6V;

(2) If $\dot{m}_{1d}$ is bigger than the maximum flow rate value listed in Table 3.4.2, set u_1 as 5V;

(3) Other wise, set u_1 as u_{11} obtained in (3.4.13).

The back-solving procedures are similar for the other valves. The coefficients of the bipolynomial function, voltage and pressure variables should be replaced by the

corresponding ones. For valve 1 and valve 2, the pressure is P_a while for valve 3 and valve 4 the pressure is P_b.

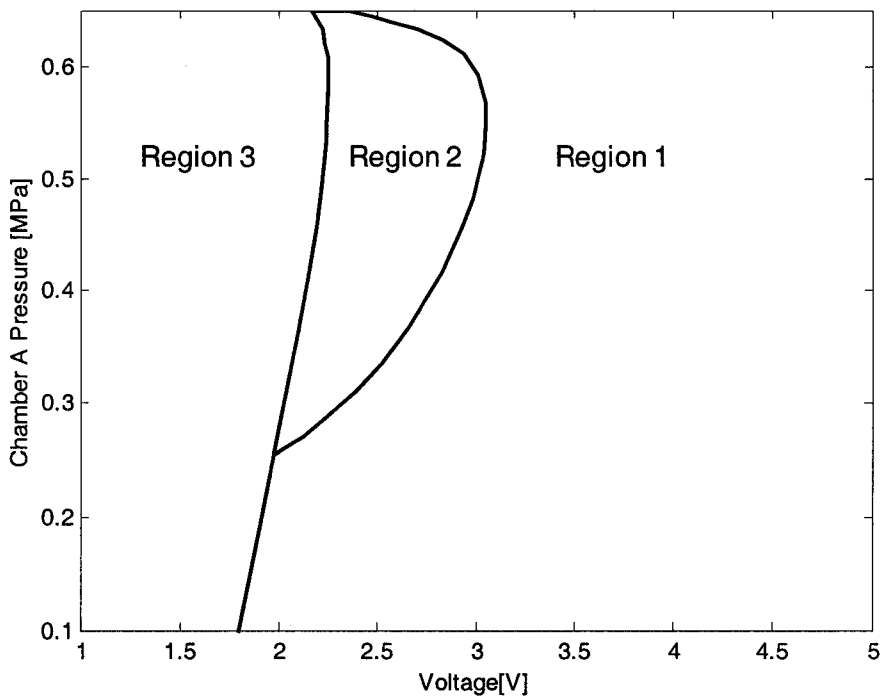

Figure 3.4.11: Regions for back-solving control voltage of valve 1.

3.5 Friction model

Friction appears in all mechanical systems. In the pneumatic servo system in this study, the friction is mainly due to contact between the piston seals and the cylinder wall. The sliding of the rod, the LVDT sensor and slide table supporting the payload also contribute to the friction force.

Usually the friction is a nonlinear function of the relative velocity of the two surfaces in contact. We will employ the classical static friction model. This model is represented as

$$F_f = \begin{cases} \left[F_c + (F_s - F_c)e^{-(v/v_s)^2}\right]\mathrm{sgn}(v) + F_v v & \text{if } v \neq 0 \\ F_{ext} & v = 0 \text{ and } |F_{ext}| < F_s \\ F_s\,\mathrm{sgn}(F_{ext}) & \text{otherwise} \end{cases} \tag{3.5.1}$$

where sgn(.) is the signum function,

$$\mathrm{sgn}(v) = \begin{cases} 1 & \text{if } v > 0 \\ 0 & \text{if } v = 0 \\ -1 & \text{if } v < 0 \end{cases} \tag{3.5.2}$$

In this model, F_c is the Coulomb friction force, F_s is the stiction force, F_v is the viscous friction coefficient, and v_s is the Stribeck velocity. F_{ext} is the resultant external force excluding friction. The friction depends on the moving velocity v. When the object moves, the friction includes the Coulomb friction and the viscous friction. The Stribeck effect is obvious only when the velocity is low. When the object is stationary, the friction force cancels the external force if it is less than the stiction, otherwise, the object will begin to move.

A velocity-friction map is needed to identify the four parameters: F_c, F_s, F_v and v_s. Open loop tests were performed on the system in the horizontal position with different input signals to the valves and different initial chamber pressures. The pressure data P_a, P_b and the position data y were recorded. The velocity and acceleration were obtained from the numerical central difference. All data were smoothed by the MATLAB function `filtfilt()` with a Butterworth low-pass filter. The cut-off frequency of low-pass filter was manually for each data set tuned to smooth out the noise ripples. The result from one experiment is shown in Figure 3.5.1.

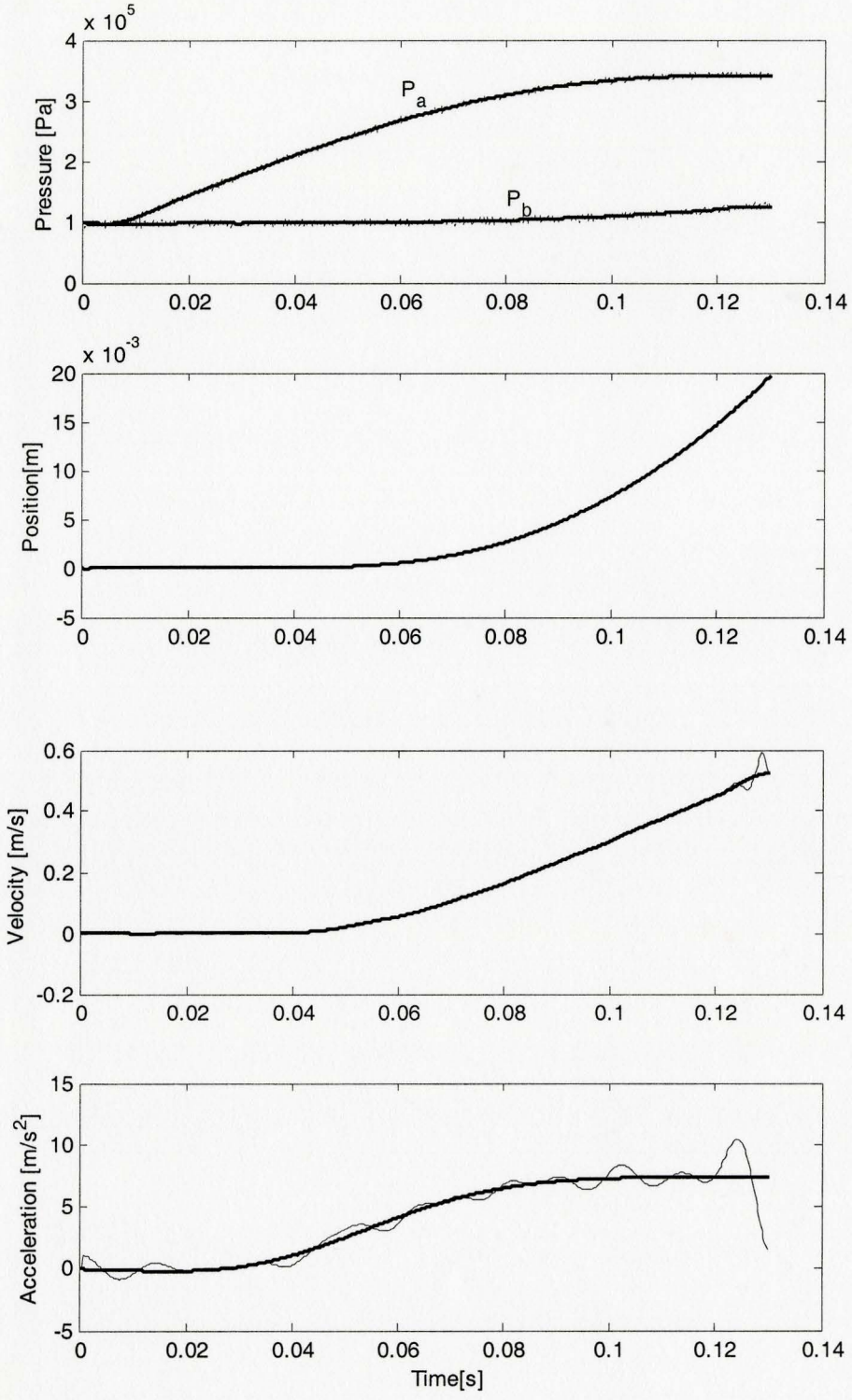

Figure 3.5.1 Pressure measurement, position measurement, velocity estimate and acceleration estimate from one friction modeling experiment.

The friction is estimated from the system dynamic equation,

$$F_f = P_a A_a - P_b A_b - P_0 A_{rod} - M\hat{a} \tag{3.5.3}$$

where $\hat{a}$ is the acceleration estimate. The velocity-friction map from four experiments is shown in Figure 3.5.2. The data in Figure 3.5.2 were averaged over the velocity range. The velocity range of 0-0.4 m/s was divided into a series of small intervals. A smaller interval size was used in the low velocity range (less than 0.01 m/s) for a better Stribeck velocity estimation. The data in Figure 3.5.2 were registered into these intervals and averaged to get the average velocity-friction map, given in Figure 3.5.3 Nonlinear least square fitting was used to fit the data in Figure 3.5.3 to equation (3.5 1). The fitting goal was to find the four friction parameters that minimized the sum of squared fitting errors. The MATLAB optimization toolbox was used. First, the initial guesses for the four parameters were obtained from the data in Figure 3.5.3 as. $F_c = 3.5[N]$, $F_s = 5.6[N]$, $F_v = 6[N/m/s]$, $v_s = 0.1[m/s]$ Next The MATLAB command `lsqnonlin` was used to search for the parameter estimates. The optimization options were left with the default values. The results are $F_c = 3\ 15[N]$, $F_s = 5.66[N]$, $F_v = 5.68[N/m/s]$ and $v_s = 0.098[m/s]$ The model is shown in Figure 3.5.3 as a solid line. With other initial guess and other options the results were similar

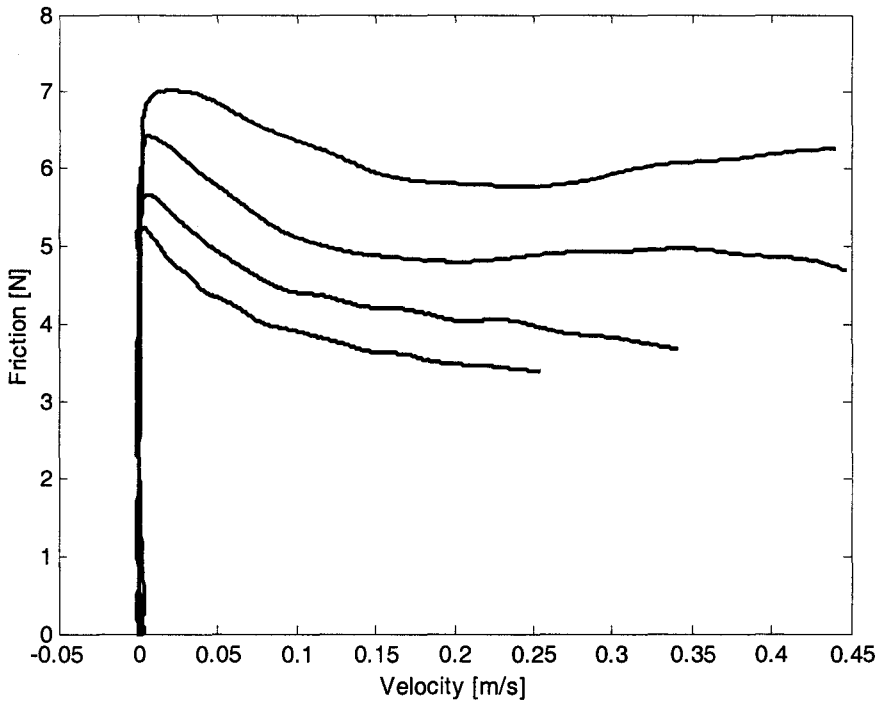

Figure 3.5.2: The velocity-friction map from 4 experiments.

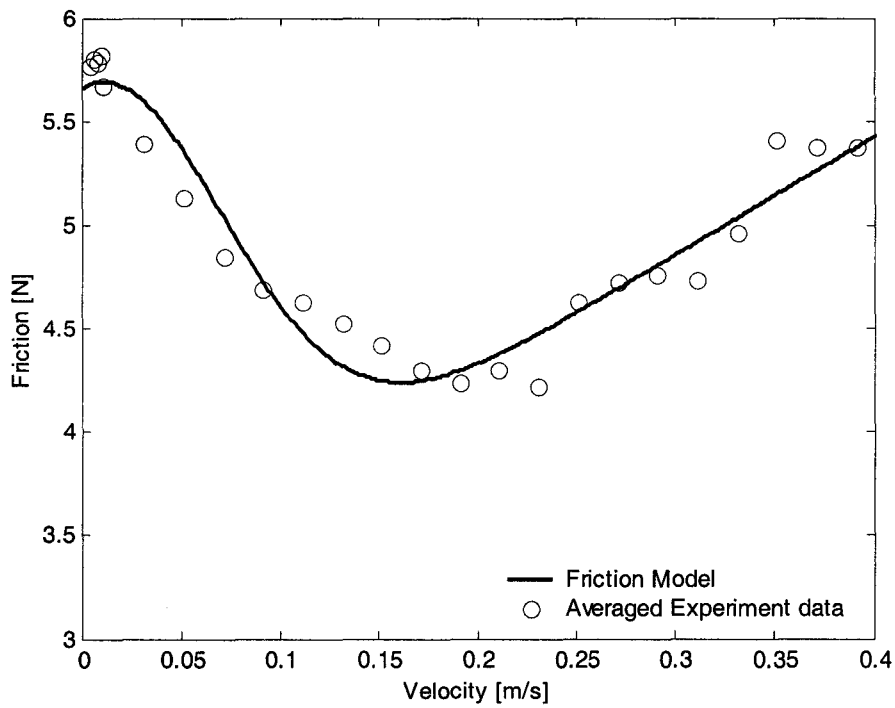

Figure 3.5.3: Average friction-velocity map and the fitted model.

3.6 Open loop validation of the model

In the previous sections the system model has been derived in detail, and the unknown parameters have been identified. This section compares the open loop model simulation and the experiment result. The model simulation involves the following steps:

(1) Choose the initial piston position and chamber pressures.

(2) Obtain the mass flow rate for each valve from the bipolynomial model (3.4.8) using the given valve voltages and the chamber pressures.

(3) From (3.3.12) and (3.3.13) obtain the chamber flow rate; then from (3.3.10) and (3.3.11) calculate the pressure derivatives.

(4) Calculate chamber pressures P_a and P_b using digital integration.

(5) Calculate the acceleration from (3.3.18).

(6) Calculate the velocity and position using digital integration.

To examine the model over a wide range, the control signals were given as the clipped sine waves shown in Figure 3.6.1. The same control signals were also used for the experiment. The simulation and experiment results are compared in Figure 3.6.2. The simulation data is consistent with the experiment data. It demonstrates that the system model predicts the static and dynamic behavior of the real system well.

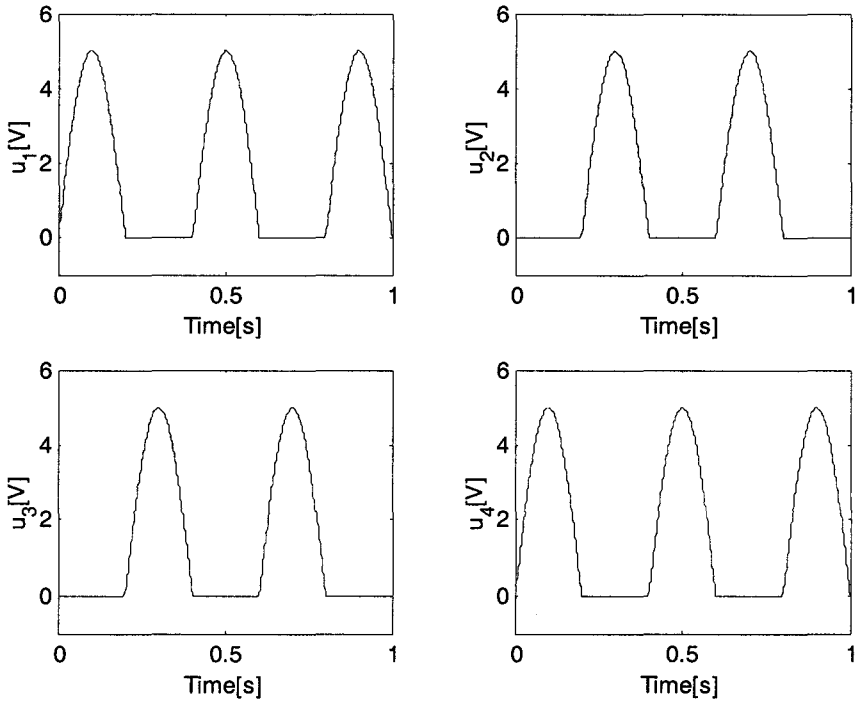

Figure 3.6.1: Control signals used for open loop validation.

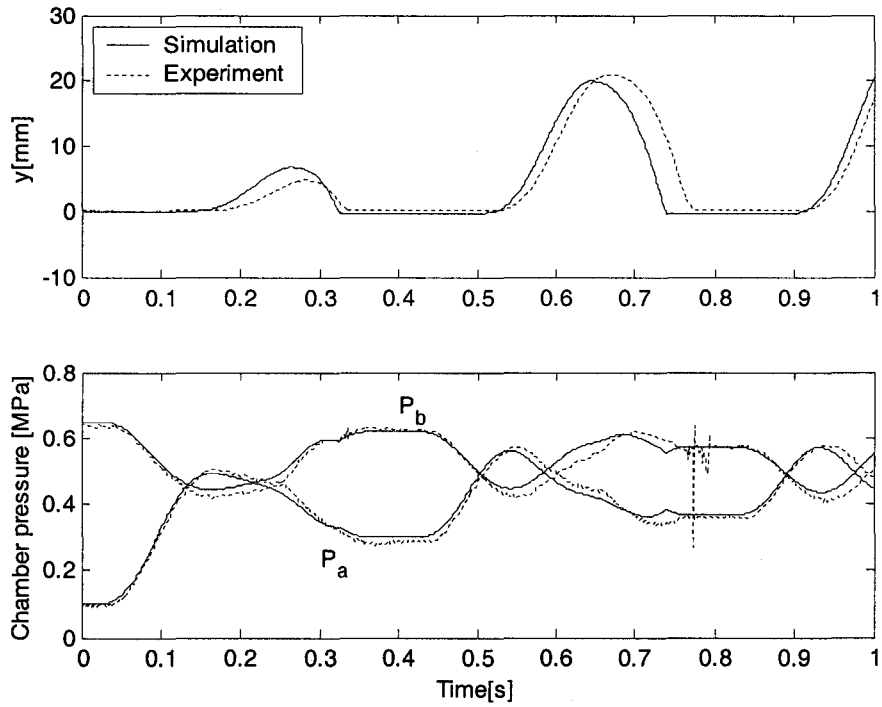

Figure 3.6.2: Comparison of open loop simulation and experiment.

3.7 Conclusions

The system model was derived in this chapter. The mathematical equations were derived based on physical theories. The flow rate model of each valve was obtained based on the experimental data and two techniques were compared. The bipolynomial surface fitting method provided higher modeling accuracy than the sectional curve fitting method. The system model was validated by comparing simulation and experiment results. The results demonstrated that the model represents the system well.

CHAPTER 4

CONTROLLER DESIGN AND EXPERIMENTS

4.1 Introduction

The design and implementation of three controllers are presented in this chapter A PVA controller is presented first. Next, two nonlinear controllers, based on inverse dynamics and backstepping respectively, are designed, simulated and experimentally tested. The detailed design procedures are described.

4.2 Linear PVA controller design and experiment

This section introduces a single-input single-output (SISO) linear controller implementation for performance comparison. In a SISO system the four control valves imitate a 4-way servo valve using the following strategy·

$$\begin{aligned} &u_1 = u, \quad u_2 = 0, \quad u_3 = 0, \quad u_4 = u \quad \text{if } u \geq 0 \\ &u_1 = 0, \quad u_2 = -u, \quad u_3 = -u, \quad u_4 = 0 \quad \text{if } u < 0 \end{aligned} \tag{4.2.1}$$

where u is a virtual control signal. In this strategy, assume positive u to extending the piston thus valve 1 (chamber A charging) and valve 4 (chamber B discharging) should be open and the other two be closed. On the other hand negative u should retract the piston thus the valves are operated oppositely

A conventional linear controller for pneumatic servo systems is the PVA controller Here the controller proposed by Ning and Bone [23] will be tested on the current system. This controller incorporates PVA feedback, feedforward compensation and DZC. The control structure is shown in Figure 4.2.1

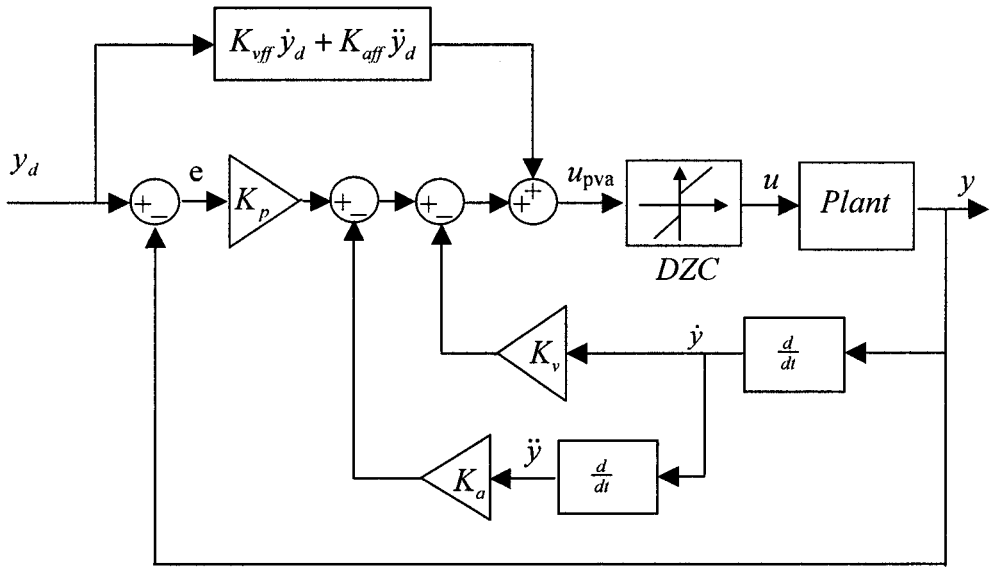

Figure 4.2.1: PVA+FF+DZC controller structure.

The controller gains were manually tuned as: $K_p = 350[V/m]$, $K_v = 15[V/m/s]$, $K_a = 0.5[V/m/s^2]$, $K_{vff} = 15[V/m/s]$ and $K_{aff} = 1.1[V/m/s^2]$. The DZC value was tuned as 2.5V, which compensates the valve dead zone and the friction. The DZC is applied as follow,

$$u = \begin{cases} u_{pva} + 2.5 & \text{if } u_{pva} \geq 0 \\ u_{pva} - 2.5 & \text{if } u_{pva} < 0 \end{cases} \tag{4.2.2}$$

where u_{pva} is the control signal calculated based on the controller structure shown in Figure 4.2.1.

In the PVA controller, velocity and acceleration are needed. Since direct velocity and acceleration measurements are not available, a velocity observer [44] is used,

$$\begin{aligned} \hat{v} &= z_v + K_v y \\ \dot{z}_v &= -K_v \hat{v} \end{aligned} \tag{4.2.3}$$

where $\hat{v} = \hat{\dot{y}}$ is the velocity estimate. This observer is actually a low-pass filtered differentiator. In fact, canceling the state z_v, one can obtain the transfer function,

$$\frac{\hat{v}}{y} = \frac{s}{\left(1/K_v\right)s + 1} \tag{4.2.4}$$

This transfer function is a differentiator in series with a unity-gain first order system acting as a low-pass filter. The time constant of the first order system is $1/K_v$. The observer gain K_v should be tuned to allow fast response and reasonable noise reduction. Also note that the bandwidth of the low-pass filter cannot exceed the half of the sampling frequency. The same observer is used to estimate the acceleration using the velocity estimate as the input.

Three trajectories, as listed in Table 4.2.1, were tested with this controller.

Table 4.2.1: Trajectories used for the PVA controller.

	Trajectory
1	Point-to-point (0 to 20 mm) with cycloidal rising in the first second
2	Ramp speed 5 mm/s
3	1 Hz sine wave with 7.5 mm amplitude

The experiment results are shown in Figures 4.2.2 to 4.2.4. It is found that in the step response the SSE is in the range of ±0.04 mm, but the system output zigzags around the desired trajectory during tracking. This is especially obvious in the ramp test (Figure 4.2.3). It shows a typical stick-slip phenomenon due to the stiction. Due to the small

stroke length, the system velocity is mostly in the Stribeck region, where a small velocity variation may cause big change in the friction force. Simple DZC cannot completely compensate the friction. The RMSE values of the three trajectories are 0.31 mm, 0.67 mm and 0.92 mm respectively.

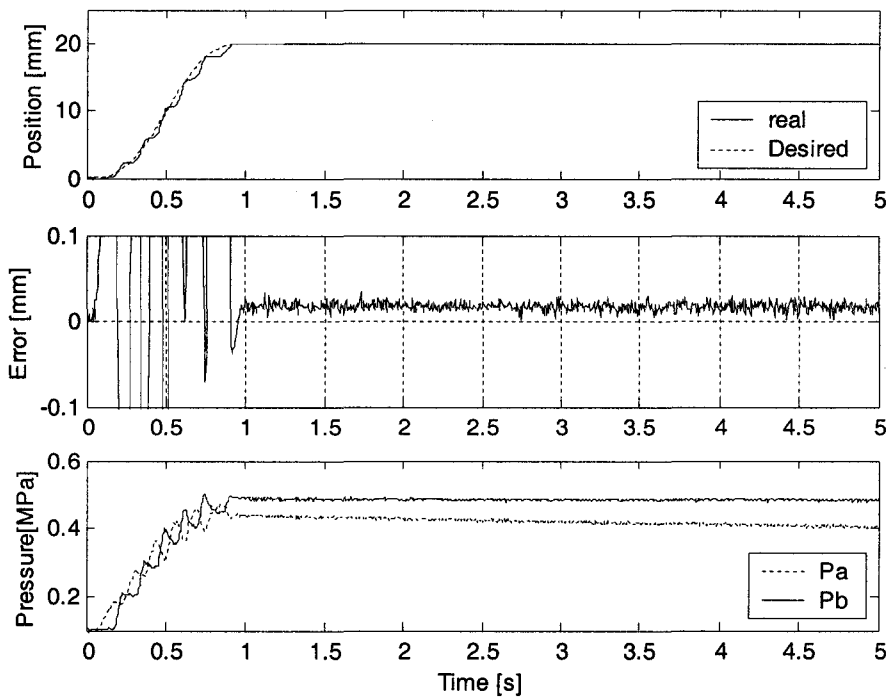

Figure 4.2.2: Trajectory 1 tracking experiment with PVA+FF+DZC controller.

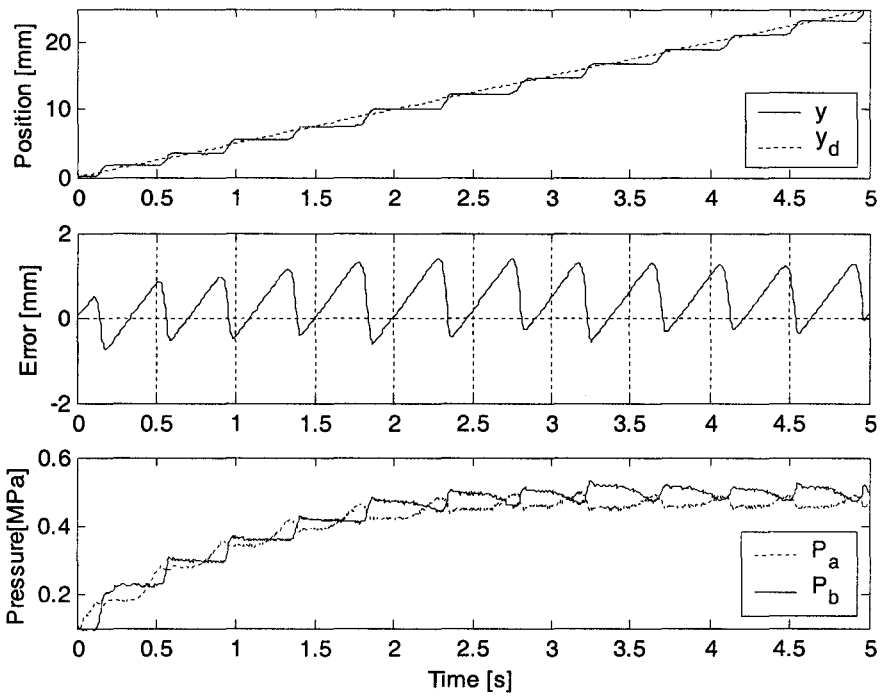

Figure 4.2.3: Trajectory 2 tracking experiment with PVA+FF+DZC controller.

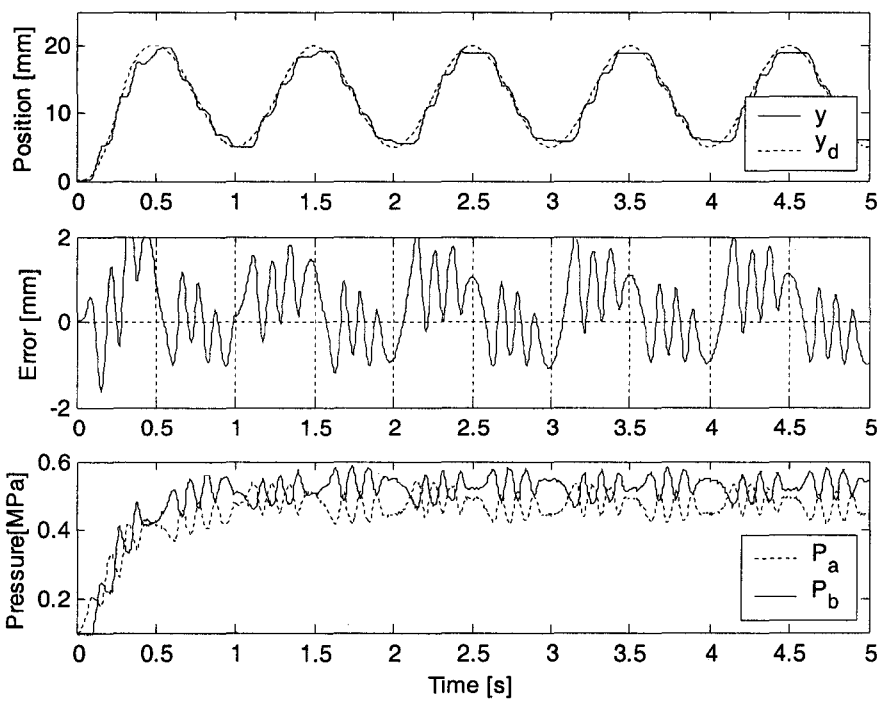

Figure 4.2.4: Trajectory 3 tracking experiment with PVA+FF+DZC controller.

4.3 Controller design using the inverse dynamics method

In this section a nonlinear controller is designed. The controller separates the force control subsystem and the position control subsystem. In each subsystem the inverse dynamics method [27] is used. Sohl and Bobrow [45] used similar approach for a hydraulic system with a servo valve. The design procedure is presented in detail. Simulation and experiment results are given.

4.3.1 Design procedure

The system model has been derived in chapter 3. The equations are listed below.

$$\dot{m}_1 = \eta_1(u_1, P_a) \tag{4.3.1}$$

$$\dot{m}_2 = \eta_2(u_2, P_a) \tag{4.3.2}$$

$$\dot{m}_3 = \eta_3(u_3, P_b) \tag{4.3.3}$$

$$\dot{m}_4 = \eta_4(u_4, P_b) \tag{4.3.4}$$

$$\dot{m}_a = \dot{m}_1 - \dot{m}_2 \tag{4.3.5}$$

$$\dot{m}_b = \dot{m}_3 - \dot{m}_4 \tag{4.3.6}$$

$$KRT\dot{m}_a = \left(KA_a\dot{y}\right)P_a + \left(A_a y + V_{a0}\right)\dot{P}_a \tag{4.3.7}$$

$$KRT\dot{m}_b = -\left(KA_b\dot{y}\right)P_b + \left[A_b(L-y) + V_{b0}\right]\dot{P}_b \tag{4.3.8}$$

$$M\ddot{y} = F_p - F_f - F_l - P_0 A_{rod} \tag{4.3.9}$$

where $\eta_1 \sim \eta_4$ are the nonlinear valve models (the bipolynomial functions), and

$$F_p = P_a A_a - P_b A_b \tag{4.3.10}$$

is the applied driven force.

The controller design strategy includes the following steps:

(1) Based on the motion equation (4.3.9), design a controller for tracking the desired trajectory using F_p as the input. Obtain the desired driven force F_{pd};

(2) Based on equation (4.3.10), distribute the desired driven force F_{pd} to the desired pressure of the two chambers, P_{ad} and P_{bd};

(3) Design separate pressure controllers for the two chambers using the chamber mass flow rate as the input signal. Obtain the desired mass flow rate for each chamber; and

(4) Use equation (4.3.5) and (4.3.6) to distribute the two desired mass flow rate to the four valves, then back-solve the valve voltage from equations (4.3.1)~(4.3.4).

The details of each step are given below.

Step (1):

Define tracking error as

$$e = y_d - y \tag{4.3.11}$$

and an auxiliary variable (or filtered error)

$$S = \dot{e} + \lambda e \tag{4.3.12}$$

where λ is a strictly positive number. The desired driven force is proposed as,

$$F_{pd} = M(\ddot{y}_d + \lambda \dot{e}) + K_s S + \hat{F}_f + F_l + P_0 A_{rod} \tag{4.3.13}$$

where K_s is a positive control gain to be tuned and $\hat{F}_f$ is the friction estimate. Define the friction estimate error that comes from the friction model as,

$$F_{fe} = F_f - \hat{F}_f \tag{4.3.14}$$

and the applied driven force error

$$F_{pe} = F_{pd} - F_p \tag{4.3.15}$$

Substituting these equations back into the dynamic model (4.3.9) one obtains,

$$M\dot{S} + K_s S = F_{fe} + F_{pe} \tag{4.3.16}$$

This is a linear first order system about S, driven by $F_{fe} + F_{pe}$. Since λ and K_s are both positive, the system is stable. It will be shown later in step 3 that $F_{pe} \to 0$ as $t \to \infty$ if the valve models are accurate. If the friction model is accurate then $F_{fe} = 0$. When the input to the first order system vanishes, the output also vanishes, i.e., $S \to 0$ as $t \to \infty$. From equation (4.3.12), $e \to 0$ as $t \to \infty$. If these errors are bounded, e.g., $\|F_{fe}\| < \varepsilon_1$ and $\|F_{pe}\| < \varepsilon_2$, S is bounded by $\frac{\varepsilon_1+\varepsilon_2}{K_s}$ thus output e is bounded by $\frac{\varepsilon_1+\varepsilon_2}{\lambda K_s}$.

In chapter 3 the friction was modeled as a nonlinear function with respect to the velocity. Due to the short stroke of the cylinder and its friction behavior, the velocity tends to stay in the Stribeck region where small changes in the velocity produce large changes in the friction force. It is well known that velocity estimates are noisy, so we use feedforward friction compensation [46] where the velocity of the moving mass in (3.5.1) is replaced by the desired velocity. The friction estimate is obtained as,

$$\hat{F}_f = \begin{cases} \left[F_c + (F_s - F_c)e^{-(v_d/v_s)^2}\right]\operatorname{sgn}(v_d) + F_v v_d & \text{if } |v_d| > v_{th} \\ F_{ext} & |v_d| \le v_{th} \text{ and } |F_{ext}| < F_s \\ F_s \operatorname{sgn}(F_{ext}) & |v_d| \le v_{th} \text{ and } |F_{ext}| \ge F_s \end{cases} \tag{4.3.17}$$

where $F_{ext} = F_p - F_l - P_0 A_{rod}$. Here a velocity threshold v_{th} is used. If velocity is smaller than the threshold, the system is assumed to be stationary.

Step (2):

The desired driven force was derived in (4.3.13). Based on (4.3.10), the desired chamber pressures need to satisfy,

$$P_{ad} A_a - P_{bd} A_b = F_{pd} \tag{4.3.18}$$

Another constraint on P_{ad} and P_{bd} is necessary to determine their values. One way is to let P_{ad} and P_{bd} vary in the middle of the full pressure range, as shown in Figure 4.3.1. In this method, the pressure change is evenly distributed to the two chambers, and subsequently to the four valves. The same maximum applied force, thus acceleration, can be obtained evenly in both directions. Other objectives, *e.g.* stiffness control, can be implemented here. From Figure 4.3.1 we have,

$$P_s - P_{ad} = P_{bd} - P_0 \tag{4.3.19}$$

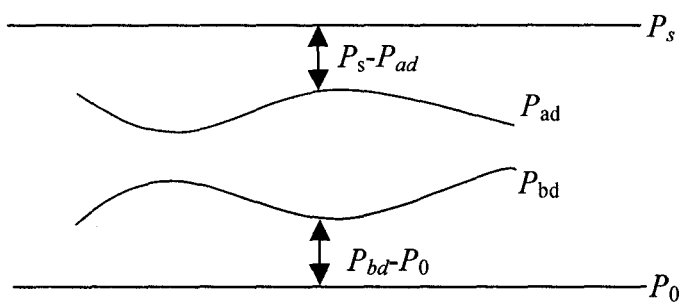

Figure 4.3.1: A constraint on P_{ad} and P_{bd}.

From (4.3.18) and (4.3.19) one can solve for P_{ad} and P_{bd} to yield

$$P_{ad} = \frac{A_b\left(P_s + P_0\right) + F_{pd}}{A_a + A_b} \tag{4.3.20}$$

$$P_{bd} = \frac{A_a\left(P_s + P_0\right) - F_{pd}}{A_a + A_b} \tag{4.3.21}$$

Step (3):

In the previous step the desired chamber pressures were obtained. Now, two pressure controllers will be designed to track the desired pressures. First, the pressure controller for chamber A is derived. We rearrange the pressure dynamics in (4.3.7) as,

$$\left(\frac{A_a\dot{y}}{RT}\right)P_a + \left(\frac{A_a y + V_{a0}}{KRT}\right)\dot{P}_a = \dot{m}_a \tag{4.3.22}$$

If the two coefficient terms of P_a and $\dot{P}_a$ are considered to be pointwise [47], i.e., they are frozen in time at each point in time, this is a time-varying first order system with $\dot{m}_a$ as input and P_a as output. Define the pressure tracking error,

$$e_{pa} = P_{ad} - P_a \tag{4.3.23}$$

The desired chamber A flow rate is proposed as,

$$\dot{m}_{ad} = \left(\frac{A_a\dot{y}}{RT}\right)P_a + \left(\frac{A_a y + V_{a0}}{KRT}\right)\left(\dot{P}_{ad} + \Lambda_a e_{pa}\right) \tag{4.3.24}$$

where Λ_a is a strictly positive gain to be tuned. Substituting (4.3.23) and (4.3.24) into (4.3.22) and rearranging it gives,

$$\dot{e}_{pa} + \Lambda_a e_{pa} = \frac{e_{\dot{m}_a}}{\left(\frac{A_a y + V_{a0}}{KRT}\right)} \tag{4.3.25}$$

where

$$e_{\dot{m}_a} = \dot{m}_{ad} - \dot{m}_a \tag{4.3.26}$$

is the mass flow rate error that comes from the valve model inaccuracy.

Similarly, the flow rate for chamber *B* is designed as,

$$\dot{m}_{bd} = \left(-\frac{A_b \dot{y}}{RT}\right) P_b + \left(\frac{A_b(L-y)+V_{b0}}{KRT}\right)\left(\dot{P}_{bd} + \Lambda_b e_{pb}\right) \tag{4.3.27}$$

where

$$e_{pb} = P_{bd} - P_b \tag{4.3.28}$$

is the pressure tracking error for chamber *B*. The pressure tracking error dynamic is,

$$\dot{e}_{pb} + \Lambda_b e_{pb} = \frac{e_{\dot{m}_b}}{\left(\frac{A_b(L-y)+V_{b0}}{KRT}\right)} \tag{4.3.29}$$

The dynamics of e_{pa} and e_{pb} are first order. If the mass flow rate modeling error of the four valves are zero, the chamber mass flow rate errors $e_{\dot{m}_a}$ and $e_{\dot{m}_b}$ are also zero. Recall that Λ_a and Λ_b are strictly positive, e_{pa} and e_{pb} will vanish exponentially, thus $F_{pe} \to 0$ as $t \to \infty$. If the mass flow rate error of the four valves are bounded, $e_{\dot{m}_a}$ and $e_{\dot{m}_b}$ are also bounded. The two pressure errors, e_{pa} and e_{pb}, are bounded, thus F_{pe} is bounded.

When calculate the desired mass flow rate for the two chambers using (4.3.24) and (4.3.27), the derivatives of the desired chamber pressure, $\dot{P}_{ad}$ and $\dot{P}_{bd}$, are required. From (4.3.20) we have, $\dot{P}_{ad} = \dot{F}_{pd}/(A_a + A_b)$. Then from (4.3.13) we can obtain,

$$\dot{P}_{ad} = \frac{M(\dddot{y}_d + \lambda\ddot{e}) + K_s\dot{S} + \dot{\hat{F}}_f}{A_a + A_b} \tag{4.3.30}$$

From (4.3.20) and (4.3.21) we have,

$$\dot{P}_{bd} = -\dot{P}_{ad} \tag{4.3.31}$$

Here, the derivative of the friction estimate is required. From equation (4.3.17), the friction estimate is discontinuous when $|v_d| \le v_{th}$. This is due to the definition of friction in the vicinity of zero velocity. In practice, numerical differentiation is adequate for this range.

Step (4):

The expressions for the desired mass flow rate for the two chambers have been obtained. The net flow rate of a chamber is the difference between the charging flow rate and the discharging flow rate. For each chamber we use two 2-way valves to emulate a 3-way valve. The desired flow rate of chamber *A* is distributed to the two valves as follows:

$$\dot{m}_{1d} = \begin{cases} \dot{m}_{ad} & \dot{m}_{ad} > 0 \\ 0 & \dot{m}_{ad} \le 0 \end{cases} \tag{4.3.32}$$

$$\dot{m}_{2d} = \begin{cases} 0 & \dot{m}_{ad} > 0 \\ -\dot{m}_{ad} & \dot{m}_{ad} \le 0 \end{cases} \tag{4.3.33}$$

Similarly the desired flow rate of chamber *B* is distributed using,

$$\dot{m}_{3d} = \begin{cases} \dot{m}_{bd} & \dot{m}_{bd} > 0 \\ 0 & \dot{m}_{bd} \le 0 \end{cases} \tag{4.3.34}$$

$$\dot{m}_{4d} = \begin{cases} 0 & \dot{m}_{bd} > 0 \\ -\dot{m}_{bd} & \dot{m}_{bd} \le 0 \end{cases} \tag{4.3.35}$$

Once the desired flow rates are obtained for the four valves, the control voltages can be obtained from the back-solving method described previously in section 3.4.3.

4.3.2 Simulation results

The designed controller was simulated with the four trajectories listed in Table 4.3.1. In the simulation, the controller gains were manually tuned based on the system model developed in chapter 3, including the four valve models. The friction model was assumed to be perfect in the simulation. The goals of tuning the gains were maximizing the controller gains and thus reducing the tracking errors, without causing system instability.

The tuned position controller gains were $\lambda = 70[\mathrm{s}^{-1}]$, $K_s = 100[\mathrm{kg}\cdot\mathrm{s}^{-1}]$. The pressure controller gains were $\Lambda_a = \Lambda_b = 500[\mathrm{s}^{-1}]$. The velocity observer gain was $K_v = 200[\mathrm{s}^{-1}]$, corresponding to a 31 Hz low-pass filter on the backward differenced result from the position measurement. The simulation results are shown in Figures 4.3.2 to 4.3.5. In each simulation the position tracking error, the chamber pressure and the pressure tracking errors are shown.

Table 4.3.1: Trajectories used for the nonlinear controllers.

	Trajectory
1	Point-to-point (0 to 20 mm) with cycloidal rising in the first second
2	Ramp speed 5mm/s
3	1 Hz sine wave with 7.5 mm amplitude
4	2 Hz sine wave with 2.5 mm amplitude

From the simulation results it is found that the controller has satisfactory performance. The SSE of the step response is in the range of ±0.02 mm, as in Figure 4.3.2. The main reason for this SSE is due to the friction model at the vicinity of zero velocity. In the ramp test the tracking error tends to zero after a short transient period of 0.2 seconds. In the steady state the pressure difference between the two chambers is constant, the applied force totally matches the friction force and keeps the velocity of the payload constant. In the sine trajectory tracking shown in Figures 4.3.4 and 4.3.5, the tracking error is in the range of ±0.2 mm except during the initial rise. It is found that the tracking error has peaks when the velocity changes sign. The pressure tracking also have peak error at the corresponding instant. This is due to the maximum flow rate limitation of the valves, which will be further discussed in section 5.4.

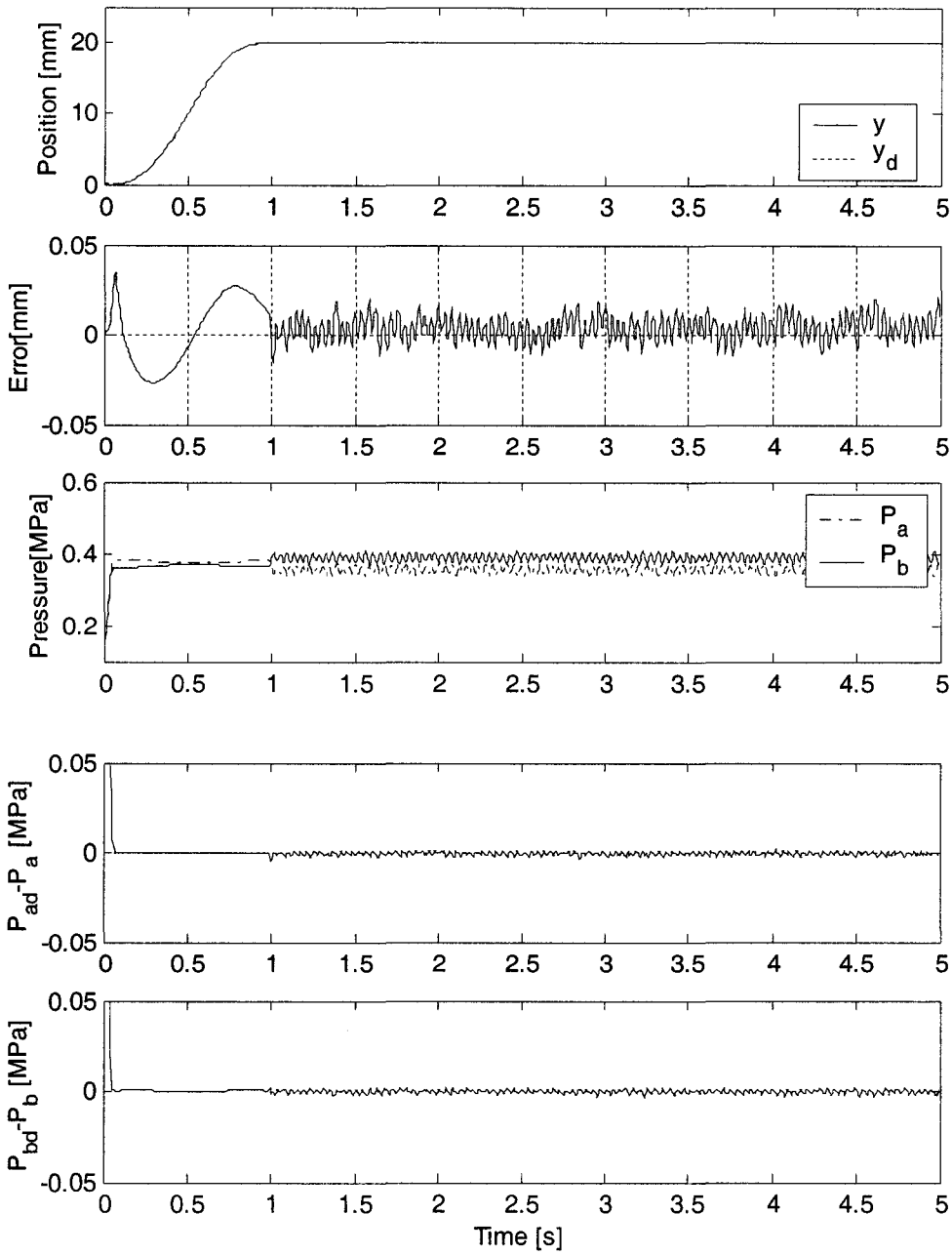

Figure 4.3.2: Trajectory 1 simulation with the inverse dynamics controller.

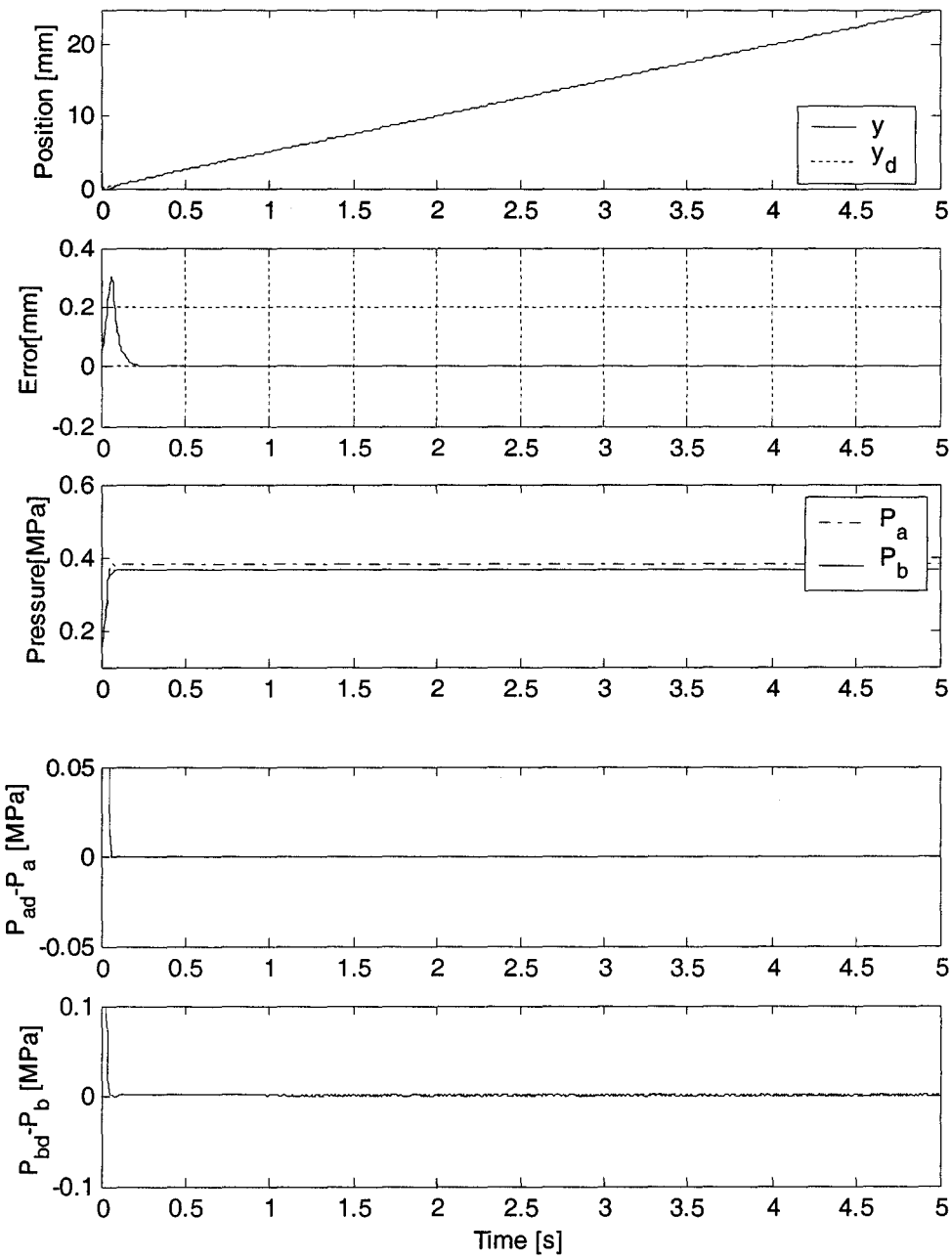

Figure 4.3.3: Trajectory 2 simulation with the inverse dynamics controller.

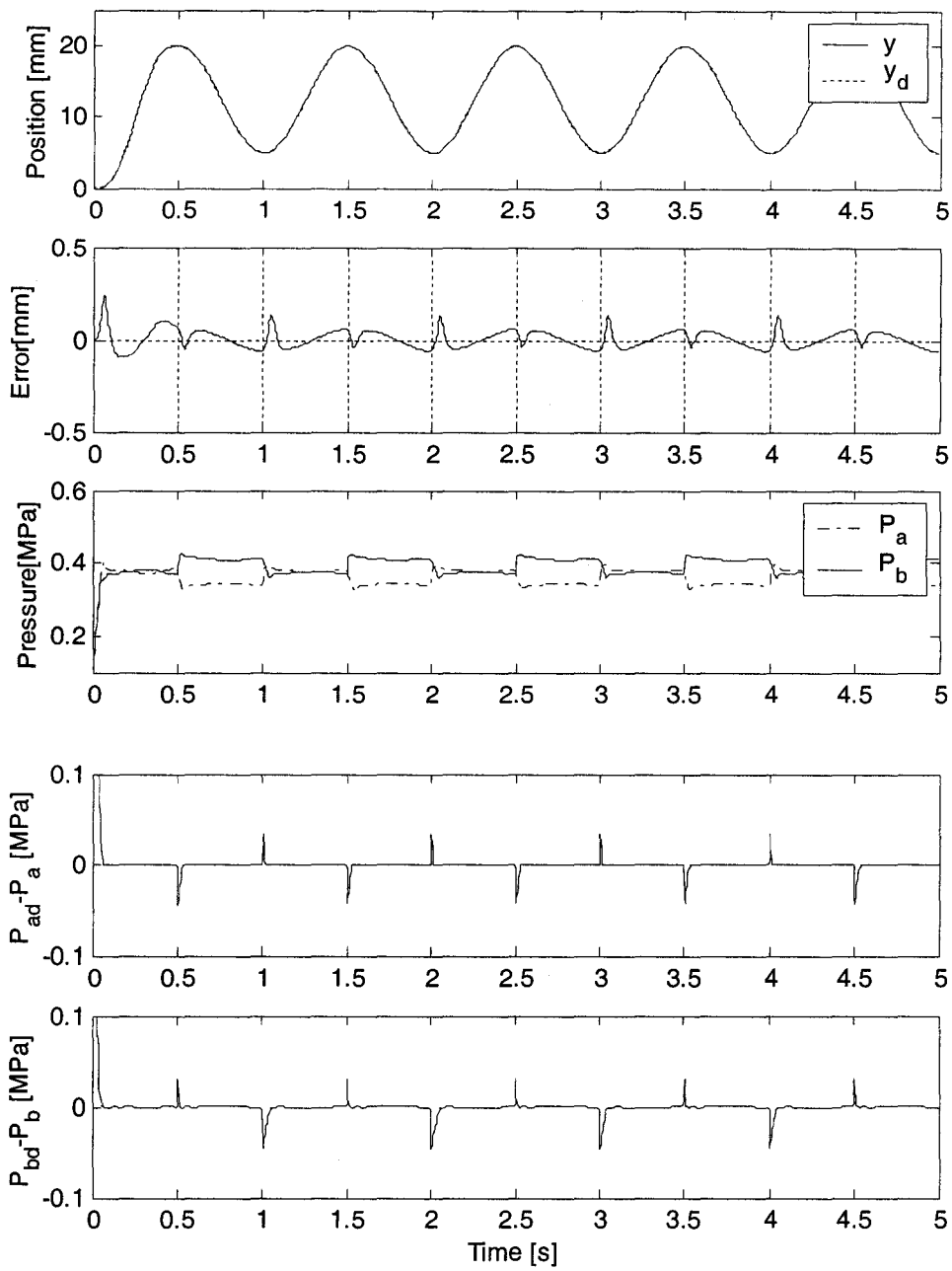

Figure 4.3.4: Trajectory 3 simulation with the inverse dynamics controller.

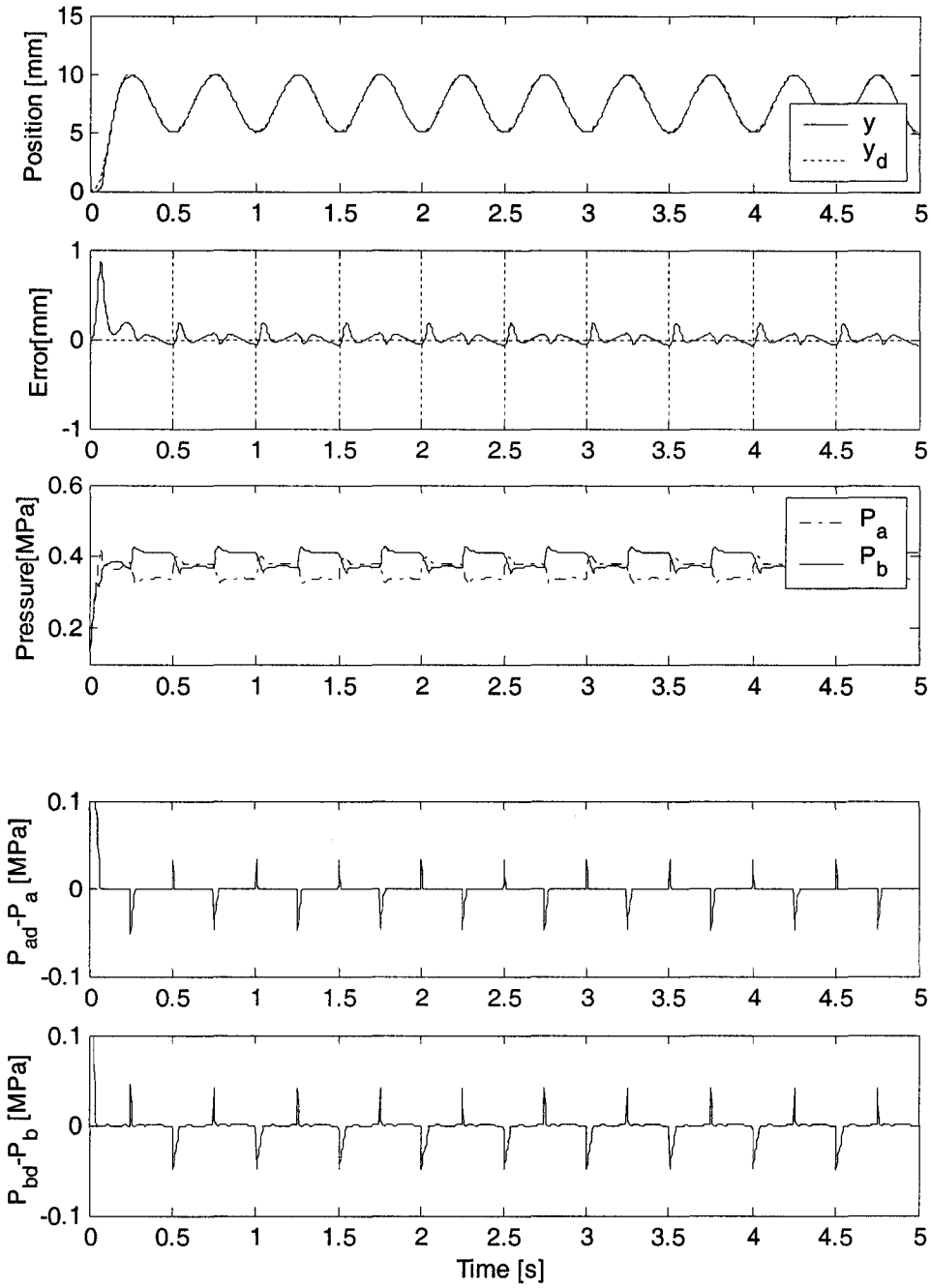

Figure 4.3.5: Trajectory 4 simulation with the inverse dynamics controller.

4.3.3 Experiment results

The proposed controller was implemented on the test system. The controller gains were manually tuned as follow. Position controller gains were $\lambda = 60[\mathrm{s}^{-1}]$, $K_s = 70[\mathrm{kg}\cdot\mathrm{s}^{-1}]$. Pressure controller gains were $\Lambda_a = \Lambda_b = 350[\mathrm{s}^{-1}]$. Velocity observer gain was $K_v = 200[\mathrm{s}^{-1}]$. The four trajectories listed in Table 4.3.1 were tested. The experiment results are shown in Figure 4.3.6 to Figure 4.3.9.

The experiment result of the step response (trajectory 1) is shown in Figure 4.3.6. The steady state error of trajectory 1 is within ±0.06 mm. This is due to the friction modeling at the zero velocity and the LVDT sensor noise. Figure 4.3.7 shows the tracking of the ramp trajectory (trajectory 2). The tracking error is within ±0.3 mm. Figure 4.3.8 and Figure 4.3.9 show 1 Hz sine wave (trajectory 3) and 2 Hz sine wave (trajectory 4) tracking. For both sine wave trajectories, the maximum tracking error is within ±0.5 mm expect the initial period. Note that the 2 Hz sine wave has smaller amplitude so the percentage error is larger. The initial rise of the 2 Hz sine wave tracking (trajectory 4) has a large oscillation. This was caused by the cycloidal profile for the rising portion containing 4 Hz components and the resulting valve saturation.

The tracking performance worsens as the trajectory frequency becomes higher since the faster tracking requires bigger mass flow rate for the two chambers and the valves get saturated. Figure 4.3.10 shows the control signals for the four valves from the experiment with trajectory 4. It is clear that the three valves of the four, all except valve 3, are saturated during the initial period. In chapter 3 it was shown that the valve 3 has bigger

mass flow rate than the other three valves. Thus, the bandwidth of the system is mainly limited by the mass flow rate of the valves.

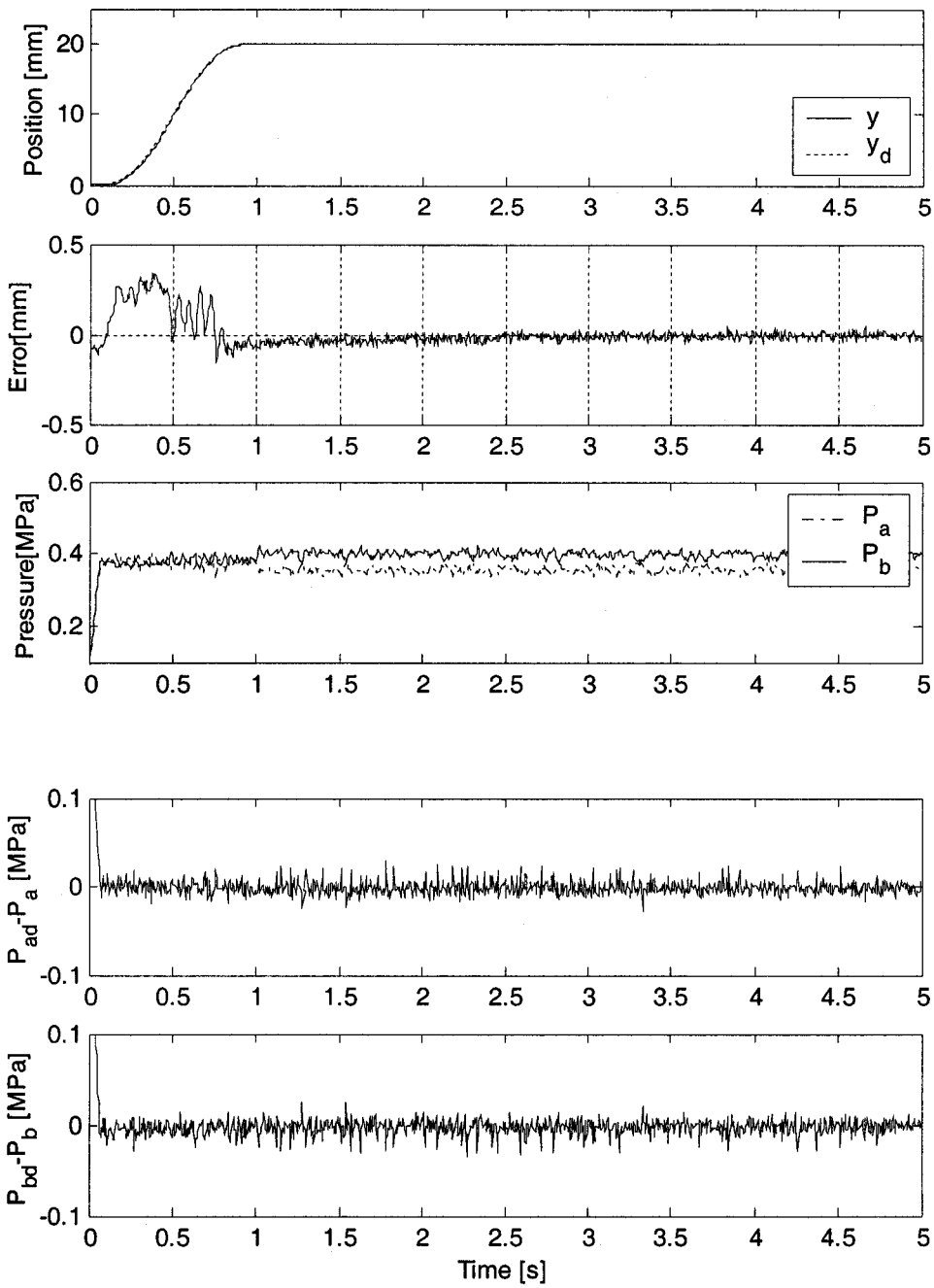

Figure 4.3.6: Trajectory 1 experiment with the inverse dynamics controller.

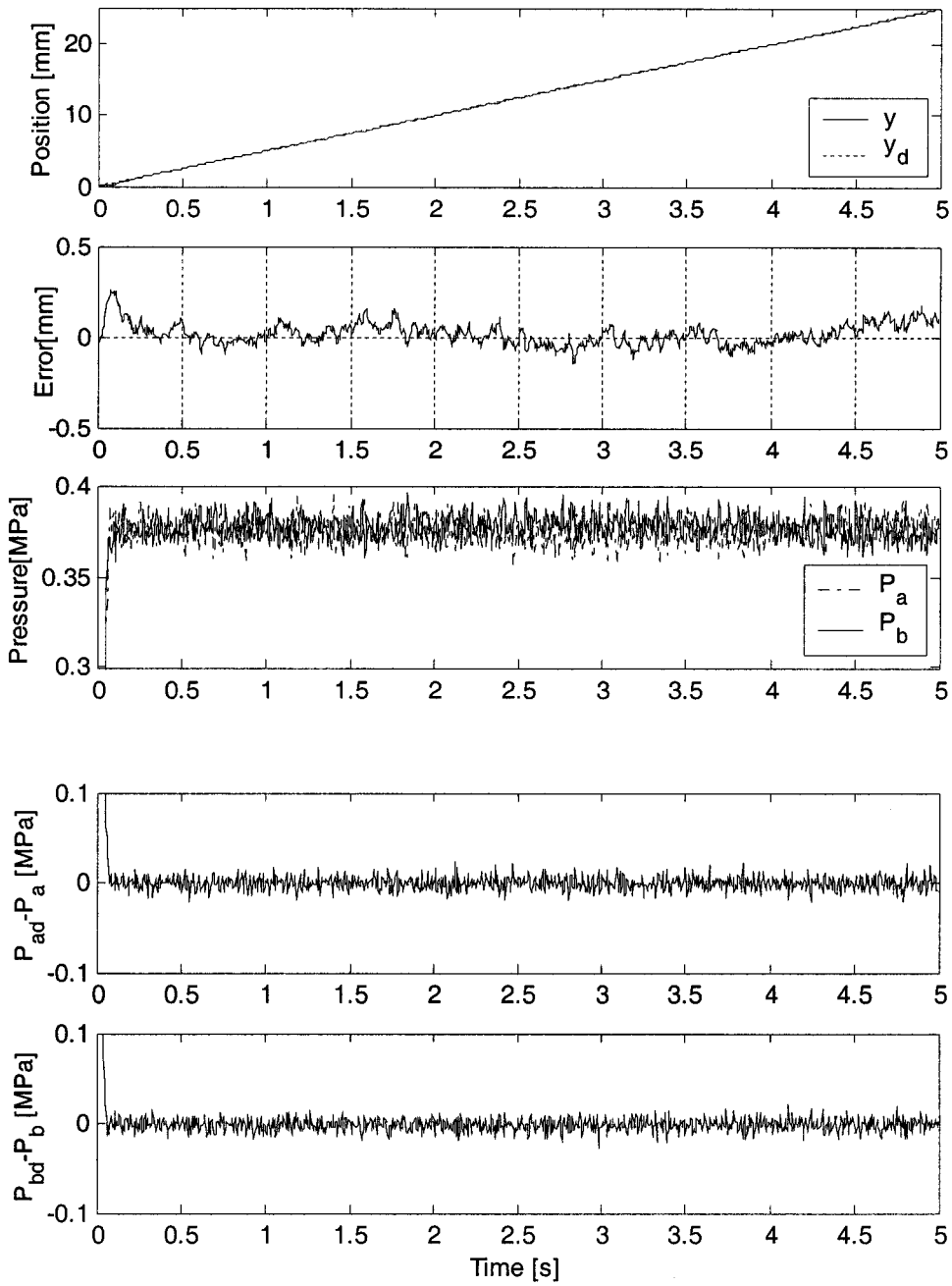

Figure 4.3.7: Trajectory 2 experiment with the inverse dynamics controller.

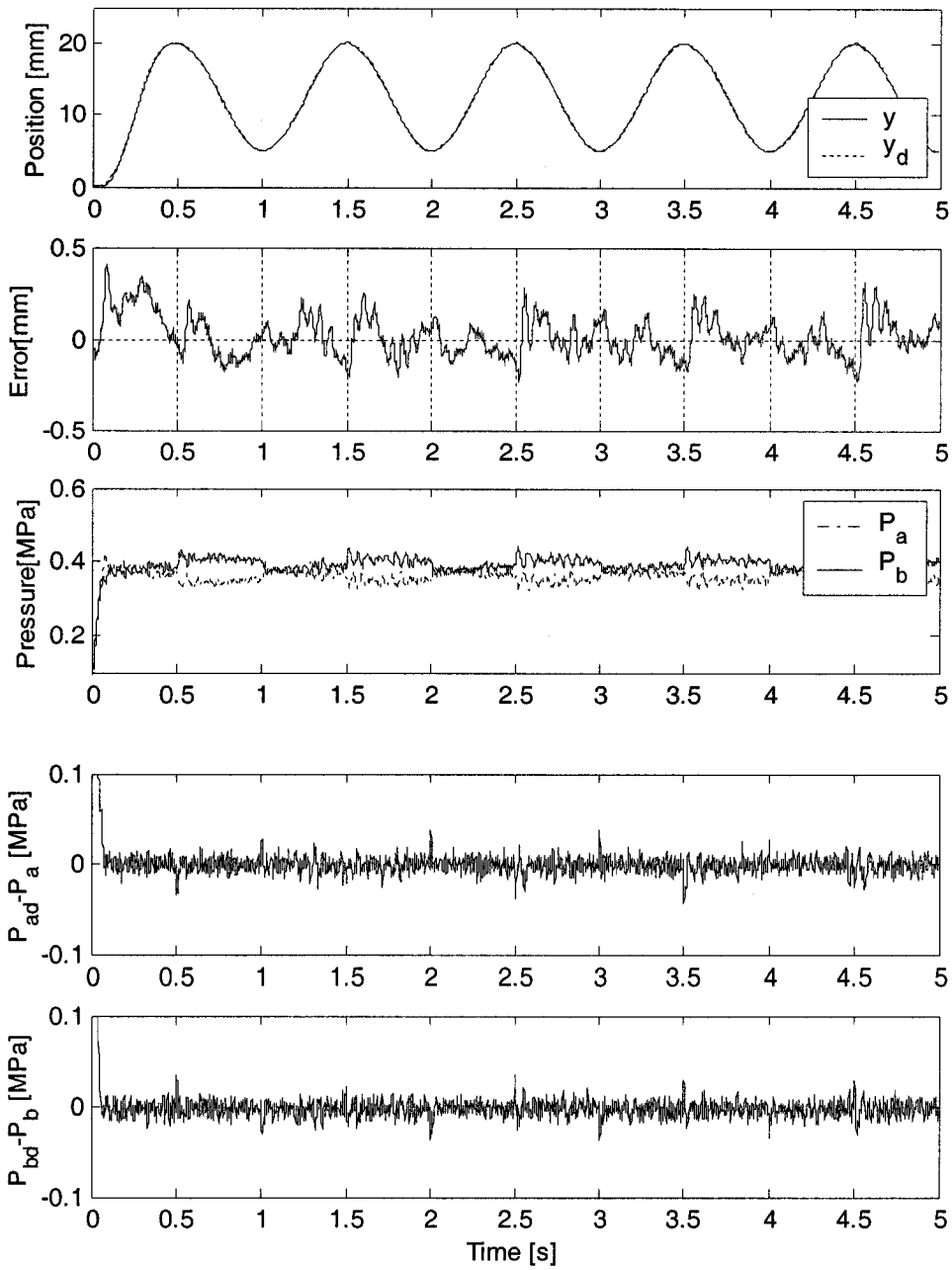

Figure 4.3.8: Trajectory 3 experiment with the inverse dynamics controller.

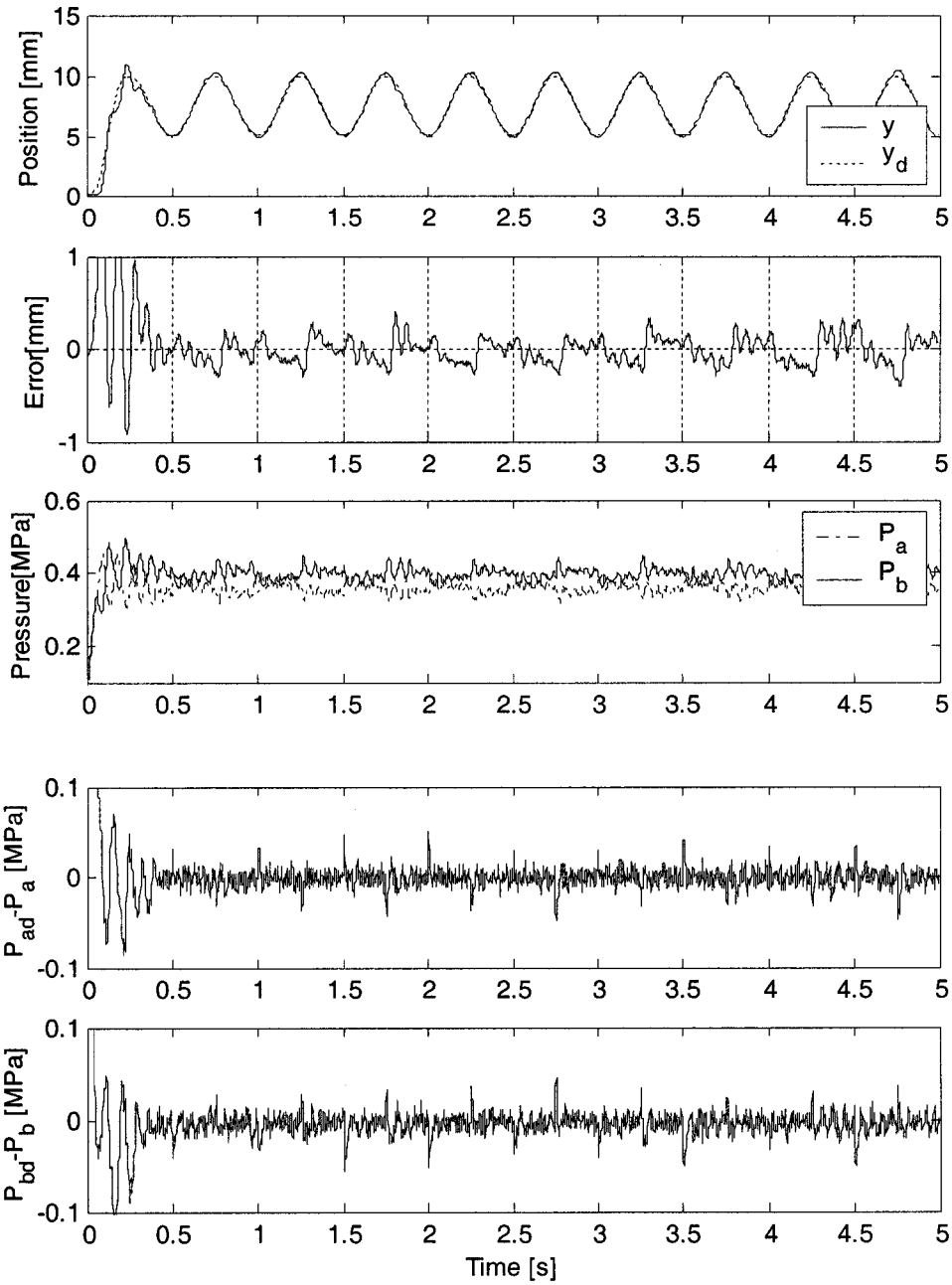

Figure 4.3.9: Trajectory 4 experiment with the inverse dynamics controller.

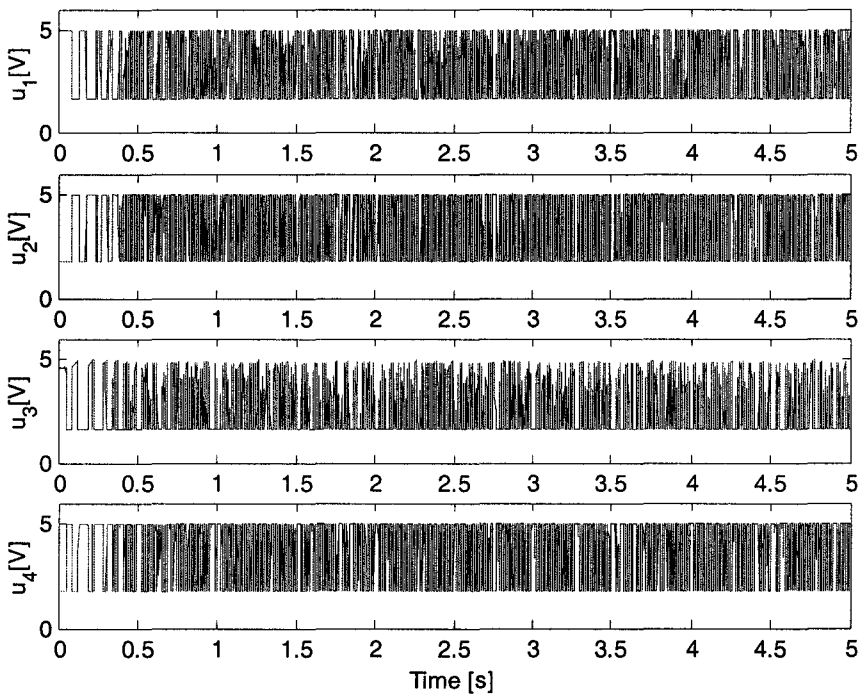

Figure 4.3.10: Valve voltage signals from the trajectory 4 experiment.

4.4 Controller design using the backstepping method

The system is nonlinear and we wish to control the payload position using multiple valves so this is a multiple-input single-output (MISO) nonlinear controller design problem. Backstepping is a recursive design procedure suitable for a class of nonlinear systems called "strict feedback systems" [36].

4.4.1 Design procedure

The set of state variables is defined as follows: $x_1 = y$ is the piston position; $x_2 = \dot{y}$ is the piston velocity; $x_3 = P_a$ and $x_4 = P_b$ are chamber pressures; and $x_5 = \dot{m}_a$ and $x_6 = \dot{m}_b$ are chamber flow rates. The system model may then be written in the form

$$\dot{x}_1 = x_2 \tag{4.4.1}$$

$$\dot{x}_2 = \frac{1}{M}\left(x_3 A_a - x_4 A_b - F_f - F_l - P_0 A_{rod}\right) \tag{4.4.2}$$

$$\dot{x}_3 = -\frac{KA_a}{A_a x_1 + V_{a0}} x_2 x_3 + \frac{KRT}{A_a x_1 + V_{a0}} x_5 \tag{4.4.3}$$

$$\dot{x}_4 = \frac{KA_b}{A_b (L - x_1) + V_{b0}} x_2 x_4 + \frac{KRT}{A_b (L - x_1) + V_{b0}} x_6 \tag{4.4.4}$$

If we treat x_5 and x_6 as control signals, this is a MISO strict-feedback system, which is suitable for the recursive backstepping design procedure. The two mass flow rates will be transferred to the valve control voltages according to the flow rate distribute strategy and back-solving of the valve models, as described in step 4 in section 4.3.1.

We start the backstepping procedure by defining the tracking error as

$$z_1 = x_{1d} - x_1 \tag{4.4.5}$$

where x_{1d} is the desired payload position. The derivative of the tracking error, taking into account (4.4.1), is

$$\dot{z}_1 = \dot{x}_{1d} - x_2 \tag{4.4.6}$$

where $\dot{x}_{1d}$ is the desired payload velocity. Choosing $V_1 = \frac{1}{2}\gamma_1 z_1^2$, where $\gamma_1 = 1[\mathrm{kg \cdot s^{-2}}]$, as a Lyapunov function candidate for (4.4.1), a stabilizing function is selected as

$$\alpha_1 = k_1 z_1 + \dot{x}_{1d} \tag{4.4.7}$$

and the control error is

$$z_2 = \alpha_1 - x_2 \tag{4.4.8}$$

The derivative of V_1 is derived as,

$$\dot{V}_1 = -k_1\gamma_1 z_1^{\,2} + \gamma_1 z_1 z_2 \tag{4.4.9}$$

This would be negative definite if z_2 were zero. Since V_1 is positive definite and $V_1 \to \infty$ as $\|z_1\| \to \infty$, according to the Lyapunov theorem of global stability [27, p.64], z_1 is globally asymptotically stable at the origin, or $z_1 \to 0$ as $t \to \infty$. We now choose another Lyapunov function $V_2 = V_1 + \frac{1}{2}\gamma_2 z_2^{\,2}$, where $\gamma_2 = 1[\text{kg}]$. Using (4.4.8), (4.4.7) and (4.4.2), the derivative of z_2 is:

$$\begin{aligned} \dot{z}_2 &= \dot{\alpha}_1 - \dot{x}_2 \\ &= \left(k_1\dot{z}_1 + \ddot{x}_{1d}\right) - \frac{1}{M}\left(x_3 A_a - x_4 A_b - F_f - F_l - P_0 A_{rod}\right) \end{aligned} \tag{4.4.10}$$

The derivative of V_2 is,

$$\begin{aligned} \dot{V}_2 &= \dot{V}_1 + \gamma_2 z_2 \dot{z}_2 \\ &= \gamma_1\left(-k_1 z_1^{\,2} + z_1 z_2\right) + \gamma_2 z_2\left(k_1\dot{z}_1 + \ddot{x}_{1d}\right) - \frac{\gamma_2 z_2}{M}\left(x_3 A_a - x_4 A_b - F_f - F_l - P_0 A_{rod}\right) \end{aligned} \tag{4.4.11}$$

This inspires us to choose the virtual driven force,

$$\alpha_2 A_a - \alpha_3 A_b = M\beta + \hat{F}_f + F_l + P_0 A_{rod} \tag{4.4.12}$$

where

$$\beta = \ddot{x}_{1d} + k_1\dot{z}_1 + \frac{\gamma_1}{\gamma_2} z_1 + k_2 z_2\,; \tag{4.4.13}$$

$\hat{F}_f$ is the friction estimate given by (4.3.19); α_2 and α_3 are virtual chamber pressures for chamber A and B, respectively. Define two pressure tracking errors,

$$z_3 = \alpha_2 - x_3 \tag{4.4.14}$$

and

$$z_4 = \alpha_3 - x_4 \tag{4.4.15}$$

Substituting (4.4.12)~(4.4.15) into (4.4.11) yields

$$\dot{V}_2 = -\gamma_1 k_1 z_1^2 - \gamma_2 k_2 z_2^2 + \frac{\gamma_2 z_2}{M}\left(F_f - \hat{F}_f\right) + \frac{\gamma_2 z_2}{M}\left(z_3 A_a - z_4 A_b\right) \tag{4.4.16}$$

If z_3 and z_4 were zero, $\dot{V}_2$ is semi-negative definite for all (z_1, z_2) by selecting k_1 and k_2 big enough, provided that the friction modeling error is bounded,

$$\left|F_f - \hat{F}_f\right| \le \Delta_1 \tag{4.4.17}$$

According to the global invariant set theorem [27, p.73], the (z_1, z_2) system would be globally asymptotically uniformly bounded.

Equation (4.4.12) may be independently satisfied by α_2 and α_3. The same approach as in section 4.3.1 is used to dispatch the two desired pressures,

$$P_s - \alpha_2 = \alpha_3 - P_0 \tag{4.4.18}$$

From (4.4.12) and (4.4.18) one can solve for the two desired pressures,

$$\alpha_2 = \frac{A_b\left(P_s + P_0\right) + M\beta + \hat{F}_f + F_l + P_0 A_{rod}}{A_a + A_b} \tag{4.4.19}$$

$$\alpha_3 = \frac{A_a\left(P_s + P_0\right) - M\beta - \hat{F}_f - F_l - P_0 A_{rod}}{A_a + A_b} \tag{4.4.20}$$

Now the goal is to stabilize the (z_1, z_2, z_3, z_4) system. Define a Lyapunov function as,

$$V_3 = V_2 + \frac{1}{2}\gamma_3 z_3^2 + \frac{1}{2}\gamma_3 z_4^2 \tag{4.4.21}$$

where $\gamma_3 = 1[\mathrm{m}^2 \cdot \mathrm{kg}^{-1} \cdot \mathrm{s}^{-2}]$. Using (4.4.14), (4.4.19) and (4.4.3),

$$\begin{aligned} \dot{z}_3 &= \dot{\alpha}_2 - \dot{x}_3 \\ &= \frac{M\dot{\beta} + \dot{\hat{F}}_f}{A_a + A_b} + \frac{KA_a}{A_a x_1 + V_{a0}} x_2 x_3 - \frac{KRT}{A_a x_1 + V_{a0}} x_5 \end{aligned} \tag{4.4.22}$$

Using (4.4.15), (4.4.20) and (4.4.4),

$$\begin{aligned} \dot{z}_4 &= \dot{\alpha}_3 - \dot{x}_4 \\ &= -\frac{M\dot{\beta} + \dot{\hat{F}}_f}{A_a + A_b} - \frac{KA_b}{A_b(L - x_1) + V_{b0}} x_2 x_4 - \frac{KRT}{A_b(L - x_1) + V_{b0}} x_6 \end{aligned} \tag{4.4.23}$$

The derivative of V_3 is,

$$\begin{aligned} \dot{V}_3 &= \dot{V}_2 + \gamma_3 z_3 \dot{z}_3 + \gamma_3 z_4 \dot{z}_4 \\ &= -\gamma_1 k_1 z_1^{\,2} - \gamma_2 k_2 z_2^{\,2} + \frac{\gamma_2 z_2}{M}\left(F_f - \hat{F}_f\right) + \frac{\gamma_2 z_2}{M}\left(z_3 A_a - z_4 A_b\right) \\ &+ \gamma_3 z_3 \left(\frac{M\dot{\beta} + \dot{\hat{F}}_f}{A_a + A_b} + \frac{KA_a}{A_a x_1 + V_{a0}} x_2 x_3 - \frac{KRT}{A_a x_1 + V_{a0}} x_5 \right) \\ &+ \gamma_3 z_4 \left(-\frac{M\dot{\beta} + \dot{\hat{F}}_f}{A_a + A_b} - \frac{KA_b}{A_b(L - x_1) + V_{b0}} x_2 x_4 - \frac{KRT}{A_b(L - x_1) + V_{b0}} x_6 \right) \end{aligned} \tag{4.4.24}$$

This inspired us the following virtual mass flow rates for chambers A and B:

$$\alpha_4 = \frac{A_a x_1 + V_{a0}}{KRT}\left(k_3 z_3 + \frac{\gamma_2 z_2 A_a}{\gamma_3 M} + \frac{M\dot{\beta} + \dot{\hat{F}}_f}{A_a + A_b} \right) + \frac{A_a}{RT} x_2 x_3 \tag{4.4.25}$$

$$\alpha_5 = \frac{A_b(L - x_1) + V_{b0}}{KRT}\left(k_4 z_4 - \frac{\gamma_2 z_2 A_b}{\gamma_3 M} - \frac{M\dot{\beta} + \dot{\hat{F}}_f}{A_a + A_b} \right) - \frac{A_b}{RT} x_2 x_4 \tag{4.4.26}$$

Define two flow rate modeling errors as

$$z_5 = \alpha_4 - x_5 \tag{4.4.27}$$

$$z_6 = \alpha_5 - x_6 \tag{4.4.28}$$

Substituting (4.4.25)~(4.4.28) into (4.4.24) we obtain,

$$\begin{aligned}\dot{V}_3 &= -\gamma_1 k_1 z_1^{\,2} - \gamma_2 k_2 z_2^{\,2} - \gamma_3 k_3 z_3^{\,2} - \gamma_3 k_4 z_4^{\,2} \\ &+ \frac{\gamma_2 z_2}{M}\left(F_f - \hat{F}_f\right) + \frac{KRT}{A_a x_1 + V_{a0}}\gamma_3 z_3 z_5 + \frac{KRT}{A_b (L - x_1) + V_{b0}}\gamma_3 z_4 z_6\end{aligned} \tag{4.4.29}$$

Assuming the valve modeling errors are bounded, $|z_5| < \Delta_2$ and $|z_6| < \Delta_2$, and knowing the displacement x_1 is bounded by the stroke length L, (4.4.29) is bounded by

$$\dot{V}_3 \le -\gamma_1 k_1 z_1^{\,2} - \gamma_2 k_2 z_2^{\,2} - \gamma_3 k_3 z_3^{\,2} - \gamma_3 k_4 z_4^{\,2} + \frac{\gamma_2 z_2}{M}\Delta_1 + \Psi\gamma_3 z_3 \Delta_2 + \Psi\gamma_3 z_4 \Delta_2 \tag{4.4.30}$$

where Ψ is the upper-boundary of the two $\frac{KRT}{\cdots}$ terms in (4.4.29). $\dot{V}_3$ can be made semi-negative definite for all (z_1, z_2, z_3, z_4) by selecting k_1, k_2, k_3 and k_4 big enough. Using the global invariant set theorem [27, p.73], the (z_1, z_2, z_3, z_4) system is globally asymptotically uniformly bounded and tracking error z_1 can be made arbitrarily small by selecting sufficiently large k_1, k_2, k_3 and k_4.

The two desired chamber flow rates have been derived in (4.4.25) and (4.4.26). Finally the valve input voltages are obtained as described in step (iv) in section 4.3.1.

4.4.2 Simulation results

The designed controller was simulated with the four trajectories from Table 4.3.1 as before. The controller gains were tuned using the same procedure as the inverse dynamics controller and the values are as follow: $k_1 = 60[s^{-1}]$, $k_2 = 70[s^{-1}]$, $k_3 = 500[s^{-1}]$ and $k_4 = 500[s^{-1}]$. The simulation results are shown in Figures 4.4.1 to 4.4.4. In each

simulation the position tracking error and the chamber pressures are shown. From the figures, the backstepping controller provides similar performance to the inverse dynamics controller. The RMSE values of the two controllers are compared in Table 4.4.1. It is found that the RMSE value of the backstepping controller is slightly bigger than that of the inverse dynamics controller for all the four trajectories. This is because that the tuned gains of the backstepping controller are lower than that of the inverse dynamics controller. The reason will be further discussed in section 5.4.

Table 4.4.1: RMSE values [mm] from the simulations with the nonlinear controllers.

Trajectory	Inverse dynamics controller	Backstepping controller
1	0.0074	0.0079
2	0.0242	0.0244
3	0.0324	0.0343
4	0.0640	0.0664

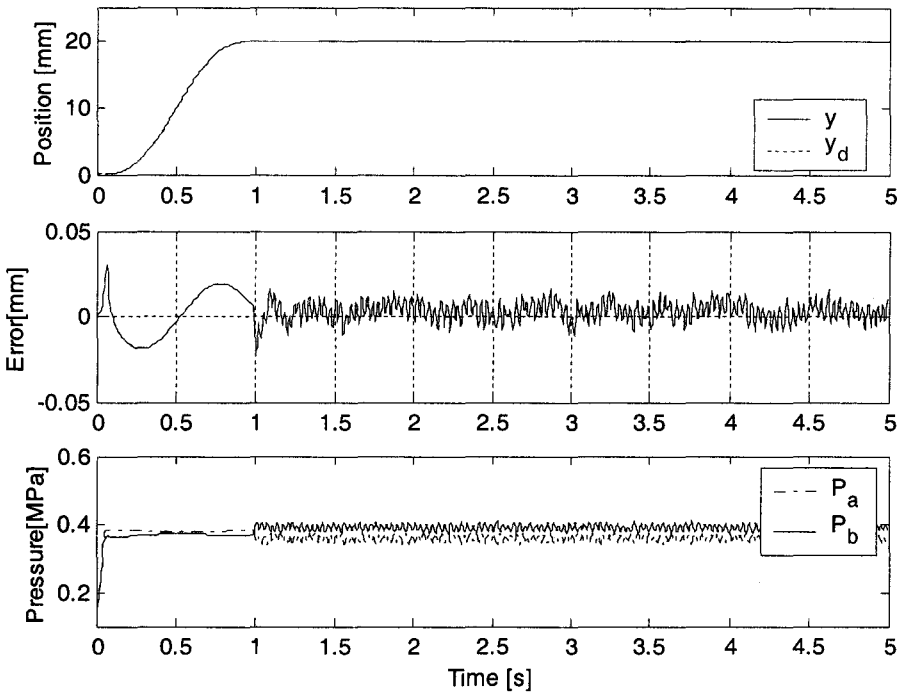

Figure 4.4.1: Trajectory 1 simulation with the backstepping controller.

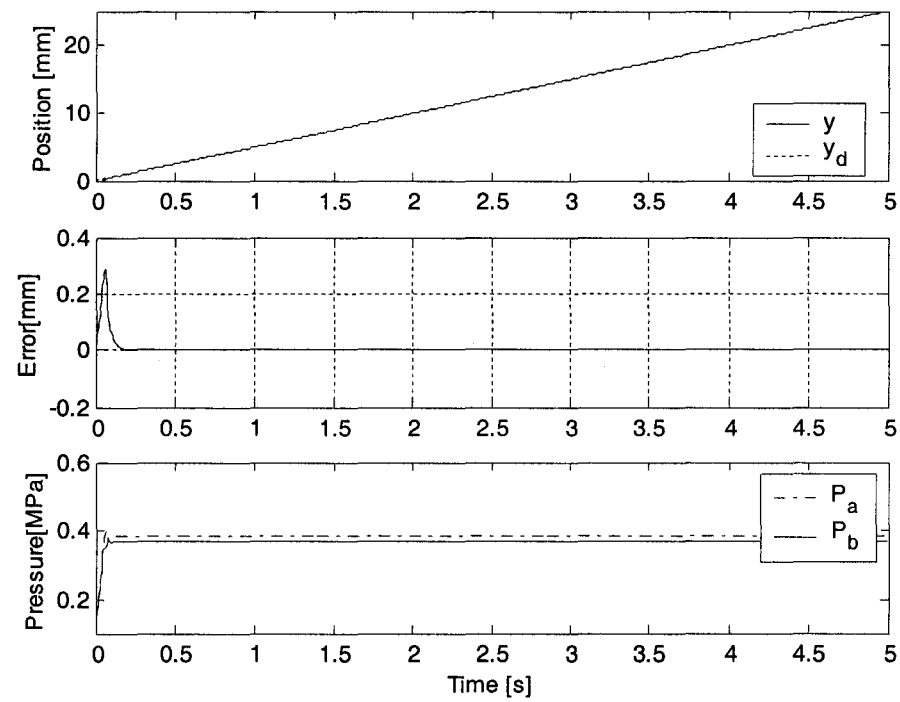

Figure 4.4.2: Trajectory 2 simulation with the backstepping controller.

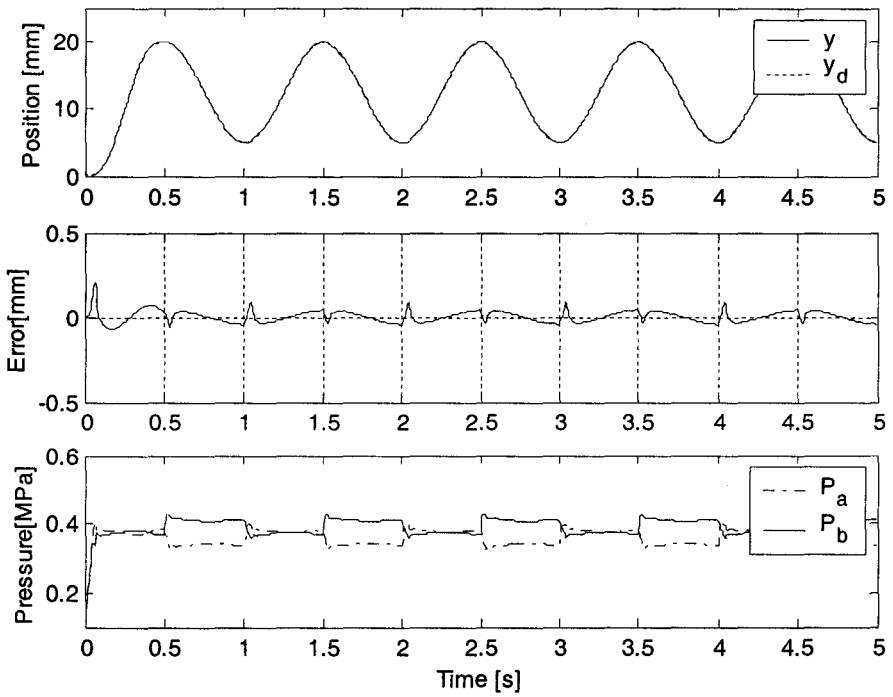

Figure 4.4.3: Trajectory 3 simulation with the backstepping controller.

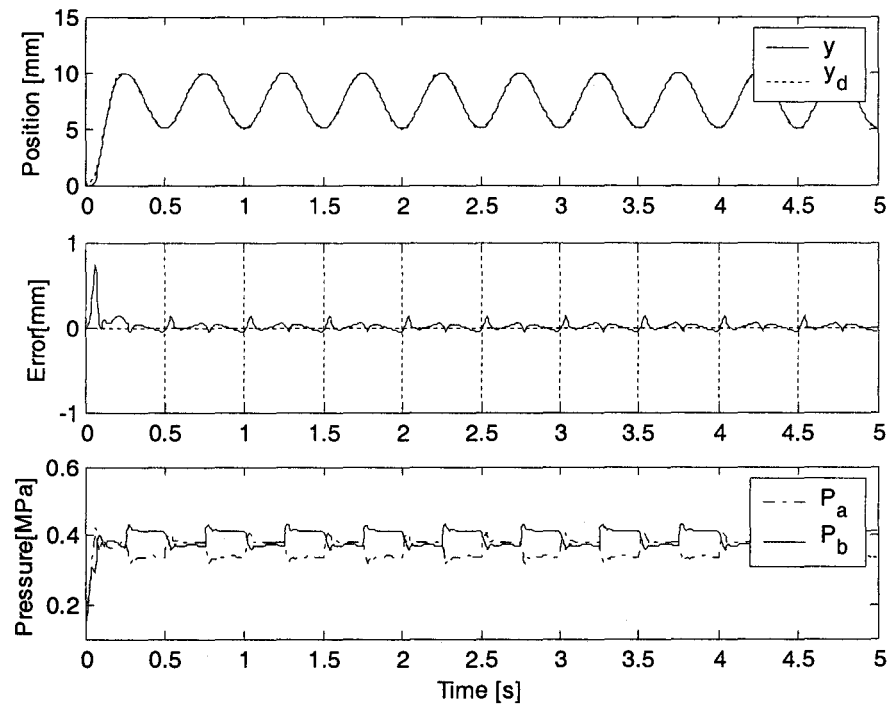

Figure 4.4.4: Trajectory 4 simulation with the backstepping controller.

4.4.3 Experiment results

The backstepping controller was tested with the system. The four reference trajectories listed in Table 4.3.1 were tested. The tuning process was begun by setting all four control gains to low values. Gains k_3 and k_4 were then increased until the pressure tracking errors z_3 and z_4 were minimized over a series of sine wave reference inputs. Next, gains k_1 and k_2 were increased until the position error z_1 and the velocity error z_2 were minimized. The tuned values of the gains were: $k_1 = 60[s^{-1}]$, $k_2 = 45[s^{-1}]$, $k_3 = 400[s^{-1}]$ and $k_4 = 400[s^{-1}]$. The experiment results are shown in Figures 4.4.5 to 4.4.8.

The steady state error for trajectory 1 is in the range of ±0.05 mm. The tracking error for trajectory 2 is in the range of ±0.2 mm. For the 1 Hz and 2 Hz sine waves tracking, the tracking error is in the range of ±0.3 mm, except during the initial rise.

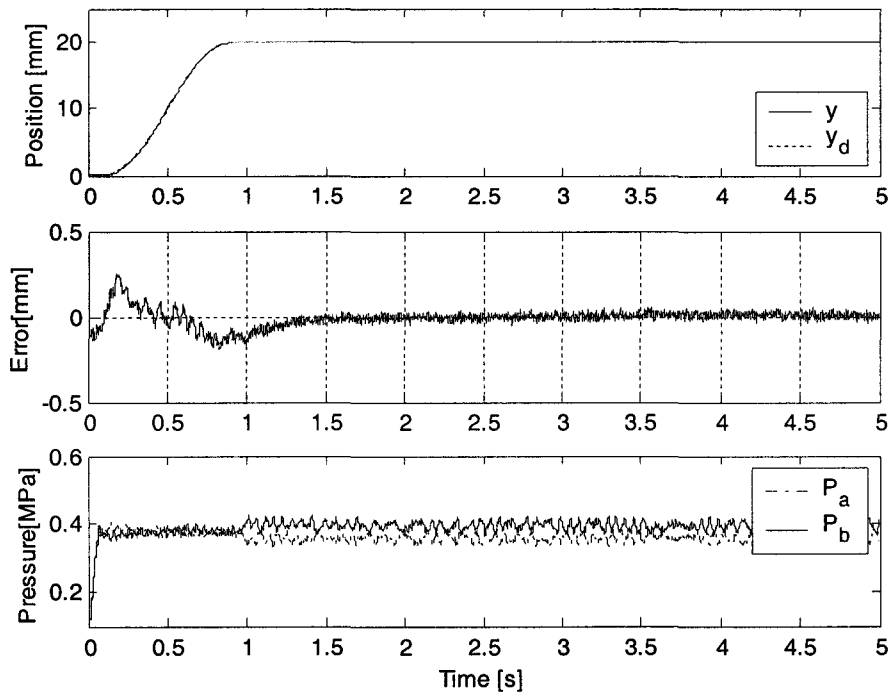

Figure 4.4.5: Trajectory 1 experiment with the backstepping controller.

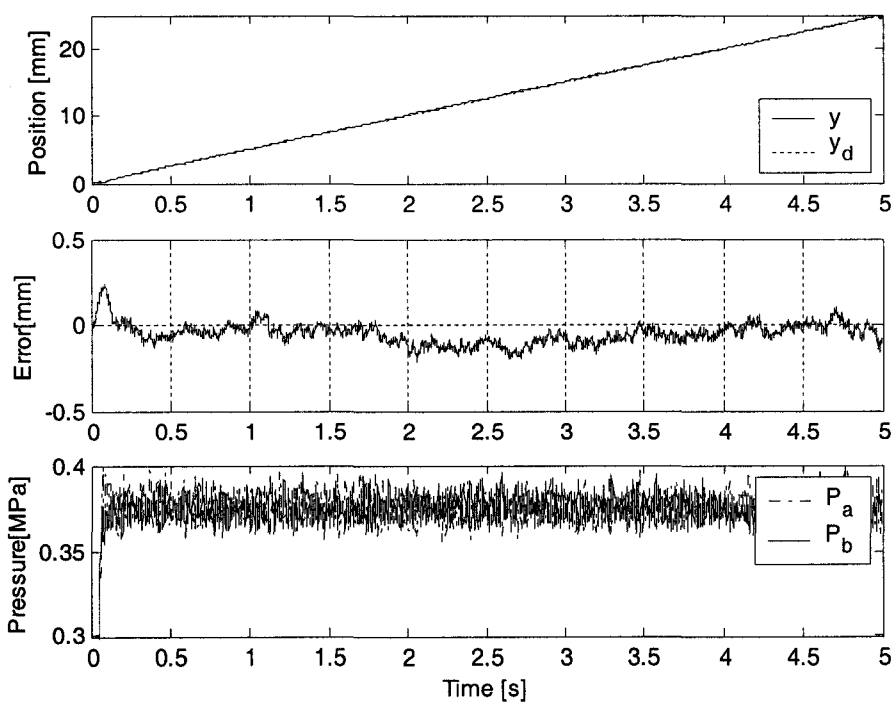

Figure 4.4.6: Trajectory 2 experiment with the backstepping controller.

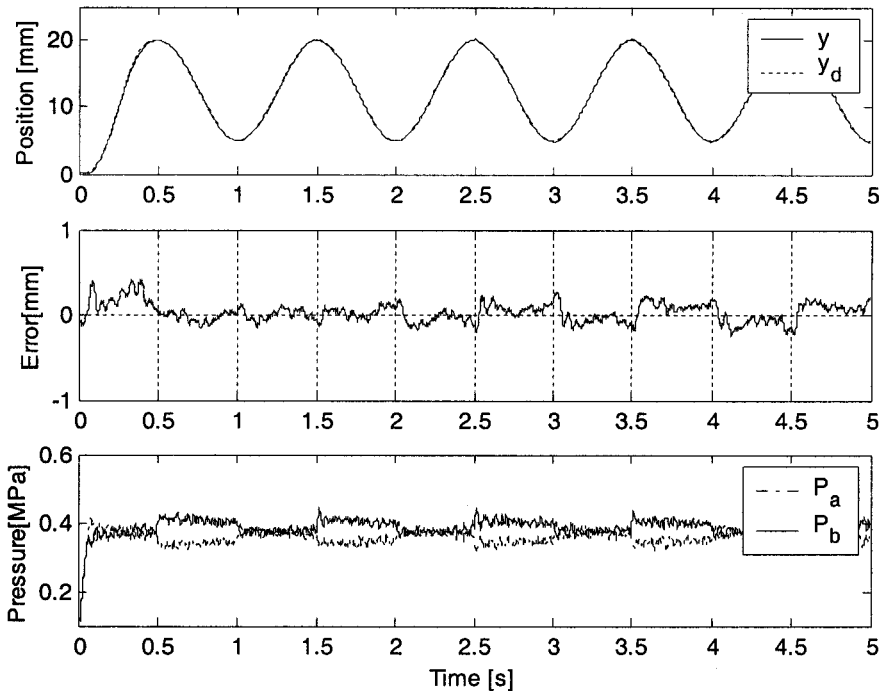

Figure 4.4.7: Trajectory 3 experiment with the backstepping controller.

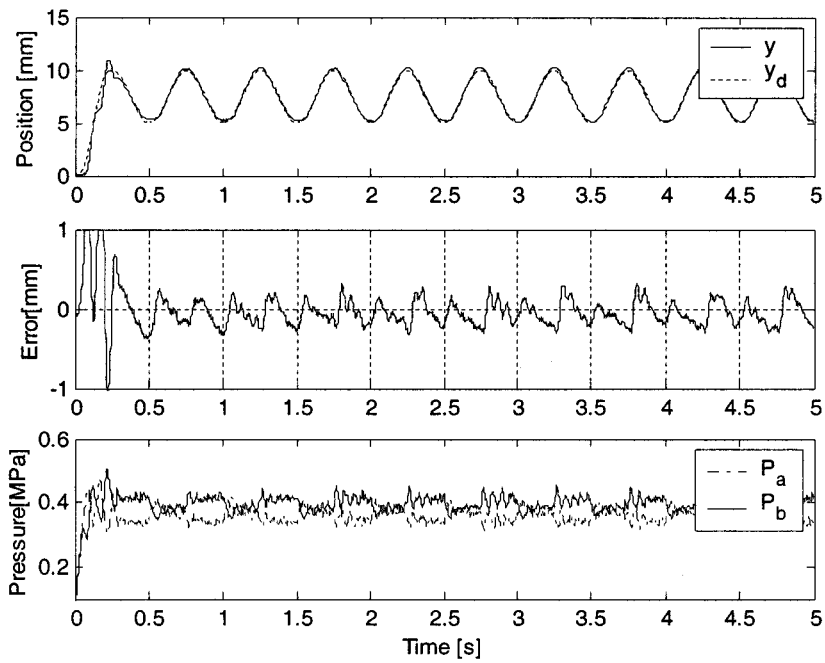

Figure 4.4.8: Trajectory 4 experiment with the backstepping controller.

4.5 Comparison of the controllers

Each experiment has been repeated five times for both controllers. The SSE of the step response listed in Table 4.5.1. It shows that the two controllers can achieve a SSE of ±0.08 mm and ±0.05 mm respectively. The RMSE values of the two controllers are recorded in Table 4.5.2. From the mean value of the RMSE and the standard deviation it is concluded that the control performances of the two controllers are very close and quite repeatable.

Table 4.5.1: SSE values [mm] from the experiments with the nonlinear controllers.

Controller	Test 1	Test 2	Test 3	Test 4	Test 5	Range
Inverse dynamics	±0.06	±0.05	±0.06	±0.07	±0.08	±0.08
Backstepping	±0.04	±0.04	±0.05	±0.04	±0.05	±0.05

Table 4.5.2: RMSE values [mm] from the experiments with the nonlinear controllers.

	Test 1	Test 2	Test 3	Test 4	Test 5	Mean	Std. Dev
Inverse dynamics controller							
Trajectory 1	0.0772	0.0400	0.0568	0.0646	0.0667	0.0611	0.0138
Trajectory 2	0.0619	0.0709	0.0685	0.0852	0.0716	0.0716	0.0085
Trajectory 3	0.1086	0.1157	0.1260	0.1357	0.1343	0.1241	0.0118
Trajectory 4	0.2557	0.2423	0.2164	0.2149	0.2122	0.2283	0.0195
Backstepping controller							
Trajectory 1	0.0515	0.1184	0.0652	0.0646	0.0688	0.0737	0.0258
Trajectory 2	0.0805	0.0847	0.1145	0.1300	0.0759	0.0971	0.0238
Trajectory 3	0.1134	0.1268	0.1427	0.1589	0.1377	0.1359	0.0171
Trajectory 4	0.2598	0.2399	0.2553	0.2389	0.2612	0.2510	0.0108

The RMSE values for the two nonlinear controllers are compared with the PVA+FF+DZC controller in Table 4.5.3. Both nonlinear controllers clearly outperform the PVA design for all three types of reference trajectory. The average reduction of the RMSE was 85%. An example comparison of the tracking errors for the three controllers in a trajectory 1 test is in Figure 4.5.1.

Table 4.5.3: Comparison of the experimental RMSE values [mm].

	PVA+FF+DZC	Inverse dynamics	Backstepping
Trajectory 1	0.3091	0.0611	0.0737
Trajectory 2	0.6744	0.0716	0.0971
Trajectory 3	0.9226	0.1241	0.1359

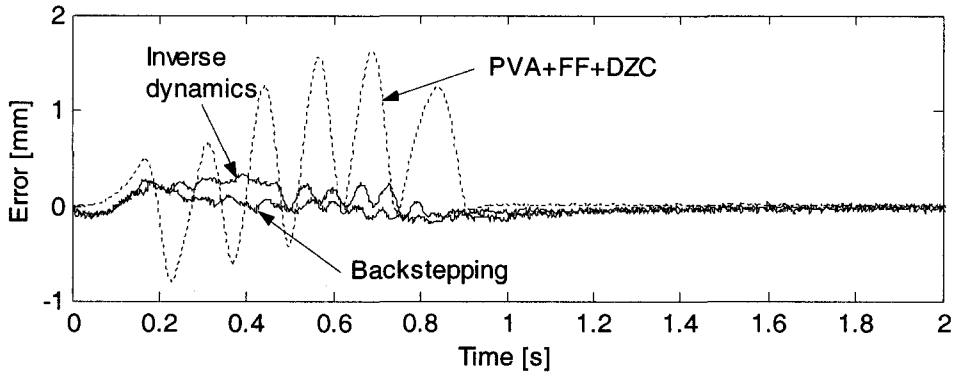

Figure 4.5.1: Comparison of the experimental tracking errors for trajectory 1.

4.6 Conclusions

Three controllers for the pneumatic servo system were designed and tested. First a linear PVA controller was implemented for comparison purposes. Next, an inverse dynamics controller and a backstepping controller were designed based on the nonlinear system model. Experimental results showed that the inverse dynamics controller achieved a SSE of ±0.08 mm for a 20 mm step signal with a cycloidal rising edge and the backstepping controller achieved a SSE of ±0.05 mm. For the tracking performance with the ramp, 1 Hz sine wave and 2 Hz sine wave trajectories, the inverse dynamics controller achieved a tracking error of ±0.5 mm and the backstepping controller achieved a tracking error of ±0.3 mm. The two nonlinear controllers outperformed the linear PVA controller. The average RMSE of the three trajectories was reduced by 85%. The performance of the controllers worsens when the trajectory frequency becomes higher because the valves become saturated.

CHAPTER 5

ROBUSTNESS AND GENERALITY TESTS

5.1 Introduction

Robustness is the capability of a controller to be insensitive to plant modeling errors and to reject disturbances. Since the system cannot be accurately modeled in practice, robustness is important. Due to the inaccuracy in the plant modeling, the controller designed based on the nominal plant should work with the plant with parameter variations to some extent. Generality is the capability of a control design procedure to be applied to systems with different dynamics. This chapter will present test results for the robustness and generality of the two controllers designed in the previous chapter.

5.2 Robustness experiments

In this section we examine the robustness of the two controllers with the test system used in the previous chapter. First we test the robustness to different moving masses, then we test the system in vertical orientation.

5.2.1 Moving payload variation

The two controllers were tuned with the nominal moving mass M =1.532kg. With the controller gains fixed, tests were performed with M=2.326kg and M=1.106kg. Trajectory 1 and trajectory 3 (see table 4.3.1) were tested. Each test was performed five times. In the experiments, both controllers became unstable with the decreased payload. Only the experimental data for the increased payload are documented here. The RMSE

values for trajectory 1 and trajectory 3 are listed in table 5.2.1. The RMSE values for different payloads are compared in table 5.2.2.

Table 5.2.1: RMSE values [mm] with the controllers with increased payload.

	Test 1	**Test 2**	**Test 3**	**Test 4**	**Test 5**	**Mean**	**Std. Dev.**
Inverse dynamics controller							
Trajectory 1	0.0756	0.0536	0.0430	0.0768	0.0484	0.0595	0.0157
Trajectory 3	0.2000	0.1422	0.1368	0.1865	0.1405	0.1612	0.0297
Backstepping controller							
Trajectory 1	0.0798	0.0847	0.0825	0.0402	0.0406	0.0656	0.0231
Trajectory 3	0.1464	0.1541	0.1542	0.1614	0.1586	0.1549	0.0057

Table 5.2.2: Comparison of RMSE [mm] with the controllers with different payload.

***M*(kg)**	**Trajectory**	**Inverse dynamics controller**	**Backstepping controller**
1.532 (nominal)	1	0.0611	0.0737
	3	0.1241	0.1359
2.326	1	0.0595	0.0656
	3	0.1612	0.1549
1.106	1	Unstable	Unstable
	3	Unstable	Unstable

The results (see Table 5.2.2) show that with a 52% increase in M, the RMSE values of the inverse dynamics controller increased by 19% on average, that of the backstepping controller increased by only 5%, while for a decrease in M of 39% both controllers became unstable. These results demonstrate that the two controllers are robust with increased payload but not for decreased payload.

In both the inverse dynamics controller and the backstepping controller, the position feedback loop has a second order closed-loop transfer function. For example, the closed-loop transfer function for the inverse dynamics controller can be obtained by substituting (4.3.12) into (4.3.16) to get,

$$\frac{e}{F_{fe}+F_{pe}}=\frac{1/M}{s^2+(\lambda+K_s/M)s+\lambda K_s/M} \tag{5.2.1}$$

which has the natural frequency of $\sqrt{\lambda K_s/M}$. Decrease of mass and increase of the two position controller gains have the effect of increase the bandwidth. In the experiments the high frequency noise may have excited unmodeled high frequency modes in the system and caused the system to be unstable.

5.2.2 Vertical motion experiments

The two controllers were tested in the vertical direction with the nominal moving mass. In vertical direction, the load force $F_l = Mg$. The tests were applied the same as in the previous section. The RMSE values are recorded in Table 5.2.3 and compared in Table 5.2.4.

Table 5.2.3: RMSE values [mm] with the controllers in vertical direction.

	Test 1	**Test 2**	**Test 3**	**Test 4**	**Test 5**	**Mean**	**Std. Dev.**
Inverse dynamics controller							
Trajectory 1	0.1425	0.1478	0.1971	0.1714	0.1595	0.1636	0.0218
Trajectory 3	0.3472	0.2256	0.3882	0.2477	0.2767	0.2971	0.0685
Backstepping controller							
Trajectory 1	0.0939	0.0972	0.0924	0.0954	0.1062	0.0970	0.0055
Trajectory 3	0.4926	0.3940	0.4768	0.2144	0.1957	0.3547	0.1418

Table 5.2.4: Comparison of RMSE [mm] with the controllers in vertical direction.

Orientation	**Trajectory**	**Inverse dynamics**	**Backstepping**
Horizontal	1	0.0611	0.0737
	3	0.1241	0.1359
Vertical	1	0.1636	0.0970
	3	0.2971	0.3547

From Table 5.2.4 it is found that the performance of both controllers decays in vertical orientation compared with the horizontal orientation. The average RMSE value increased by 149% for the inverse dynamics controller and 116% for the backstepping controller. The reasons for the performance decay in vertical orientation are as follows.

In the vertical orientation, the chamber pressure difference is bigger than that in horizontal orientation, the extra portion is necessary to compensate for the gravity force. An example of test using the backstepping controller is shown in Figure 5.2.1. It is found that the tracking error in vertical orientation was much more bigger for the first 0.5 seconds, during which the trajectory is the cycloidal profile that contains a 2 Hz component. The tracking errors of both orientations are very similar after the first 0.5 seconds. In the first 0.5 seconds a bigger flow rate is needed for chamber A to move the payload vertically upwards such that valve 1 and valve 4 became saturated, causing a pressure oscillation, and thus a bigger tracking error.

In addition, in the vertical orientation, the friction changes so the model-based friction compensation may cause more error. Also, the payload gravity is compensated by the F_l term in the controller. The inaccuracy of the moving mass measurement causes additional error.

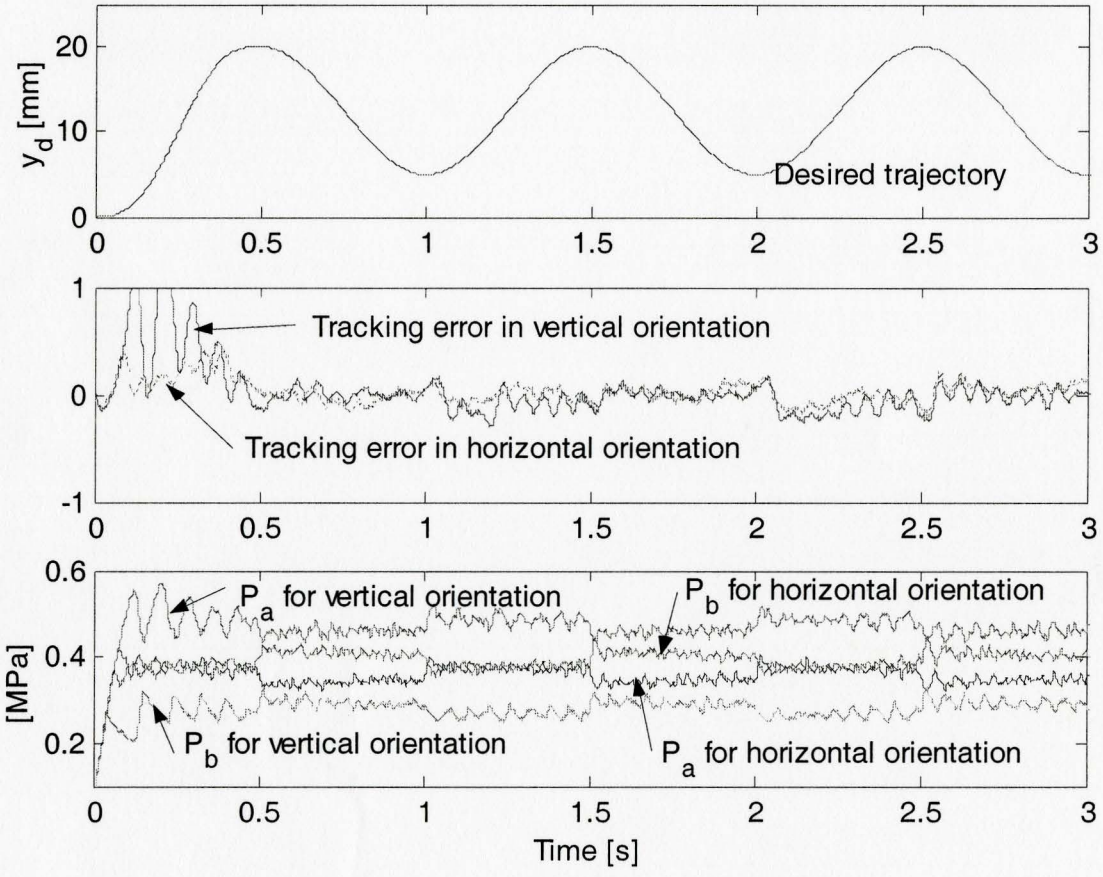

Figure 5.2.1 Comparison of vertical and horizontal motion experiments. (Backstepping controller, trajectory 3)

5.3 Generality of the two controllers

A control design strategy should be applicable to different systems. In this section the two designed controllers will be applied to two different systems using miniature cylinders. Since it is very difficult to find miniature double acting cylinder that are commercially available, a pair of single acting cylinders were used to imitate double acting cylinder. Note that the return springs were removed. The two testing systems are summarized in Table 5.3.1, including the cylinders, payload, dead volume and the friction parameters. The same proportional valves as described in chapter 3 were used. The two systems are shown in Figure 5.3.1.

Table 5.3.1: The two different systems used for the generality tests.

		System 1	System 2
Cylinder	Manufacturer	Clippard	Norgren
	Model	SM-6	RM59104/C/20
	Stroke [mm]	9.525	20
	Bore diameter [mm]	6.35	4
	Dead volume (A side) [10^{-6} m^3]	7.116	5.733
	Dead volume (B side) [10^{-6} m^3]	5.715	5.733
	Payload [kg]	0.754	0.484
System friction parameters	Stiction [N]	1.7	1.7
	Coulomb friction [N]	0.8	0.5
	Viscous coefficient [N/m/s]	1.2	0.5
	Stribeck velocity [m/s]	0.03	0.015

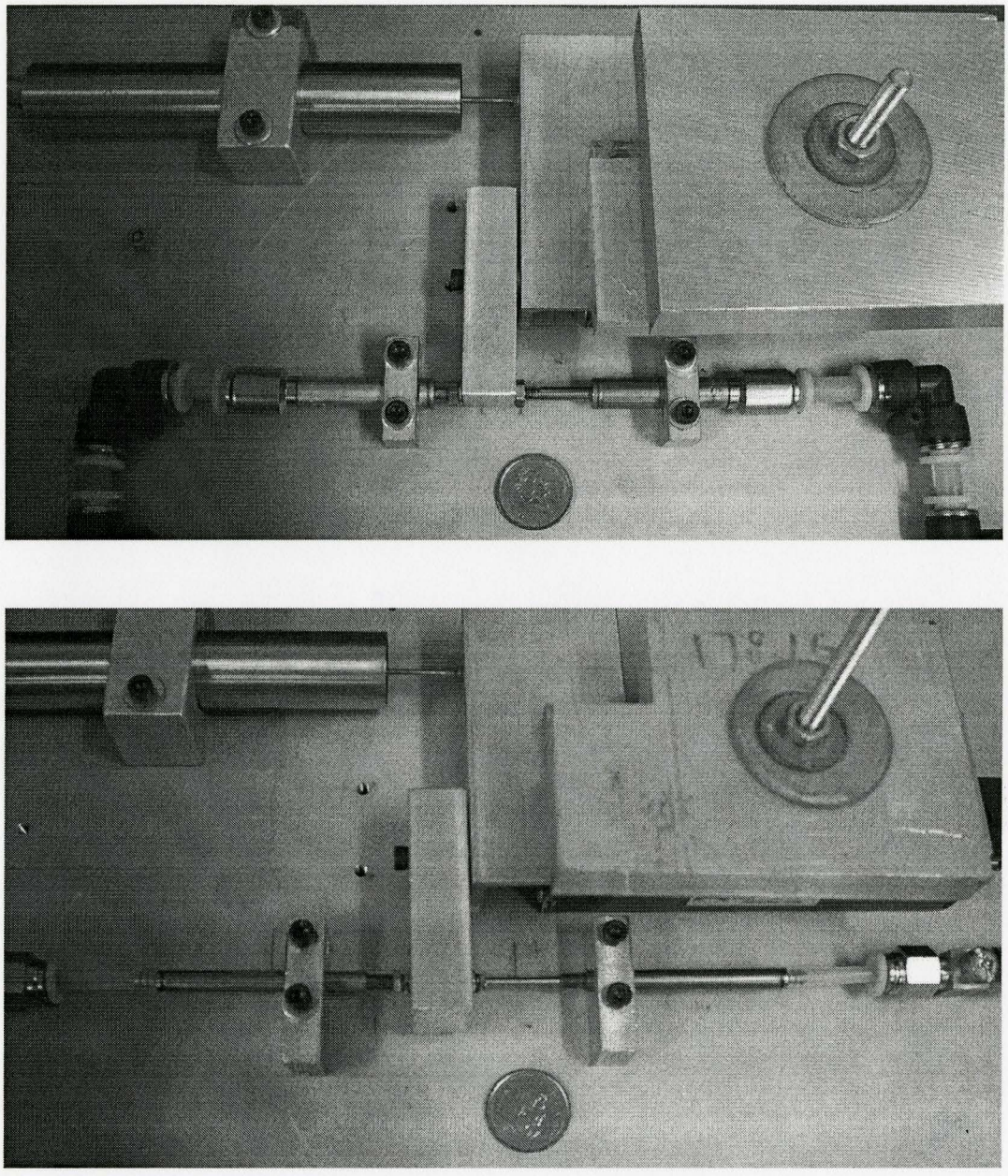

Figure 5.3.1 Testing systems with miniature cylinders (compared with a penny)
(Top: Clippard SM-6, Bottom. Norgren RM59104/C/20)

Because the systems have different stroke lengths, the trajectories tested are different, as listed in Table 5.3.2. The controllers were tuned for the two testing systems respectively. The tuned gains are listed in Table 5.3.3. Each test was repeated five times for both systems. The RMSE values are summarized in Table 5.3.4 and 5.3.5. These results are compared with the 3SD-1T cylinder. The normalized average RMSE values are listed in Table 5.3.6. Since each cylinder has a different stroke length and the trajcetories tested were different, the data are normalized by the stroke length. Note that the trajectory 4 results were not included when calculaing the average. Comparing the RMSE values, it is found that:

(1) The two controller design strategies can be applied to both Clippard SM-6 and Norgren cylinders.

(2) Overall performance of system 1 using Clippard SM-6 cylinders is better than system 2 using the Norgren cylinders. The diameter of Norgren cylinder is 63% of SM-6, and the cross-sectional area of Norgren cylinder is 40% of SM-6. Under the same supply pressure, the maximum driven force is therefore reduced from 17 N to 7 N. The friction parameters of the two systems are similar. Therefore, for the smaller cylinder, the friction becomes dominant. Even when the payload is reduced by 36%, the performance of system 2 is still worse than system 1.

(3) For both systems, the backstepping controller is better than the inverse dynamics controller. For system 1, the normalized average RMSE value of the backstepping controller was 13.5% less than that of the inverse dynamics controller. The inverse dynamics controller was unstable for the 2 Hz sine wave trajectory. For system 2,

the normalized average RMSE value of the backstepping controller was 11.1% less than that of the inverse dynamics controller.

Table 5.3.2: Trajectories tested with the two systems.

Trajectory	System 1	System 2
1: Step with cycloidal in the 1st second, step height [mm]	8	15
2: Ramp, speed [mm/s]	1	3
3: 1 Hz sine wave, amplitude [mm]	3	7.5
4: 2 Hz sine wave, amplitude [mm]	3	2.5

Table 5.3.3: Tuned gains of the two controllers for the two systems.

Controller	Gains	System 1	System 2
Inverse dynamics controller	$\lambda[s^{-1}]$	60	90
	$K_s[kg \cdot s^{-1}]$	50	80
	$\Lambda_a[s^{-1}]$	350	350
	$\Lambda_b[s^{-1}]$	350	350
Backstepping controller	$k_1[s^{-1}]$	60	90
	$k_2[s^{-1}]$	45	80
	$k_3[s^{-1}]$	400	400
	$k_4[s^{-1}]$	400	400

Table 5.3.4: RMSE values [mm] from experiments with system 1.

	Test 1	Test 2	Test 3	Test 4	Test 5	Mean	Std. Dev.
Inverse dynamics controller							
Trajectory 1	0.0472	0.0422	0.0428	0.0467	0.0456	0.0449	0.0023
Trajectory 2	0.0598	0.0948	0.0834	0.1094	0.0636	0.0822	0.0209
Trajectory 3	0.1356	0.1490	0.1349	0.1453	0.1405	0.1411	0.0061
Trajectory 4	unstable						
Backstepping controller							
Trajectory 1	0.0596	0.0569	0.0511	0.0488	0.0609	0.0554	0.0053
Trajectory 2	0.0963	0.0555	0.0625	0.0588	0.0659	0.0678	0.0164
Trajectory 3	0.0981	0.1104	0.1201	0.1037	0.1127	0.1090	0.0085
Trajectory 4	0.2600	0.2844	0.2758	0.2784	0.2792	0.2755	0.0092

Table 5.3.5: RMSE values [mm] from experiments with system 2.

	Test 1	Test 2	Test 3	Test 4	Test 5	Mean	Std. Dev.
Inverse dynamics controller							
Trajectory 1	0.1232	0.1400	0.1350	0.1042	0.1159	0.1236	0.0144
Trajectory 2	0.0575	0.0603	0.0566	0.0534	0.0527	0.0561	0.0031
Trajectory 3	0.5491	0.5115	0.6156	0.5692	0.5857	0.5662	0.0391
Trajectory 4	0.5349	0.5984	0.5678	0.5659	0.5865	0.5707	0.0241
Backstepping controller							
Trajectory 1	0.1152	0.1183	0.1101	0.1230	0.1111	0.1155	0.0053
Trajectory 2	0.1085	0.1024	0.1007	0.0922	0.0832	0.0974	0.0099
Trajectory 3	0.4210	0.4541	0.4558	0.4344	0.4874	0.4505	0.0252
Trajectory 4	0.4442	0.4684	0.5229	0.5097	0.5419	0.4974	0.0402

Table 5.3.6: Comparison of normalized average RMSE values [mm].

	SD-1T	SM-6	Norgren
Inverse dynamics controller	0.2568	0.7152	0.9473
Backstepping controller	0.3067	0.6192	0.8425

5.4 Discussion on the limitation of valve flow rate

In chapter 4 the simulations were performed with the full system model. The valve models developed in chapter 3 were included to obtain the guidelines on the controller gains for experiments. It was mentioned in section 4.3.2 that the mass flow rate of the valves has influence on the pressure tracking performance at the velocity reversal points. In this section, the influence of the valve mass flow rate on the control performance will be investigated by simulations. The simulations are performed on the system using the SD-1T cylinder as in chapter 4.

A simulation was carried out with 1 Hz sine wave profile (trajectory 1) using the inverse dynamics controller. In one case, the valve models were included. In another case the valve models were omitted, i.e., the desired chamber flow rate can be obtained ideally. The desired chamber A flow rate and pressure tracking error are shown in detail at one of

the velocity reversal points in Figure 5.4.1. The desired chamber *B* flow rate has similar characteristics. It indicates that at the velocity reversal point, the desired chamber flow rate is much more bigger than the valve capability (see Table 3.4.2). When the desired flow rate can be ideally achieved, the pressure tracking error is reduced to near zero very quickly. On the other hand, with the real valve models, the pressure tracking error vanishes gradually due to the controller saturation. For the miniature cylinders, this big desired flow rate at velocity reversal points is mainly required to overcome the stiction force.

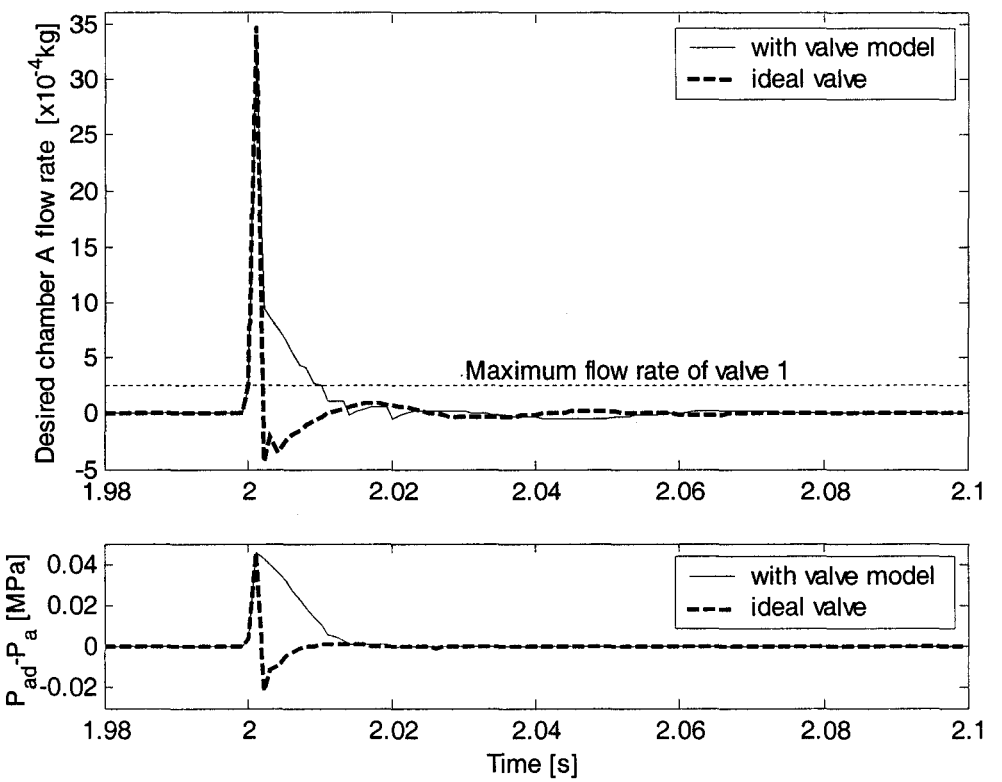

Figure 5.4.1: Influence of the valve saturation at velocity reversal point

In the chapter 4 simulations, the control gains were tuned with the valve models. The tuned gains of the backstepping controller were lower than that of the inverse dynamics controller, as discussed in section 4.4.2. The performances of the two controllers are now compared without the valve limitations. By comparing the desired chamber mass flow rates of the two controllers, i.e., equation (4.3.24), (4.3.27) and (4.4.25), (4.4.26), it is found that the gains λ, K_s, Λ_a and Λ_b of the inverse dynamics controller are roughly equivalent to k_1, k_2, k_3 and k_4 of the backstepping controller when the gain values are large enough, except that the backstepping controller has an extra term $\frac{A_a y + V_{a0}}{KRT}\left(\frac{\gamma_2 z_2 A_a}{\gamma_3 M}\right)$ in the desired chamber A flow rate. The desired chamber B flow rate has similar extra term.

The controller gains will now be re-tuned without the valve models, i.e., the desired chamber flow rate can be obtained without limitation and errors. Based on the analysis above, the gains for the two controllers are tuned to the same values. The re-tuned gains and their roles are given in Table 5.4.1.

Table 5.4.1: Simulation gains of the two controllers.

Role	Inverse dynamics controller	Backstepping controller	Re-tuned value
closed-loop tracking error dynamics	λ	k_1	100
position feedback	K_s	k_2	140
chamber A pressure feedback	Λ_a	k_3	500
chamber B pressure feedback	Λ_b	k_4	500

The re-tuned controllers are simulated with a 7.5 mm amplitude sine wave profile at different frequencies, with the valve model and without the valve model. The RMSE values are listed in Table 5.4.2. It is found that, in the ideal cases, the RMSE values of the backstepping controller are slightly smaller than that of the inverse dynamics controller. From the controller derivation in chapter 4 we observed that the pressure tracking error was compensated in the backstepping controller. This is the main reason for the performance improvement. On the other hand, with the valve models reintroduced, the backstepping controller is worse than the inverse dynamics controller. It is not stable for even a 1 Hz sine wave profile with the re-tuned gains. Figure 5.4.2 shows the tracking errors of the two controllers for the 1 Hz sine wave trajectory, with ideal valves. The backstepping controller has a smaller tracking error during the monotonic portions but it has bigger oscillation at the velocity reversal points. Therefore the controller gains are limited by the mass flow rate capability of the valves.

Table 5.4.2: Comparison of RMSE [mm] from simulations with the re-tuned controllers.

Sine wave frequency	**Inverse dynamics controller**		**Backstepping controller**	
	Ideal valves	**Real valves**	**Ideal valves**	**Real valves**
1 Hz	0.0230	0.0252	0.0203	15.6954
2 Hz	0.0809	13.5043	0.0737	16.0479
3 Hz	0.1715	14.2260	0.1573	16.8710
4 Hz	0.2846	17.4753	0.2643	22.4924

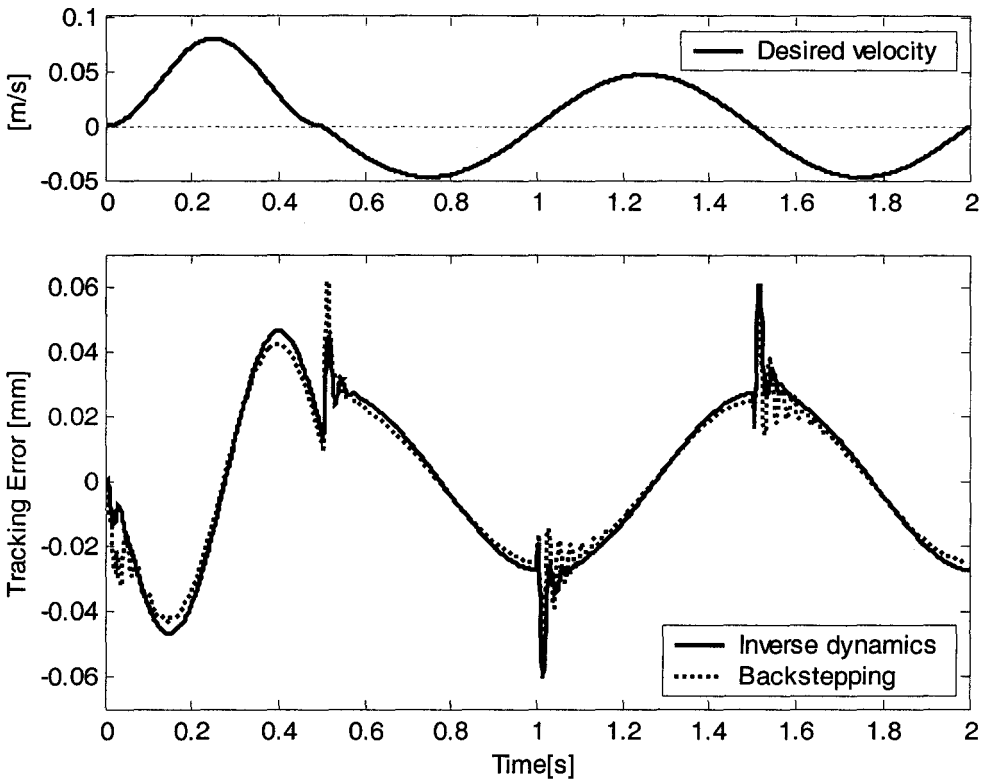

Figure 5.4.2: Comparison of the two controllers (simulation)
Tracking error of 1 Hz sine profile with ideal valves

5.5 Conclusions

The inverse dynamics controller and the backstepping controller were extensively tested. The experiments demonstrate that the two controllers are not sensitive to orientation. Both controllers are robust to an increase of payload but not for a decrease of payload. The generality of the two controller designs is good. The smallest cylinder tested has a 4 mm bore diameter.

Simulations showed that the maximum mass flow rate of the valves has a significant influence on the tracking performance. The bandwidth and the controller gains are limited by the capability of valve.

CHAPTER 6

CONCLUSIONS

6.1 Summary

In this research the development of a servo pneumatic system based on miniature cylinders was presented. The system was modeled using a combination of the mechanistic and empirical approaches. The open-loop system model was validated by comparing simulation and experimental results. Two multiple-input single-output nonlinear controllers, based on the inverse dynamics and backstepping methods respectively, were designed, simulated and experimentally tested. The experimental results demonstrated the robustness and generality of the modeling and control design strategies.

6.2 Achievements

The main achievements of this thesis are summarized as follows.

(1) This research studied the modeling and control design for miniature cylinders. It demonstrated the feasibility of miniature pneumatic actuators being used in smaller scale applications. The smallest cylinder tested has a bore diameter of 4 mm.

(2) The new system structure incorporated four low-cost 2-way proportional valves to provide greater design flexibility than the traditional single 4-way servo valve solution. In addition to position control, the control design methods allow a second control objective to be implemented.

(3) A novel method for valve mass flow rate modeling was presented. The least square surface fitting using bipolynomial function was shown to provide more accuracy and simplicity than the commonly used nozzle flow equations and sectional curve fitting method.

(4) In the experiments, the inverse dynamics controller produced SSE within ±0.08mm and the backstepping controller ±0.05mm. The two controllers produced maximum tracking errors of ±0.5 mm and ±0.3 mm for a 1 Hz sine wave trajectory respectively. Compared with a linear PVA controller, the RMSE of tracking errors were reduced by 85% on average.

(5) The two controllers were shown to be robust to orientation variation. They were also shown to be robust to increasing the moving mass, but not to decreasing it. The potential instability can be avoided in practice by tuning the gains for the smallest payload. The controllers were also tested with miniature cylinders with different bore diameter and stroke length.

6.3 Recommendations for future work

(1) The accuracy of the friction model has a big impact on the tracking accuracy. The newly developed friction models, e.g., the LuGre model, should be investigated with the pneumatic cylinders. To obtain plenty of data over the limited stroke length for friction modeling, new experiment methods should be considered. For example, using closed-loop velocity control for friction force/velocity data acquisition.

(2) The valve flow rate capability limits the system bandwidth and the tracking accuracy, especially at the velocity reversal points. The selection of valves should consider the

maximum desired mass flow rate based on not only the desired system bandwidth and moving profiles but also on the friction forces.

(3) To use the cylinder as a joint actuator in robotics, force control should also be studied. The controllers designed in chapter 4 provide one more control objective that could be used to implement open-loop force control or stiffness control. If a force sensor is added then closed-loop force control or impedance control algorithms can be developed. The new controllers should be tested with tasks involving both unconstrained and constrained motions.

REFERENCE

[1] J.M. Tressler, T. Clement, H. Kazerooni and M. Lim, "Dynamic behaviour of pneumatic systems for lower extremity extenders," in *Proceedings of the 2002 IEEE International Conference on Robotics & Automation*, Washington, DC., 2002, pp. 3248-3253.

[2] K. A. AI-Dakkan, M. Goldfarb and E. J. Barth, "Energy saving control for pneumatic servo systems," in *Proceedings of the 2003 IEEE/ASME International Conference on Advanced Intelligent Mechatronics*, 2003, pp. 284-289.

[3] J.Y.Lai, C.H. Meng, and R. Singh, "Accurate position control of a pneumatic actuator," *ASME Journal of Dynamic Systems, Measurement, and Control*, Vol. 112, pp. 734-739, 1990.

[4] Robert B. van Varseveld and G. M. Bone, "Accurate position control of a pneumatic actuator using on/off solenoid valves," *IEEE/ASME Transactions on Mechatronics*, Vol. 2, No. 3, pp. 195-204, Sep. 1997.

[5] J. E. Bobrow and F. Jabbari, "Adaptive pneumatic force actuation and position control," *ASME Journal of Dynamic Systems, Measurement, and Control*, Vol. 113, pp. 267-272, June 1991.

[6] Shih, Ming-Chang and Tseng, Shy-I, "Identification and control of a servo pneumatic cylinder," *Control Engineering Practice*, Vol.3, No.9, pp.1285-1290, Sep. 1995.

[7] J. L. Shearer and Cambridge Mass, "Study of pneumatic processes in the continuous control of motion with compressed air I, II," *Transactions of the ASME*, pp. 233-249, Feb. 1956.

[8] S. Liu and J. E. Bobrow, "An analysis of a pneumatic servo system and its application to a computer-controlled robot," *ASME Journal of Dynamic Systems, Measurement, and Control*, Vol. 110, pp. 228 – 235, Sep. 1988.

[9] B.W. McDonell and J. E. Bobrow, "Adaptive tracking control of an air powered robot actuator," *ASME Journal of Dynamic Systems, Measurement, and Control*, V115, pp. 427-433, 1993.

[10] E. Richard and S. Scavarda, "Comparison between linear and nonlinear control of an electropneumatic servodrive," *ASME Journal of Dynamic Systems, Measurement, and Control*, vol.118, pp. 245-252, 1996.

[11] J. E. Bobrow and B. W. McDonell, "Modeling, identification, and control of a pneumatically actuated, force controllable robot," *IEEE Transactions on Robotics and Automation*, Vol. 14, No. 5, pp. 732-742, Oct. 1998.

[12] S. Ning, "Theoretical and experimental study of pneumatic servo motion control systems," Ph.D. dissertation, McMaster University, Hamilton, ON, Canada, 2004.

[13] S. Ning and G. M. Bone, "Development of a nonlinear dynamic model for a servo pneumatic positioning system," in *Proceedings of the IEEE International Conference on Mechatronics & Automation*, Niagara Falls, Canada, July 2005, pp. 43-48.

[14] Edmond Richer and Yildirim Hurmuzlu, "A high performance pneumatic force actuator system. part I – nonlinear mathematical model," *ASME Journal of Dynamic Systems, Measurement, and Control*, vol. 122, pp. 416-425, Sep. 2000.

[15] B.M.Y Nouri, F Al-Bender, J Swevers, P Vanherek and H. van Brussel, "Modeling a pneumatic servo positioning system with friction," in *Proceedings of the 2000 American Control Conference*, Vol. 2, 28-30 June 2000, pp.1067-1071

[16] B. Armstrong-Helouvry, P Dupont and C. Canudus de Wit, "A survey of models, analysis tools and compensation methods for the control of machines with friction," *Automatica*, Vol. 30, No. 7, pp. 1083-1138, 1994.

[17] A. K. Paul, J K. Mishra and M. G Radke, "Reduced order sliding mode control for pneumatic actuator," *IEEE Transactions on Control Systems Technology*, Vol.2, No.3, pp. 271-276, Sep.1994.

[18] J Wang, D.J.D. Wang, P.R.Moore and J Pu, "Modelling study, analysis and robust servocontrol of pneumatic cylinder actuator systems," in *IEE Proceedings, Control Theory Appl.*, Vol. 148, No. 1, January 2001, pp. 35-42.

[19] C. Canudas de Wit, H. Olsson, K. J Astrom and P Lischinsky, "A new model for control of systems with friction," *IEEE Transactions on Automatic Control*, Vol. 40, No. 3, pp. 419-425, March 1995

[20] C. Canudas de Wit and P Lischinsky, "Adaptive friction compensation with partially known dynamic friction model," *International Journal of Adaptive Control and Signal Processing*, Vol. 11, pp. 65-80, 1997

[21] M. S. Madi, K. Khayati, and P Bigras, "Parameter estimation for the LuGre friction model using interval analysis and set inversion," *2004 IEEE International Conference on Systems, Man and Cybernetics*, Vol. 1, 10-13 Oct. 2004, pp. 428 – 433

[22] P R. Moore, R. H. Weston and T W Thatcher; "Compensation in pneumatically actuated servomechanisms", *Transactions of the Institute of Measurement and Control*, Vol. 7, No 5, pp. 238-244, Oct.-Dec. 1985

[23] S. Ning and G M. Bone, "High steady-state accuracy pneumatic servo positioning system with PVA/PV control and friction compensation," in *Proceedings of the 2002 IEEE International Conference on Robotics & Automation*, Washington, DC, 2002, pp. 2824-2829

[24] S. Ning and G M. Bone, "Methods for higher accuracy pneumatic servo position control," in *Proceedings of the 2002 CSME Forum*, May 21-24, 2002, Kingston, ON, Canada.

[25] S. Aziz and G M. Bone, "Automatic tuning of pneumatic servo actuators," *Advanced Robotics, VSP and Robotics Society of Japan*, Vol. 13, No. 6, pp. 563-576, 2000.

[26] Han Koo Lee, Gi Sang Choi and Gi Heung Choi, "A study on tracking position control of pneumatic actuators," *Mechatronics*, 12 (2002), pp. 813-831, 2002.

[27] J Slotine and W Li, *Applied Nonlinear Control*, Prentice Hall, Englewood Cliffs, New Jersey, 1991

[28] J Slotine and W Li, "On the adaptive control of robot manipulators," *1986 ASME winter annual meeting*, Anaheim, CA, vol. 3, Dec. 1986, pp. 51-56.

[29] J Y Hung, W Gao and J.C. Hung, "Variable structure control. a survey," *IEEE Transactions on Industrial Electronics*, Vol. 40, Issue 1, pp. 2-22, Feb. 1993

[30] J Tang and G Walker, "Variable structure control of a pneumatic actuator," *ASME Journal of Dynamic Systems, Measurement, and Control*, Vol. 117, pp. 88-92, 1995

[31] B. W Surgenor and N D Vaughan, "Continuous sliding mode control of a pneumatic actuator," *ASME Journal of Dynamic Systems, Measurement, and Control*, Vol.119, pp. 578-581, Sep.1997

[32] J Song and Y Ishida, "A robust sliding mode control for pneumatic servo systems," *International Journal of Engineering Science*, Vol. 35, No. 8, pp. 711-723, 1997

[33] S. R. Pandian, Y Hayakawa, Y Kamoyama and S. Kawamura, "Practical design of a sliding-mode controller for pneumatic actuators," *ASME Journal of Dynamic Systems, Measurement, and Control*, vol.119, No. 4, pp. 666-674, 1997

[34] S. Ning and G M. Bone, "Experimental comparison of two pneumatic servo position control algorithms," in *Proceedings of the IEEE International Conference on Mechatronics & Automation*, Niagara Falls, Canada, July, 2005, pp. 37-42.

[35] Petar V Kokotovic, "The joy of feedback: nonlinear and adaptive," *IEEE Control systems Magazine*, Vol. 12, Issue 3, pp. 7-17, June 1992.

[36] M. Krstic, I. Kanellakopoulos and P Kokotovic, Nonlinear and Adaptive Control Design, John Wiley & Sons, Inc., New York, 1995

[37] O. M. E. Rifai and M. M. Bridges, "Integrator backstepping control of a pneumatic actuator-based robot manipulator," in *Proceedings of the ASME Dynamic Systems and Control Division,* DSC-Vol 61, 1997, p 487-495

[38] M.R. Sirouspour and S.E. Salcudean, "On the nonlinear control of hydraulic servo-systems," in *Proceedings of the 2000 IEEE International Conference on Robotics & Automation*, April 2000, pp. 1276-1282.

[39] P Carbonell, Z.P Jiang and D W Repperger, "Nonlinear control of a pneumatic muscle actuator· backstepping vs. sliding-mode," in *Proceedings of the 2001 IEEE International Conference on Control Applications*, Mexico, 2001, pp. 167-172.

[40] A. V Oppenheim, R. W Schafer and J R. Buck, *Discrete-Time Signal Processing*, 2nd Edition, Prentice Hall, Englewood Cliffs, New Jersey, 1994.

[41] Clippard Instrument Laboratory, Inc, "Electrically Controlled Proportional Valve," U S. Patent US6,220,569B1, April 24, 2001

[42] Michael T Heath, *Scientific Computing: An Introductory Survey*, Second Edition, McGraw-Hill, New York, 2002.

[43] James R. Phillips, "Interactive 2-dimensional and 3-dimensional data modeling", http://www.zunzun.com, accessed Apr 2005

[44] J Amin, B. Friedland and A. Harnoy, "Implementation of a friction estimation and compensation technique," *IEEE Control Systems Magazine*, Vol. 17, Issue 4, pp. 71-76, Aug. 1997

[45] G A. Sohl and J E. Bobrow, "Experiments and simulations on the nonlinear control of a hydraulic servosystem," *IEEE Transactions on Control System Technology*, Vol. 7, No. 2, pp. 238-247, March 1999

[46] Masayoshi Tomizuka, "On the compensation of friction forces in precision motion control," in *Asia-Pacific Workshop on Advances in Motion Control Proceedings*, 1993, 15-16 July 1993, pp. 69-74.

[47] Y Zhang, B. Fidan and P A. Ioannou, "Backstepping control of linear time-varying systems with known and unknown parameters," *IEEE Transactions on Automatic Control*, Vol. 48, Issue 11, pp.1908-1925, Nov 2003

APPENDIX A

MASS FLOW RATE MODEL DATA FOR VALVES 2, 3 AND 4

The measured flow rate surfaces for the valves 2, 3 and 4 are shown in Figure A.1, Figure A.3 and Figure A.5, their bipolynomial surface fitting results are shown in Figure A.2, Figure A.4 and Figure A.6, respectively The coefficients of the bipolynomial model (3.4.8) for each valve are listed in Table A.1

Table A.1 Coefficients of bipolynomial model for the three valves.

Valve 2		Valve 3		Valve 4	
a_2	$-4\ 4998 \times 10^{-05}$	a_3	$-9\ 3344 \times 10^{-05}$	a_4	$-2\ 2503 \times 10^{-05}$
b_2	$5\ 9260 \times 10^{-10}$	b_3	$9\ 7016 \times 10^{-10}$	b_4	$4\ 0563 \times 10^{-10}$
c_2	$-1\ 0109 \times 10^{-15}$	c_3	$-1\ 2429 \times 10^{-15}$	c_4	$-6\ 8382 \times 10^{-16}$
d_2	$3\ 5487 \times 10^{-05}$	d_3	$6\ 9666 \times 10^{-05}$	d_4	$1\ 5715 \times 10^{-05}$
e_2	$-4\ 7317 \times 10^{-10}$	e_3	$-1\ 0056 \times 10^{-09}$	e_4	$-2\ 8343 \times 10^{-10}$
f_2	$7\ 0595 \times 10^{-16}$	f_3	$1\ 3483 \times 10^{-15}$	f_4	$4\ 0478 \times 10^{-16}$
g_2	$-5\ 6555 \times 10^{-06}$	g_3	$8\ 1698 \times 10^{-07}$	g_4	$-1\ 8110 \times 10^{-06}$
h_2	$7\ 9544 \times 10^{-11}$	h_3	$1\ 9884 \times 10^{-10}$	h_4	$3\ 8639 \times 10^{-11}$
i_2	$-8\ 5645 \times 10^{-17}$	i_3	$-2\ 9833 \times 10^{-16}$	i_4	$-3\ 2427 \times 10^{-17}$

Note that due to the manufacturing tolerances, the performance is different for each valve. From the data it is found that valve 3 has the maximum flow rate while valve 4 has the minimum.

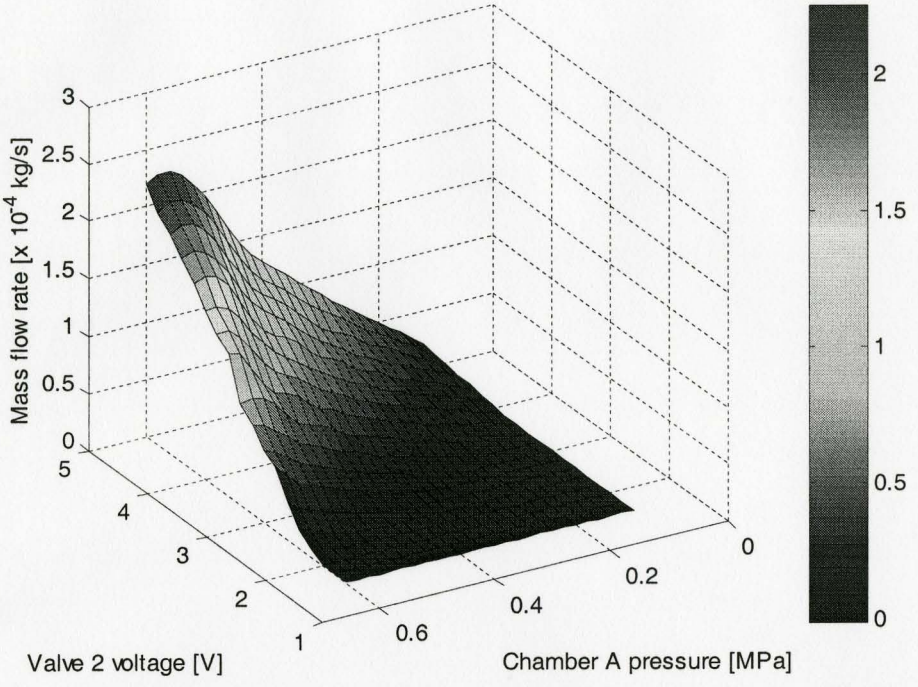

Figure A.1 The measured flow rate surface for valve 2.

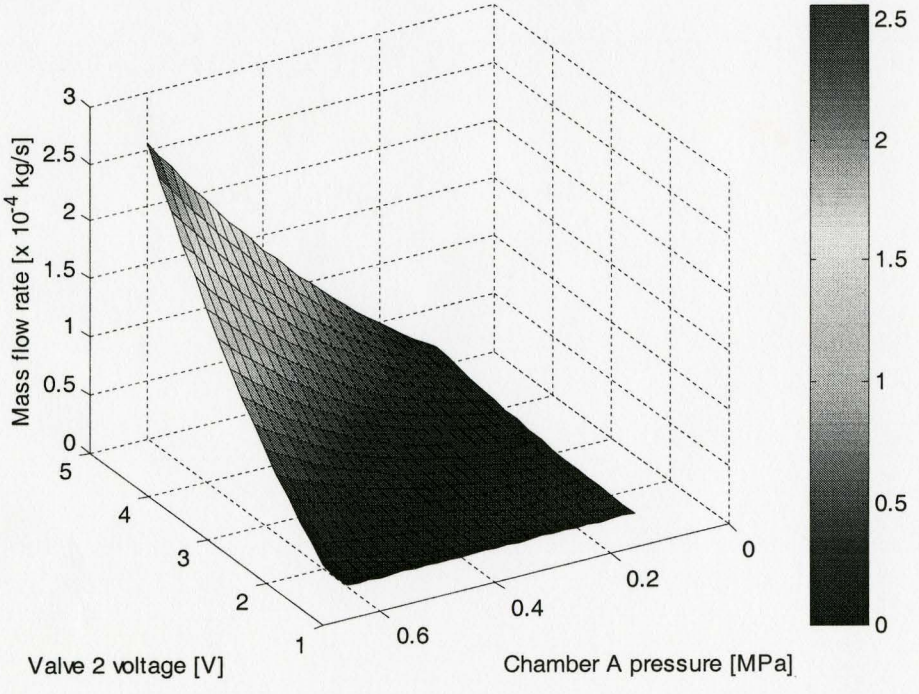

Figure A.2. Bipolynomial surface fitting result for mass flow rate of valve 2.

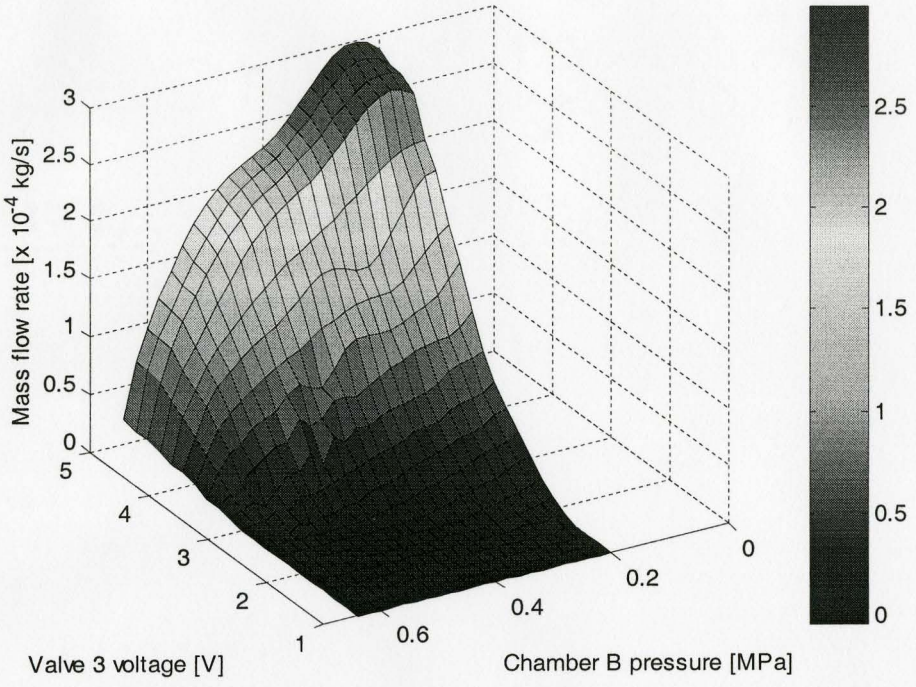

Figure A.3 The measured flow rate surface for valve 3

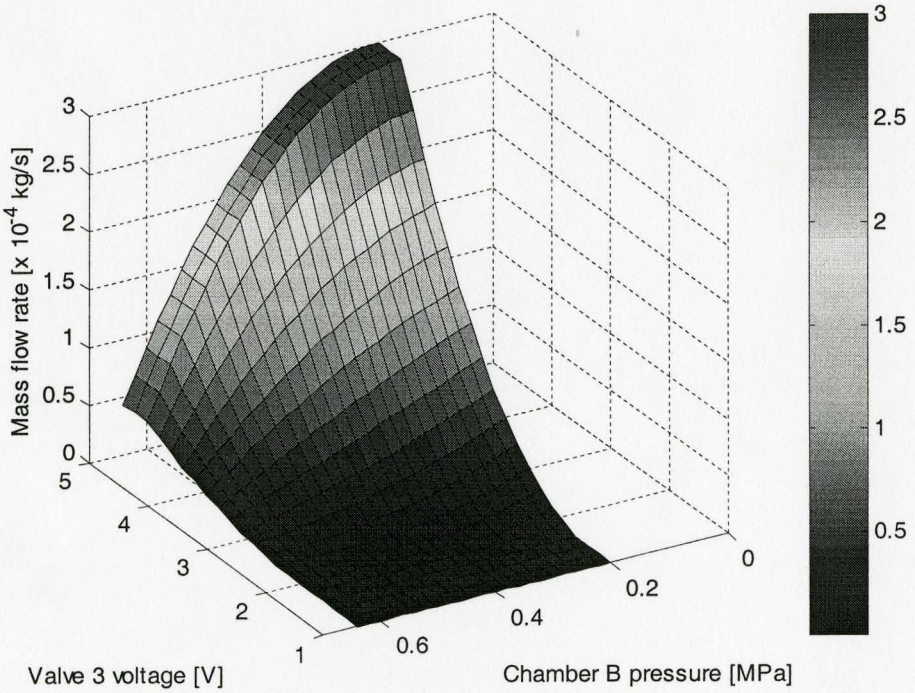

Figure A.4: Bipolynomial surface fitting result for mass flow rate of valve 3

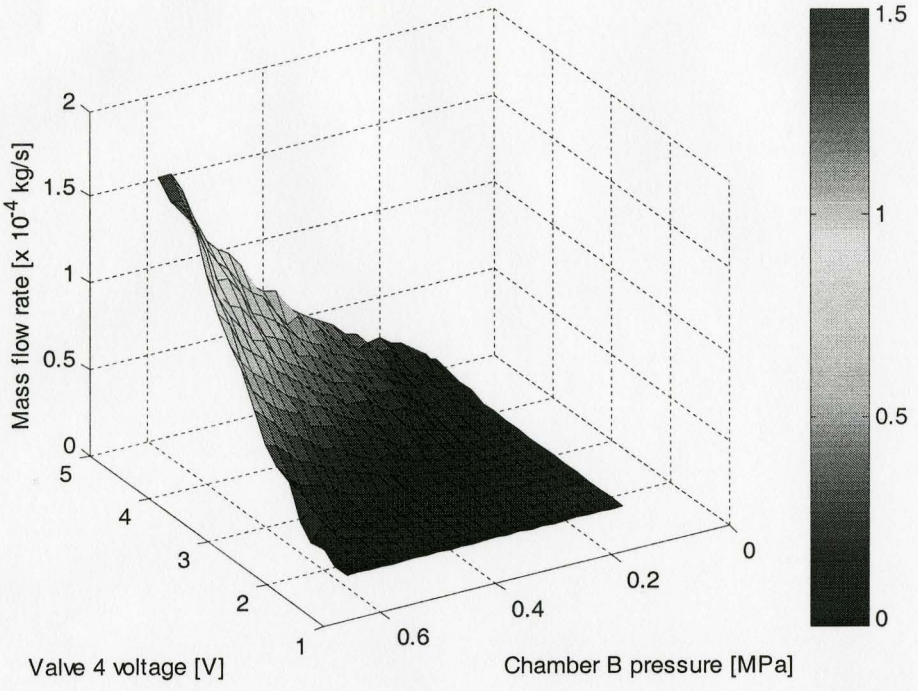

Figure A.5: The measured flow rate surface for valve 4.

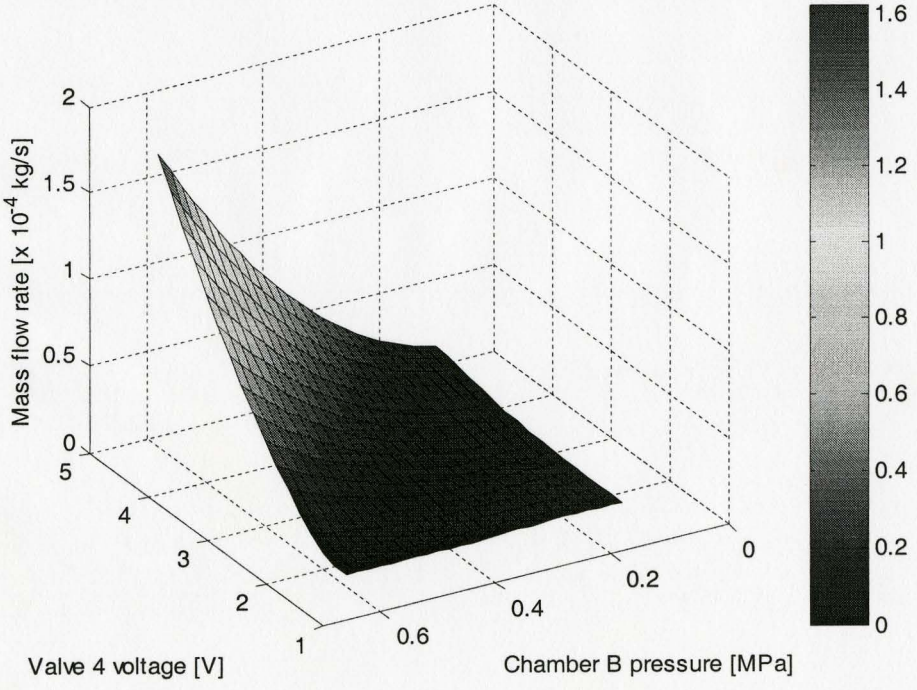

Figure A.6: Bipolynomial surface fitting result for mass flow rate of valve 4.